NIR Spectroscopy for Personal Screening

by
Aamer Saleem

Submitted for the degree of **Ph.D. in Engineering** to the **University of Warwick**
describing research conducted in the **School of Engineering**
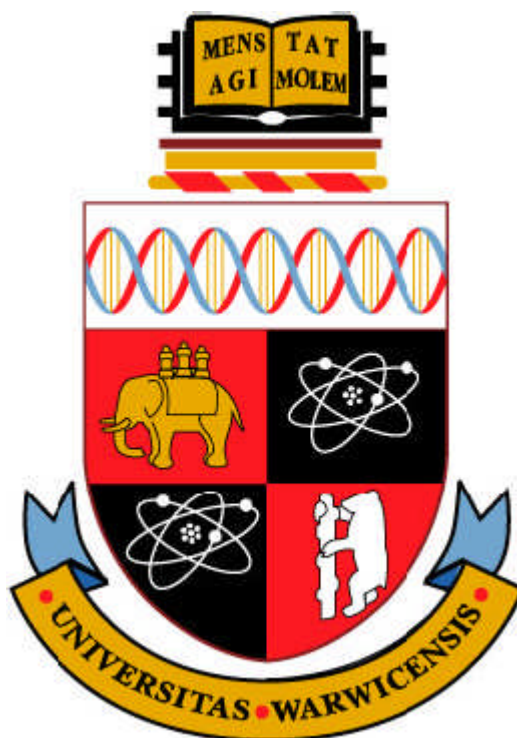
School of Engineering
University of Warwick
August 2011

Table of contents

List of figures

Chapter 3

Chapter 5

List of tables

Acknowledgments

This work would not have been possible without the unflinching, consistent and invaluable support of Prof. David A. Hutchins. He was always a source of crucial guidance and insight, while allowing me all the leeway to work on the subjects that I felt comfortable with. He was extraordinarily patient and understanding whenever I (all too often) ran up dead ends, and felt desperate and hopeless. It was only through his constant encouragement and support that the work was finished on schedule.

Additionally, I would be remiss not to mention the pivotal help of Celine Canal with the experimental work; her expertise in setting up optical bench arrangements was always a great source of learning and help, and she was always willing to brainstorm new ideas and avenues of work. Thanks in no small measure are also due to Lee Davis, for his ready help with resolving any technical issues whenever they arose. My sincere gratitude also goes to Robert Southgate and Ritesh Gohel for their help with the work, as well as to all other members of the group, including Yin Xiaokang, Vipin Seetohul, Prakash Pallav and Chuan Li (Luby) for their support.

Finally, I would be eternally grateful for the unwavering support of my family, including my wife Fatima and my parents, which allowed me to keep focus and stay committed to the task.

Declaration

The work presented in this thesis has been carried out by the author, except where otherwise stated. It has been performed in the School of Engineering, at the University of Warwick. No part of this work has previously been submitted to the University of Warwick, or any other academic institution for consideration for a higher degree. All publications to date arising from this work are listed in the publications section in the end.

Summary

This work presents investigations into the use of the near-infrared (NIR) signals to interrogate, detect and image specific chemical compounds of interest in a security screening application, including when such compounds are hidden behind single layers of clothing fabric.

In an initial set of experiments, the mechanisms governing the interaction of NIR signals with clothing fabrics and similar materials has been studied, in order to account for the influence of fabric layers when detecting hidden chemicals. Throughout the rest of the work, NIR spectroscopy has been used as a means to perform qualitative and quantitative analysis, in order to detect the presence of chemicals, and quantify the concentration in aqueous solution of liquids.

It has been shown that, while the compounds can be identified on the basis of the characteristic features that appear in the relevant NIR spectra, the origin and nature of these spectra necessitate that such identification be performed with a chemometrics-based approach. Accordingly, multivariate calibration models based on neural networks and partial least squares regression (PLSR) have been developed to perform the requisite analyses. Results of calibration and testing with a range of data are reported.

In order to facilitate operation in practical security screening, the development and testing of a software-based lock-in amplifier is reported, as a mean to enhance the signal-to-noise ratio (SNR) of the spectral data. It is shown that the amplifier can process up to 40 wavelength channels in parallel, to extract the spectral data buried in noise in each channel. Hence, with the SNR of the input signal set as low as -60 dB (by introducing software-generated additive white noise in the spectra), adequate noise suppression has been obtained, allowing the resulting spectral data to be used for requisite chemical detection.

Finally, an integrated spectroscopic imaging application is developed to perform two-dimensional cross-sectional scans of chemical samples, carry out lock-in amplification of the recorded intensity spectra, and plot the results of neural network-based chemical detection in the form of intensity images colour-coded to depict the presence of the pertinent chemicals at the scanned coordinates.

Chapter 1

NIR spectroscopy: Background, theory & applications

1.1 Introduction – The detection of chemicals used for explosives

During the last few decades, terrorist attacks based on improvised explosive devices (IEDs) have emerged as a security threat in most parts of the world [1-3]. Lately, however, this threat has become more potent due to the increased reliance by the perpetrators of such attacks on explosives improvised from common household/ industrial materials such as hydrogen peroxide and acetone, which are difficult to detect and control at vulnerable locations [4]. These materials can be very stable in their raw form, and carried in innocuous-looking containers such as PET bottles, hidden from view beneath layers of clothing.

Some inspection technologies that attempt to detect chemicals potentially used in IEDs have been tested for incorporation in scanning systems installed at airports [5, 6]. These include electromagnetic induction, X-ray, vapour suction and Raman spectroscopy. Electromagnetic induction differentiates between water and flammable liquids on the basis of differences in dielectric constants [7]. However, it falls short of detecting a chemical such as hydrogen peroxide in this manner, as its dielectric constant is similar to that of water. In X-ray systems, detection is based on the atomic number and density of the sample, which makes it difficult, for instance, to distinguish between innocuous substances such as honey and more dangerous materials that have similar atomic numbers and densities [8]. The trace vapour suction method uses a conductive polymer to detect chemicals such as hydrogen peroxide [9]; however, this method fails if the container is tightly capped and sealed, so that no leakage exists. Finally, Raman spectroscopy allows detection of materials such as hydrogen peroxide, but has limited effectiveness when applied on coloured bottles and mixed drinks, as the resulting fluorescence can interfere with and severely degrade the analysis of the weak Raman spectra of the pertinent chemical [10].

The purpose of this work is, therefore, to explore the use of near-infrared spectroscopy (NIRS) as a technique that overcomes some of the limitations of afore-mentioned

technologies to detect, image and characterize chemicals that could potentially be used in IEDs, when these are concealed underneath clothing.

The use of NIRS in chemical and food processing industries for quality and process control is well-established [11], and relies on the unique mechanism by which NIR energy interacts with these materials. This technique has been investigated here in the context of security screening by maintaining focus on certain considerations, such as imaging across fabric layers, which are unique to such an application. The experimental evidence gathered in the course of this work has established the feasibility of the use of NIRS in this application.

1.2 Background to NIR

1.2.1 Why spectroscopy would be useful

The rapid growth in recent years in the development of increasingly sophisticated signal and image processing systems has facilitated the deployment of different non-destructive testing techniques for the identification of compounds with relevance in security screening. While techniques such as X-ray computer tomography (CT), electromagnetic induction (EMI), ultrasonic imaging and eddy current testing have been the subject of research and shown to bear considerable promise in certain applications, these and similar techniques have limited use in imaging/identifying compounds concealed on the person of a subject. It is, therefore, felt that a technique that would allow the capability to rapidly and accurately characterize the relevant compounds based on qualitative as well as quantitative analyses would serve to fill a major functionality gap that currently exists in security screening applications.

In this context, NIRS has previously been shown to allow the imaging of various non-metallic materials [12]. Additionally, its use in identifying and quantifying the constituent chemicals of a given compound is well-established [13]. In effect, NIRS has emerged during recent decades as the method of choice to perform structural and chemical analysis of samples in order to test for heterogeneity and other parameters related to process and quality control. The suitability of the relevant frequency range for use in these applications arises from the fact that NIR frequencies are on the same order of magnitude as the vibrational frequencies of molecules constituting the tested

compounds. The NIR band extends from around 780 nm to 2,500 nm [14], which includes wavelengths that correspond to modes of molecular vibrational transitions that are higher order overtones and combinations of the fundamental bands occurring in the mid to far infrared range [15]. Such higher order transitions are excited in the molecules with the absorption of NIR energy in the anharmonic oscillations of different chemical functional groups [16], leading to appearance of absorbance spectra characteristic of the relevant groups. The nature of these vibrations dictates that the resulting spectral bands are broader and have lower intensity levels than the corresponding fundamental bands. Note that absorption of energy in the visible band can also produce spectra characteristic of the vibrational energy levels of the particular molecules [17]; this gives rise to the possibility of performing visible and NIR spectroscopy concurrently [18, 19].

During the course of this work, the characteristic absorption of NIR energy by different functional groups, and by extension molecular structures, was used for detecting and analysing specific chemicals behind fabric layers.

1.2.2 The electromagnetic spectrum

The layout of the electromagnetic spectrum, showing the position of the infrared region relative to the rest of the frequency bands, is illustrated on a logarithmic wavelength scale in Figure 1.1. As seen, the wavelength progressively increases from the visible region through infrared to radio waves. The characteristics of a vast range of wavelengths, including NIR at the transition between the visible and infrared regions, allow their potential use in spectroscopic analysis. The frequency ν of the waves, measured in Hz, is inversely related to wavelength λ in metres as follows [20]:

$$\nu = c/\lambda \qquad (1.1)$$

where c is the speed of light, with an approximate value of $3{\times}10^8$ m/sec. Thus, the increasing wavelength from visible through NIR to mid-IR range is accompanied by corresponding decrease in frequency.

Besides its characterisation as waves defined in terms of frequency and wavelength, the radiation in the electromagnetic spectrum can also be perceived to comprise packets of energy called photons [21]. Similar to the other characteristics, different regions of the

---

Chapter 1: NIR spectroscopy: Background, theory and applications

spectrum are defined by photons with varying levels of energy. An important relationship, used to describe the energy E of the photons, measured in joules, in terms of the frequency v in Hz of the corresponding wave, is as follows [20]:

$$E = hv \tag{1.2}$$

where h represents Plank's constant, with a value of 6.6×10^{-34} J.sec. Based on (1.1) and (1.2), it may be noted that energy E is inversely proportional to wavelength λ, a relationship that is highlighted in Figure 1.1 to emphasize the direction of increasing energy as opposite to that of increasing wavelength.
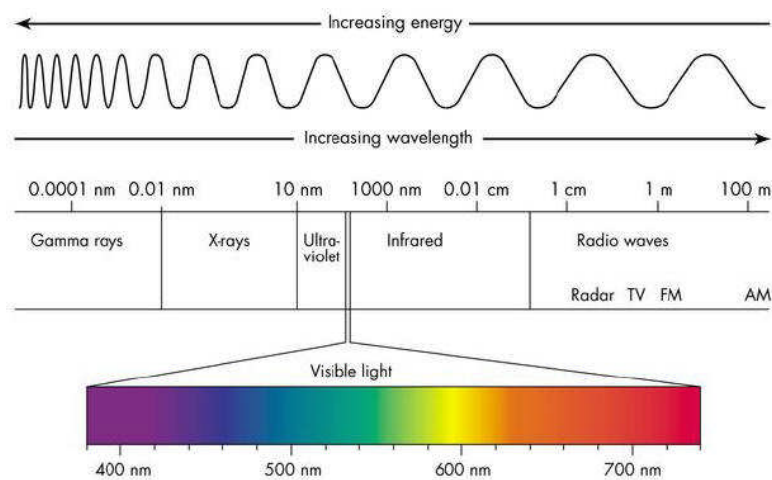
Figure 1.1 – The electromagnetic spectrum, illustrated on a logarithmic wavelength scale [22].

As depicted in Figure 1.1, the infrared region covers the space between visible light and radio waves, and includes wavelengths ranging from approximately 780 nm to 1 mm. As shown in Figure 1.2, this region is further divided into three sub-regions, called near-infrared, mid-infrared and far-infrared [23]. The location of near-infrared, in terms of the energy of the radiation, is deemed to favour its exploitation in non-destructive testing and imaging applications.

The second unit of measure shown alongside wavelength λ in Figure 1.2 is wavenumber $\overline{v}$, which is the reciprocal of λ, and is expressed in units of cm^{-1} [24]:

$$\overline{v} = 1/\lambda \tag{1.3}$$

Based on (1.1), (1.2) and (1.3), photon energy E can be expressed in terms of wavenumber $\overline{v}$ as:

$$E = h.c.\overline{\nu} \tag{1.4}$$

As seen, expressing wavelength in terms of $\overline{\nu}$ allows a direct relationship to be drawn between the wavelength and the energy of the radiation in a given region of the spectrum [20].
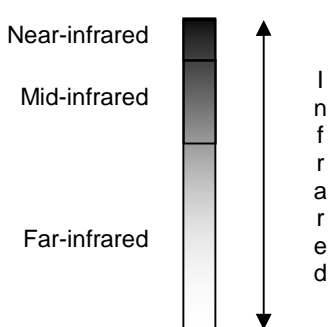
	Wavelength λ (µm)	Wavenumber $\overline{\nu}$ (cm^{-1})
Near-infrared	0.78 – 2.5	12821 – 4000
Mid-infrared	2.5 – 40	4000 – 250
Far-infrared	40 – 1000	250 – 10

Figure 1.2 – The infrared region, subdivided into near, mid and far-infrared.

When electromagnetic energy is directed on a substance, the interaction between the impinging photons and the relevant matter may be characterized by a transfer of energy to the matter, whereby the photons get completely absorbed. The phenomenon allows deduction of qualitative and quantitative information about the substance, based on the nature of the photons absorbed [21]. The particular characteristics of the NIR band in terms of frequency and wavelength of the waves, and the energy of the photons, make this region particularly suited for interrogation of chemical compounds in order to deduce information about their composition, while allowing the waves to travel relatively unimpeded through any intervening layers of clothing fabrics.

1.2.3 History

The study of visible light and attempts at understanding the nature of colour by scholars and astronomers date back to the second century; however, the first truly structured treatment of the subject came about in 1665, when Newton conducted experiments demonstrating dispersion of white light into constituent colours, and expanded on the nature of these colours as part of the visible spectrum within the electromagnetic spectrum [25]. The discovery of the infrared region was made in 1800 by Herschel, in the course of experiments designed to measure the temperature of the various constituent colours of visible light [15]. The earliest study reporting infrared spectra of

chemicals was performed by Coblenz in early twentieth century [21], while the specific use of near-infrared spectroscopy in a practical application came about around fifty years later, when Karl Norris employed it in a study of analytes in agricultural commodities [26]. A number of studies that followed used NIRS, as it transitioned from dormancy to becoming recognized as a powerful analytical tool. During the 1980s, its popularity grew manifold, as its deployment in various industrial quality and process control applications was facilitated by the development of sophisticated miniaturized instrumentation, allowing the development of standalone test stations that could be easily integrated in the existing industrial processes. NIRS has since been adopted as the non-destructive evaluation technique of choice, replacing traditional NDT tools in several industries [21].

1.2.4 Current applications

A brief overview of the use of NIRS in the quantitative and qualitative analysis of products spanning foodstuffs and agricultural products, pharmaceuticals and medical uses is presented below.

The use of NIRS for quality checking of different foodstuffs and agricultural products has grown in popularity in recent decades. The main reason for this is the alternative to traditional testing techniques it offers, in terms of fast, accurate, economical and non-destructive testing as opposed to the often-time consuming and destructive approaches used in the traditional techniques [27]. To this end, it has been used in applications designed to determine the end-point temperature of fish and meat products [28, 29]. Additional applications have included determination of oil and fat content in the test products [30, 31]. Further, the technique has been used to test beverages and foods for quality control/ verification, and for testing specific analytes such as adulterants in alcoholic beverages [32, 33]. The quality control application has been extended to dairy products as well [34-36]. In the fresh fruit processing industry, NIRS has been employed in multifarious quality control processes [37, 38], including non-destructive determination of soluble solids content (Brix number) [19, 39-41] and total acidity [42-44], as well as physical characteristics such as firmness of various fruits [45-47]. Additional applications have included the sorting of produce based on properties such as sweetness, acidity and colour using Vis/NIRS [18, 48], and determination of the

moisture content in various products [49]. In short, the applications continue to grow as the technology matures and further advances are made in the development of compact, fast and reliable instrumentation.

Another popular use of NIRS is in industrial quality control within the pharmaceutical industry [50], where it has offered the means to meet the industry's necessarily stringent quality control requirements while achieving the requisite high throughput rates, coupled with the ability to implement multi-constituent analysis with accurate prediction of test samples that do not meet the specified tolerance limits [51]. The methods used to perform the measurements continue to evolve, with new approaches to product analysis reported regularly for regulatory approval [52]. The technique has been employed for monitoring multiple stages of the product development cycle, ranging from the sourcing of raw materials, in-situ quality assessment and process monitoring during different stages of product manufacture [13], and the determination of active pharmaceutical ingredient (API) concentration in finished pharmaceutical products [51, 53, 54]. The use of NIRS was documented and recommended in the relevant industrial quality control guidelines published by International Conference on Harmonization (ICH), and adopted by the relevant regulatory bodies *i.e.* CPMP (Committee for Proprietary Medicinal Products) in the EU, and FDA (Food and Drug Administration) in the USA [55]. It has been shown that the use of NIRS in conjunction with conventional imaging techniques offers the most efficient means to collect spectral data and spatial information used for monitoring the distribution of constituent compounds and overall structural integrity of pharmaceutical tablets [56].

Studies in the medical field have also been performed, and have highlighted the complexities involved in modelling the interaction of an interrogating signal comprised of visible or NIR radiation with biological tissue [57, 58]. The extraction of useful information from such experiments continues to be a challenge in a number of applications, primarily due to the complex structure of biological specimens such as human skin. It has emerged that visible radiation does not penetrate appreciably beyond a few millimeters in such cases. Although NIR signals penetrate to greater depth, their transmission is strongly attenuated due to strong scattering. Although scattering remains a challenge at longer wavelengths in the infrared region, the main impediment to

transmission in the far-infrared region is water, which is one of the main constituents of biological tissue, and exhibits strong absorption characteristics at such wavelengths [59]. With advances in medical research, NIRS has been successfully employed to test various characteristics of neonatal subdermal blood flow [60]. However, a wider scope of use for the technique has remained somewhat elusive, owing to the different structure and makeup of adult tissue and skin. Nevertheless, one of the main applications of NIRS in this context has been in the monitoring and imaging of human brain [61, 62]. This has included the use of the technique in detection of control signals in the brain [63-66], and measuring cerebral blood oxygenation levels [59, 67-70]. The latter application has been extended in neonatal care to monitor cerebral blood flow and measure cerebral blood volume [71-74]. In assessing the relative merits of NIRS and pulse oximetry, it has been concluded that compared with pulse oximetry, NIRS offers greater advantages in terms of better tissue penetration and a global assessment of blood oxygenation [59].

In addition to the areas mentioned above, NIRS has been employed in analytical studies involving a diverse range of analytes such as petroleum products [75-79], animal feeds [80-83], textiles [84-87] and lately, measures concerning environmental implications [14, 88]. The list of applications continues to grow and evolve at pace with advances in the relevant technologies, reflecting the potential of the technique as a strong analytical tool.

1.2.5 Advantages

The exploitation of the NIR frequencies for spectroscopic analysis offers several advantages, some of which are outlined below.

1.   NIR spectra of a specimen offer a rich resource of qualitative as well as quantitative information about the composition of that specimen, and allow valuable analyses to be drawn despite the increased complexity of these spectra compared with infrared spectra.

2.   NIRS-based applications enjoy an inherent degree of robustness in that, spectral data can be collected with minimum to no sample preparation [16]. However, some improvement in the quality of spectra can be achieved with sample preparation.

Chapter 1: NIR spectroscopy: Background, theory and applications

3.   Contingent on its careful deployment, NIRS offers an accurate, non-invasive, non-destructive and rapid analytical approach [13], providing data at allow the determination of the compositional, spatial and spectral characteristics of the sample under test [15].

4.   The technique offers a high throughput rate, which enables its use in industrial applications that depend on real-time in-situ monitoring of specific analytes.

5.   In chemical analysis applications, the choice of NIRS over other competing techniques can offer a less complicated solution, as it allows a simpler approach to performing concurrent quality assessment of multiple samples based on simultaneous analysis of multiple analytes.

6.   Based on significant advances in instrumentation and spectral processing methods, the technique provides a rugged yet sensitive and versatile analytical tool for industrial scanning applications [56].

7.   Compared with mid-IR spectroscopy, NIRS provides better spatial resolution and higher signal-to-noise ratio with the same transmitted power level and similar scan geometry.

8.   The instrumentation used for NIRS is comprised of low-cost optical components and optical fibre cables, which renders this a cheaper option than other analytical techniques.

9.   An important additional point is that NIR transmission through visible dyes is often very good; in addition, high absorption that is seen at longer wavelengths due to primary absorption bands is not present. Hence, it is likely that higher signal levels in a security screening application might be expected than if either visible or mid IR/far IR signals are used.

1.3 Theoretical overview

A brief theoretical overview of NIRS is presented below, starting with the basic concept, followed by some specific details of the mechanisms involved, and finally with a description of the methods by which typical spectroscopic measurements are made.

1.3.1 Foundation

As explained in Section 1.2.1, the electromagnetic spectrum is comprised of radiation with a wide range of frequencies, and the energy of the radiation is a function of the

relevant frequency, measured using the relationship in (1.2). Moreover, the interaction of this radiation with matter may be characterised by absorption and scattering of the radiation, where scattering represents a generic phenomenon encompassing the mechanisms by which light is reflected, refracted and diffracted by the matter. The study of these interactions between electromagnetic radiation and matter falls under the general heading of light spectroscopy, and is carried out by means of a spectrum, which is a plot of the results of these interactions against the wavelength of the radiation. Spectra are obtained through the use of spectrometers, which are optical devices designed to analyse the overall spectral response as a function of wavelength.

All matter is composed of groups of atoms, or molecules, which vibrate at certain frequencies. The fundamental frequencies of molecular vibrations correspond to the frequencies in the mid and far IR range [14]. Note that molecular vibrations are not entirely dependent on external stimuli, as atoms remain in a state of random motion about their mean positions even at equilibrium. However, when the frequency of incident radiation matches that of the relevant molecular transitions, a transfer of energy takes place from the radiation to the molecules, or in other words the radiation is absorbed by the molecules, setting off their transitions to higher excitation states [15]. Absorption spectroscopy is thus performed by measuring the intensity of the radiation after it has interacted with a particular material sample, and comparing this intensity with a reference level to deduce which wavelengths have been absorbed by the sample.

Hence, NIRS is based on the interactions between NIR signals and the given material samples. The NIR spectrum obtained with a homogeneous sample contains features that are characteristic of that sample, and is comprised of unique spectral signatures of the constituent molecular groups. These features thus provide vital information about the compositional and quantitative makeup of that sample [15]. In case the sample is heterogeneous in nature, the resulting spectrum is more complicated; however, the constituents of the sample can still be determined through a careful appraisal of the spectral signatures present in the relevant spectrum. This ability to classify most samples based on their NIR transmittance or reflectance spectra remains at the heart of, and continues to drive, all research in this field.

1.3.2 Origin of absorption bands

As outlined earlier in Section 1.2, NIR spectra result from overtones and combinations of the fundamental modes of molecular transitions at frequencies in the mid-IR range. The origin of these modes is in the vibrations that occur in the bonds of functional chemical groups, leading to absorption of incident radiation at frequencies that match the frequencies of molecular transitions to higher energy levels [20]. In order to understand the origin of these absorption bands, it is useful to model the vibrations of atoms that constitute the chemical bonds as an approximation of the simple harmonic motion of a diatomic oscillator.

1.3.2.1 Harmonic oscillator

From the perspective of classical mechanics, an understanding of the vibrations of atoms in chemical bonds could be gained by modelling it on the harmonic motion of a simple vibrating system shown in Figure 1.3.
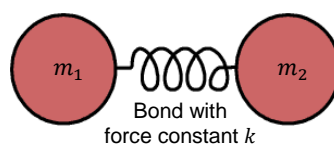
Figure 1.3 – A simple diatomic oscillator.

This model is comprised of two masses m_1 and m_2, which depict the nuclear mass of the two atoms in such an oscillator. These masses are joined together by a spring, which is analogous to the inter-nuclear forces that exist between two such atoms participating in a chemical bond. This is coherent with the relevant laws of physics, which describe the manner in which these forces attract and repel the nuclei towards and away from each other to constrain the vibrations of the participating atoms in accordance with the magnitude of these forces and the combined nuclear mass [21]. In a simple diatomic oscillator as shown in Figure 1.3, the inter-nuclear forces are modelled by the force constant, or stiffness, of the bond, which reflects the strength of the bond, and is analogous to spring constant. The frequency of the vibrations is then a function of the force constant and the combined nuclear mass [14]:

$$\nu = \frac{1}{2\pi}\sqrt{\frac{k}{\mu}} \tag{1.5}$$

Chapter 1: NIR spectroscopy: Background, theory and applications

where ν is the vibrational frequency, while k is the force constant of the bond, and μ is the product of the two nuclear masses divided by their sum, termed 'reduced molecular mass':

$$\mu = \frac{m_1 \cdot m_2}{m_1 + m_2} \qquad (1.6)$$

As chemical bonds incorporate unique values of k, the frequency ν of molecular vibrations is specific to the type of inter-atomic bonding in the molecules [21], and is therefore very sensitive to the structure of the compound being tested.

The potential energy E_p of a diatomic oscillator vibrating at ν is a function of inter-nuclear distance [21], and is given by a relationship that is similar to that for an analogous mass/ spring system [14]:

$$E_p = \frac{1}{2}k(r_t - r_e)^2 = \frac{1}{2}kr^2 \qquad (1.7)$$

where r represents the displacement of the atoms from equilibrium, while r_t and r_e are, respectively, the total inter-nuclear distance and the inter-nuclear distance at equilibrium. A graph showing the parabolic variation in E_p with r_t is given in Figure 1.4. As seen, this represents the behavior expected within elastic limits in accordance with Hooke's law [89] in that, when the atoms move closer together than the point of equilibrium, inter-nuclear electrostatic forces of repulsion come into play, and when they move apart beyond the point of equilibrium, such motion is opposed by similar forces of attraction. In both cases, the magnitude of E_p in the bond builds up till the maxima of E_p occur and the motion ceases, before re-initiating in the opposite direction. As mentioned earlier, this oscillatory behaviour exists in chemical bonds even in the absence of external stimuli, as atoms in molecules are in a perpetual state of random motion about their mean positions. However, the amplitude of such vibrations is small. If this amplitude increases, there is a limit, again as per Hooke's Law, up to which the bond remains elastic. The value of E_p when the bond is stretched to such limiting distance is termed as 'bond energy'. If this limit is exceeded, the bond is permanently weakened, which can lead to its breakage and dissociation of the participating atoms, resulting in disintegration of the molecule.

Chapter 1: NIR spectroscopy: Background, theory and applications
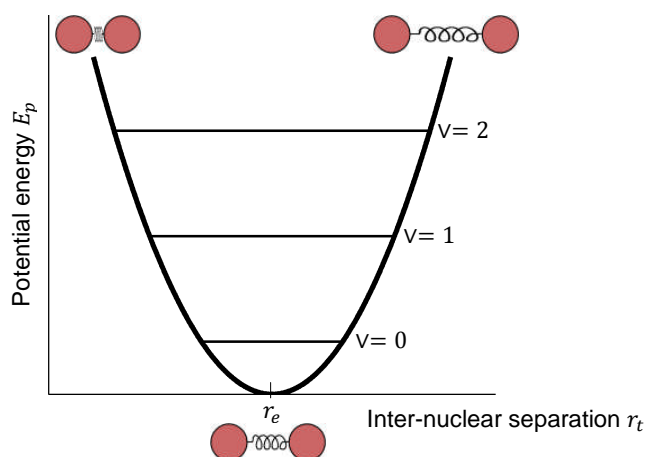
Figure 1.4 – Potential energy curve for the harmonic motion of a diatomic oscillator.

From a quantum mechanical perspective, the vibrational energy of a molecule can only have certain discrete values, which are termed as the energy levels of the molecule. In the case of a diatomic molecule executing harmonic vibrations as above, these energy levels are given by [14]:

$$E_{\text{vib}} = h\nu \left(\vee + \frac{1}{2}\right) \tag{1.8}$$

where h and ν are, respectively, Plank's constant and the classical frequency of harmonic oscillations as given in (1.5), while $\vee$ denotes the vibrational quantum number, which takes integer values 0, 1, 2, 3 …

In addition to the expression in (1.8), energy levels are expressed in terms of wavenumber (cm^{-1}). From (1.4) and (1.8), the relevant expression can be derived as follows:

$$\bar{\nu}_{\text{vib}} = \frac{E_{\text{vib}}}{hc} = \bar{\nu} \left(\vee + \frac{1}{2}\right) \tag{1.9}$$

where $\bar{\nu}$, as shown in (1.3) and (1.4), is the classical wavenumber of the harmonic oscillations. As seen in (1.8) and (1.9), and depicted in Figure 1.4, the vibrational energy of the molecule at $\vee = 0$, *i.e.* in the ground state, is not zero. This ground vibrational energy is termed as zero-point energy, and it enables the molecule to exhibit low-amplitude vibrations even at 0 K.

Based on the above, a molecule can exist at a number of vibrational excitation levels determined by the value of $\vee$. These levels are shown on the vibrational energy scale in

Figure 1.4, and illustrated in Figure 1.5 on the wavenumber scale as derived from (1.9), along with the fundamental and 'hot band' transitions that molecules undergo between these levels.
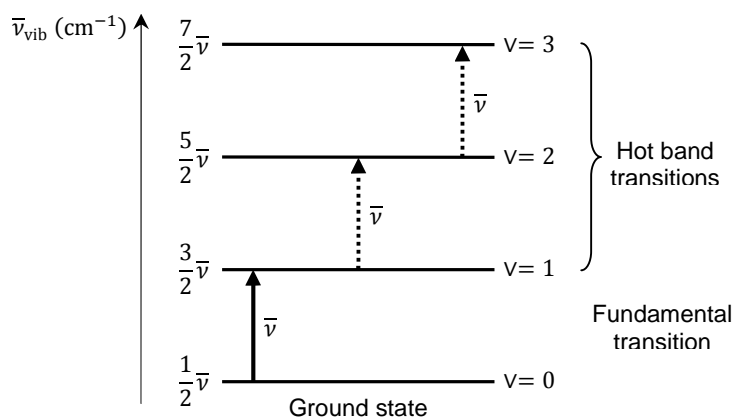
Figure 1.5 – Vibrational energy levels of a harmonic diatomic oscillator [14].

The energy levels that a molecule is allowed to attain in a given scenario is dependent on which of the transitions are permitted under a quantum-mechanical selection rule [90]. This rule, as it relates to vibrational spectroscopy, is dependent on the value of the transition moment integral:

$$T_{V' \to V''} = \int_{-\infty}^{\infty} \psi_{V''}^{*} \varepsilon \psi_{V'} d\tau \tag{1.10}$$

This represents the transition from excitation state V' to V'', where $\psi_{V'}$ and $\psi_{V''}$ are the wave functions of the vibrations at each of these levels ($\psi_{V''}^{*}$ is the complex conjugate of the relevant wave function), while ε is the transition moment operator. In this case, ε represents the dipole moment of the molecule which, for small values of displacement r about the equilibrium position, varies linearly with r:

$$\varepsilon = \varepsilon_0 + \left(\frac{d\varepsilon}{dr}\right)_e r \tag{1.11}$$

As per the selection rule, if the transition moment T in (1.10) evaluates to zero, the particular transition is forbidden. Short of evaluating the integral to determine its exact value, the symmetry of the transition moment function $\psi_{V''}^{*} \varepsilon \psi_{V'}$ in (1.10) provides an indication of the value of the integral; in transitions where this function is symmetric, T evaluates to a non-zero quantity, and the relevant transitions are allowed. In the case under discussion, this function is deemed to become symmetric only when a particular

transition instigates a change in the dipole moment ε of the molecule. In a qualitative sense, this represents the case where the oscillating dipole couples with the electric field of the impinging radiation in a way that energy transfer can take place from the radiation to the molecule.

The quantum mechanical model imposes a further restriction on permissible transitions in that, the vibrational quantum number $\vee$ can only change by one unit in either direction. Thus, a single transition is not allowed to span multiple energy levels.

Hence, based on the two conditions outlined above, a transition can take place only if:

$$\left(\frac{d\varepsilon}{dr}\right)_e \neq 0 \Rightarrow \text{T} \neq 0, \text{ and } \Delta \vee = \pm 1 \tag{1.12}$$

The amount of energy required to excite a molecule to a higher energy level is laid out in the Bohr-Einstein Law, which states that the energy of incident radiation must be the same as the energy gap between excitation states to enable the molecule to make the said transition [15, 21]:

$$\Delta E = E'' - E' = h\nu \tag{1.13}$$

where E'' and E' are permissible energy levels, while $\Delta E = h\nu$ represents the radiation energy which, if incident on the molecule, would be absorbed to produce the required change in dipole moment ε, hence exciting the molecule from level E' to E''.

In accordance with Boltzmann distribution [91], the majority of molecules at room temperature reside in the ground excitation state. Hence, in the presence of the required radiation energy signal, the predominant transition that takes place is from $\vee = 0$ to $\vee = 1$. Known as fundamental transition as shown in Figure 1.5, this transition dominates all absorption spectra in the infrared region, and forms the basis of the bulk of spectroscopic analysis carried out in this region. The remaining transitions originate from higher excitation levels; however, due to the low molecular populations at these levels (at room temperature), the corresponding absorption bands are much weaker than the fundamental band. The designation of these higher-level transitions as 'hot band' transitions as seen in Figure 1.5 reflects the fact that if the temperature is increased, the

inherently low molecular populations at these higher energy levels get augmented which, in turn, leads to an increase in the intensity of the relevant absorption bands.

As shown in Figures 1.4 and 1.5, the energy levels of a harmonic oscillator are equally spaced, *i.e.* the frequency of fundamental transition is the same as the frequency of each of the successive hot band transitions. Taking into account the criteria for permissible transitions laid out under the relevant selection rule in (1.12), this precludes the existence of overtone and combination bands. However, as the very existence of these bands forms the basis of NIR spectroscopy, it is important to derive a more realistic approximation of molecular transitions based on an anharmonic oscillator.

1.3.2.2 Anharmonic oscillator

The existence of anharmonicity, or departure from ideal harmonic behaviour, is readily observed during experiments in vibrational spectroscopy [14, 15]. It is noted that the transitional frequencies of different hot bands (ref. Figure 1.5) are not the same, and are different from the frequency of fundamental transition as well. Additionally, it is seen that the second part of the criteria for permissible transitions laid out in (1.12), *i.e.* $\Delta v = \pm 1$, does not always hold true, in that transitions across multiple energy levels such as $v = 0 \rightarrow v = 2$ or 3 can be observed. These effects are the result of two underlying phenomena, which affect all spectroscopic measurements to varying degrees.

The first of these phenomena is termed as 'mechanical anharmonicity', and arises from the fact that in a practical scenario, the expression for oscillator energy E_p is not purely quadratic in r as given in (1.7), but involves higher order terms as well:

$$E_p = \frac{1}{2}kr^2 + k'r^3 + \cdots \qquad (k \gg k') \qquad (1.14)$$

Consequently, the energy levels permitted for an anharmonic oscillator are not the same as those given by the relationship in (1.9), but are modified as per the relevant solution of the Schrödinger equation. This is obtained by using the expression in (1.14) in the Schrödinger equation, and applying an approximation method to arrive at the following relationship:

$$\bar{v}_{\text{vib}} = \frac{E_{\text{vib}}}{hc} = \bar{v}\left(v + \frac{1}{2}\right) - x_a\bar{v}\left(v + \frac{1}{2}\right)^2$$

$$= \bar{v}\left(v + \frac{1}{2}\right) - X\left(v + \frac{1}{2}\right)^2 \tag{1.15}$$

Here, x_a represents a quantity known as the anharmonicity constant, which has unique values for particular molecular bonds and the types of vibrations they undergo. In the second expression above, $X = x_a\bar{v}$. The energy levels thus obtained in (1.15) for an anharmonic oscillator are shown alongside those of a harmonic oscillator for successive values of v in Figure 1.6.
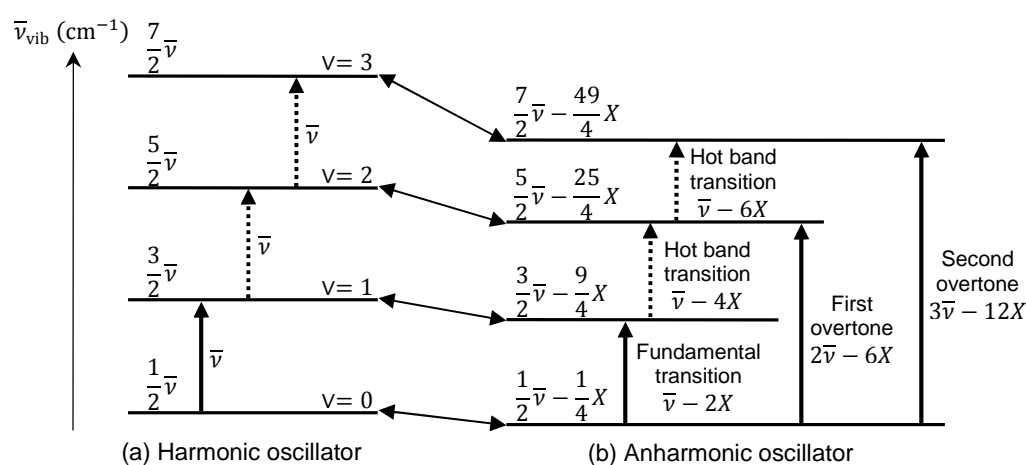
Figure 1.6 – Vibrational energy levels and permissible transitions of (a) a harmonic diatomic oscillator, and (b) an anharmonic oscillator [14].

As seen in Figure 1.6(b), with the introduction of anharmonicity, the successive energy levels are no longer equally spaced and tend to close in together, so that the magnitude of hot band transitions grows progressively smaller as the value of v increases. The ground state ($v = 0$) is affected as well, so the anharmonic oscillator incorporates lower vibrational energy at each excitation level as compared with the corresponding energy levels of the ideal harmonic oscillator.

The potential energy curve of an anharmonic oscillator follows a trajectory defined by the Morse function [14, 92]:

$$E_p = E_d\left[1 - e^{-\beta(r_t - r_e)}\right]^2 = E_d\left(1 - e^{-\beta r}\right)^2 \tag{1.16}$$

where β is a constant, while E_d is the dissociation energy of the oscillator, given as [93]:

$$E_d = \frac{\bar{v}}{4x_a} \tag{1.17}$$

Figure 1.7 shows a plot of the Morse function in (1.16) against inter-nuclear distance r_t, along with the corresponding energy function of the harmonic oscillator (ref. (1.7) and Figure 1.4) for comparison.
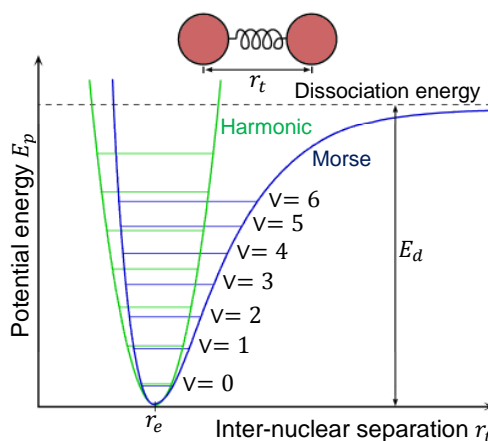
Figure 1.7 – Potential energy curve for a harmonic oscillator, and the Morse curve for an anharmonic diatomic oscillator.

As seen, the value of E_d is measured from the bottom of the Morse curve, and represents the bond energy which, if acquired by the oscillator on positive displacement (stretch), leads to the dissociation of the bond. This implies that anharmonic oscillators can withstand compression better than stretching, as the bond simply dissociates if a certain limit is exceeded while stretching.

The second phenomenon that dictates the behaviour of an anharmonic oscillator is termed "electrical anharmonicity", and is manifested by way of transitions that span more than one energy level, *i.e.* $\Delta v > 1$. Such transitions are known as overtones. The higher excitation energy required for realizing these transitions, as depicted in Figure 1.6, leads to the occurrence of the relevant absorption bands in the NIR region. The presence of these overtones owes to the fact that the dipole moment ε of an anharmonic oscillator is not linear in r, but includes higher order terms as well, so that the expression of ε for harmonic oscillator as given in (1.11) is modified as below:

$$\varepsilon = \varepsilon_0 + \left(\frac{d\varepsilon}{dr}\right)_e r + \frac{1}{2}\left(\frac{d^2\varepsilon}{dr^2}\right)_e r^2 + \cdots \tag{1.18}$$

Chapter 1: NIR spectroscopy: Background, theory and applications

As illustrated in Figure 1.6(b), the transitional frequency (or wavenumber) of the overtones is not an exact multiple of the absorption frequency of fundamental transition. As explained above, this is a consequence of mechanical anharmonicity, which results in consecutive hot band transitions that have progressively lower amplitudes than the amplitude of fundamental transition.

Taking into account the values of $\bar{\nu}$ and x_a for various chemical functional groups, it becomes clear that the majority of absorption spectra in the NIR region result from overtone transitions [94]. Additionally, it is seen that the intensity of these overtone absorption bands is directly proportional to the magnitude of anharmonicity in the relevant functional groups [95]. For instance, the XH stretching transitions (including CH, NH and OH bonds) have the highest values of x_a, and therefore dominate the overtone absorption bands. Conversely, the carbonyl stretching modes have very small values of x_a, leading to the exceedingly weak/ low-intensity overtone spectra of this group.

1.3.3 Overtone and combination bands

As elaborated in the preceding section, no fundamental vibrational transitions take place at NIR frequencies. While the frequencies of these transitions belong in the mid and far-IR regions, their overtones and combinations occur at higher frequencies, which are in the NIR region. Further, the overtones are not exact multiples or harmonics of the pertinent fundamental frequencies but, depending on the extent to which the relevant vibrational modes are anharmonic, occur at transitional frequencies that are less than exact multiples. Additionally, the intensity of higher overtone bands progressively decreases [15], again subject to the extent to which the relevant molecular oscillations are anharmonic – high anharmonicity produces higher intensity overtones and vice versa – and they tend to be broader in profile that the fundamental absorption bands as well [16]. The general layout of the overtone and combination regions, along with the main absorption bands that occur in each case, is shown in Figure 1.8. While most of the relevant bands tend to be relatively broad, they still offer a valuable resource of qualitative information about the composition of the molecules whose vibrations give rise to these bands. With careful analysis of the location of these bands on the wavelength scale, the identity of the relevant molecular transitions, and hence the

composition of the test samples, can be determined. Besides the magnitude of anharmonicity impacting the intensity of these bands, the physical structure of the test sample may affect the intensity of the spectra as well. For instance, a denser sample might produce more representative spectra with better wavelength resolution and cleaner layout than a highly porous sample, as the latter might severely scatter the impinging radiation to adversely affect the intensity, resolution and overall quality of the resultant spectra [96].
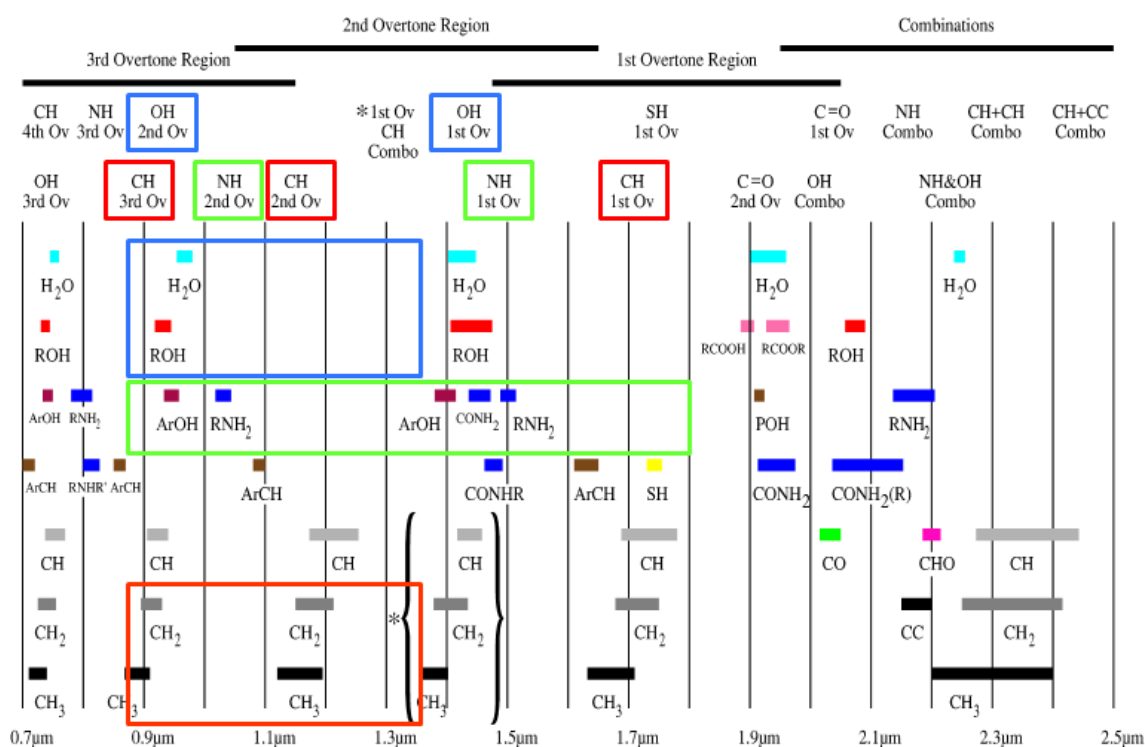
Figure 1.8 – The layout of spectral absorption bands in the NIR region, comprising higher order overtones and combinations of fundamental transitions [21].

In case the molecular structure of the test sample is comprised of complex molecules containing multiple functional groups of atoms, where vibrational transitions of each of these functional groups produce different overtone and combination absorption spectra, qualitative and quantitative information about the substance can be gleaned from the spectra by characterizing the absorption bands belonging to the various functional groups. However, the allocation of characteristic absorption bands to specific functional groups in such cases is not straightforward [16]. This arises from the fact that complex molecules can have a substantial number of distinct vibrational modes and frequencies: A molecule with N atoms possesses $(3N - 6)$ vibrational degrees of freedom, which account for $(3N - 6)$ modes of vibration with distinct fundamental transitional

frequencies, also referred to as 'normal' modes of vibration [14, 24]. Each normal mode signifies a particular instance where all the atoms constituting the molecule vibrate in phase at the same frequency, albeit with different amplitudes. Hence, the difficulty in assigning characteristic absorption bands to a specific molecule is a direct consequence of the large number of absorption bands that a single molecule can produce. Moreover, the fundamental transitional frequencies of all the relevant vibrational modes are not necessarily mutually different, so that multiple vibrational modes, called degenerate modes, can have the same fundamental frequency. Finally, the transitions arising from distinct vibrational modes with different fundamental frequencies can overlap to produce hybrid or combination spectral bands. The frequency at which a particular combination absorption band occurs denotes the sum of the fundamental transitional frequencies of participating vibrational modes [15]. As a result, such combination spectra can be poorly resolved in frequency/ wavelength, rendering it difficult to assign them to particular analytes, thus complicating the overall spectral profiles. As seen in Figure 1.8, combination bands appear in the longer wavelengths of the NIR region.

In view of the above factors, a chemometrics-based approach is generally considered essential to effectively use NIR spectra for requisite qualitative and quantitative analyses [97]. A number of multivariate calibration techniques exist to realize such an approach, where each technique offers certain advantages and limitations in specific applications [98]. The factors affecting the choice and application of techniques used in the course of this work are discussed alongside the relevant experimental details in the following chapters.

1.3.4 Modes of molecular vibrations

All molecular vibrations that produce overtone and combinational transitions that result in the appearance of the relevant absorption bands in the NIR region, fall into two main categories, namely stretching and bending vibrations [20]. Further, stretching vibrations can take place either symmetrically or asymmetrically. In the case of symmetric stretching, there is a possibility that the vibrations do not incur a change in the dipole moment ε of the molecule. As change in ε is a prerequisite (as explained in Section 1.3.2) for transfer of energy to take place between the radiation and the molecule so as

to excite the molecule to a higher energy level, such transitions remain inhibited in this case. As a result, such vibrations do not produce any absorption spectra.

The geometrical orientation of the two vibrational modes dictates that during stretching vibrations, the length of the bonds changes, while bending vibrations produce changes in the angle of the host bonds [20]. It has been shown that stretching vibrations inherently require higher energy to execute, and therefore, in accordance with the relationship in (1.2), occur at higher frequencies in a particular excitation state as compared with bending vibrations.

The vibrational modes of a CO_2 molecule [99] are illustrated in Figure 1.9. In this case, the symmetric stretching mode does not trigger a change in ε and therefore, does not contribute to the relevant NIR absorption spectra. Accordingly, this mode is not deemed to be 'IR active' in this case, as opposed to the other three modes which are responsible for vibrational transitions that result in the appearance of CO_2 spectral bands.
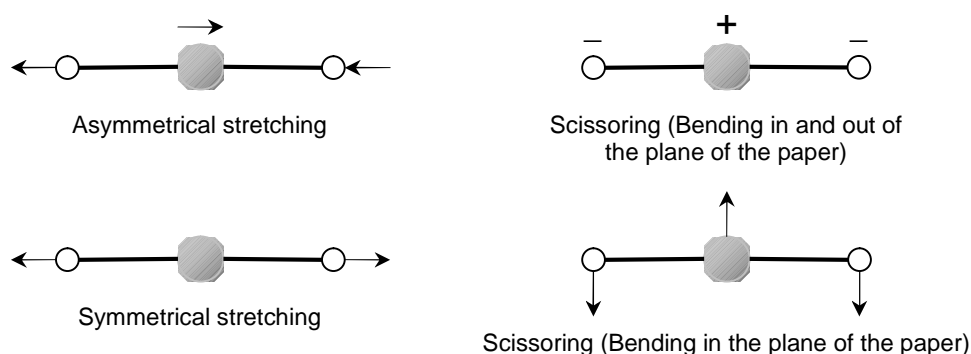
Figure 1.9 – Stretching and bending vibrational modes in a CO_2 molecule [99].

1.4 Modes of spectroscopy

1.4.1 Measurements using relative absorbance

In accordance with a basic convention, amplitude spectroscopic measurements are carried out in terms of relative, rather than absolute, absorbance values. This precludes the need to make measurements against a universal standard on a given scale, but rather presents measured values as dimensionless quantities in terms of absorption relative to a local reference level, as outlined below.

The spectral measurements are normally recorded as optical intensity spectra over a certain wavelength range, obtained with the help of an appropriate optical instrument such as a light spectrometer. Two sets of measurements are recorded: an initial reading is taken to record intensity across a reference material/ sample, and then similar readings are taken for all other test samples. The following relationship is then used to calculate spectral absorbance for each sample:

$$A(\lambda) = -\log_{10}\left[\frac{I(\lambda)}{I_0(\lambda)}\right] \qquad (1.19)$$

where A is the relative absorbance of a given test sample as a function of wavelength λ, while I and I_0 are the intensity spectra collected with the test sample and the reference sample respectively. As seen, the values of A are dimensionless, and signify the signal amplitude measured with the sample relative to the reference. Note the −ve sign in (1.19) allows positive values of A in the majority of cases where the recorded amplitudes of I are less than those of I_0. The resulting absorbance A may then be construed as an interpretation of the absolute absorption:

$$A(\lambda) = A^*(\lambda) - A_0^*(\lambda) \qquad (1.20)$$

where A^* and A_0^* represent the absolute absorbance values at wavelengths λ for the test and reference samples respectively. Sets of measurements are performed with constant A_0^*, or I_0 in actual terms, so as to maintain consistency and enable appropriate comparisons to be drawn between the values of spectral absorbance A measured with different test samples.

Reference intensity I_0 is conventionally recorded across a reference material such as a ceramic plate, or can be taken as the total incident intensity level recorded without a sample. In reflectance mode (explained below), another suitable material such as PTFE may be used as the reflective surface to obtain the reference I_0.

1.4.2 Methods of presenting test samples

Different scan geometries can be used to set the relative positions of the radiation source, the sample being tested, and the detector. The choice depends on the type of application, and the physical structure of the test sample. The four main methods of

presenting samples in NIR spectroscopic measurements are illustrated in Figure 1.10 [14].

Transmittance

Reflectance

Transflectance

Interactance

Optical fibre arrangement
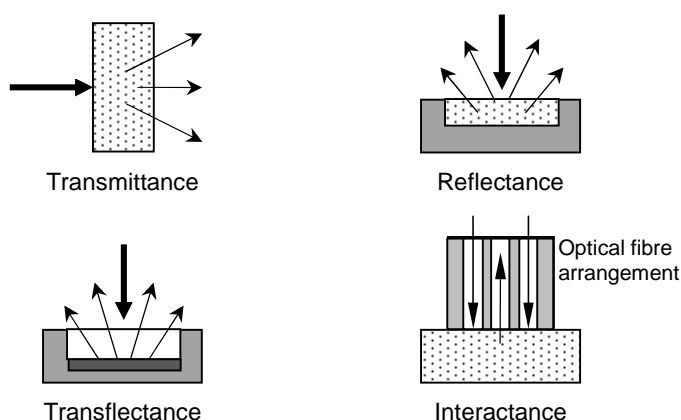
Figure 1.10 – Different methods of presenting samples, including transmittance, reflectance, transflectance and interactance, used to collect NIR spectral data [14].

1.4.2.1 Transmittance

The transmittance method is widely used to test samples that allow measureable signal levels to travel across, and is especially popular for testing liquid samples. Here, the incident signal is directed on the surface of the test sample which, in the case of liquids, can be held in a suitable container such as a cuvette, and the intensity signal that traverses the sample to the opposite side is recorded and processed to obtain requisite absorbance values. One of the widespread applications of this method has been in the pharmaceutical industry, where it has been found to provide more accurate results, less affected by features such as embossing on the tablets, than the other methods [100].

1.4.2.2 Reflectance

In the reflectance mode, the radiation source and the detector are positioned on the same side of the test sample, and diffuse reflected signal from the sample is measured. The sample in this case must be appropriately opaque, such as a powder or a thick colloidal suspension, and have sufficient depth to reflect the impinging radiation. While the depth deemed to be suitable is dependent on the magnitude of incident radiation, in view of the transmission characteristics of NIR signals, a depth of 1 cm is usually considered as the minimum essential to make reliable measurements in reflection. Additionally, care must be exercised in setting the geometrical layout of the optical bench, so that the orientation of the detector relative to the source and the sample allows only diffuse reflection off the sample to be recorded, while ensuring that no part of the received

signal is contaminated by any specular reflection. The recorded measurements are then comprised purely of the diffuse reflected signal from the surface and the layers closest to the surface of the sample. The technique has been employed in various quality control applications, including testing the physical characteristics and Brix values of fresh fruit [101, 102].

1.4.2.3 Transflectance

The transflectance mode of measurement presents a combination of transmittance and reflectance modes. As depicted in Figure 1.10, the incident signal traverses the sample, which in this case is either relatively transparent, such as a liquid held in a glass cell, or a sufficiently thin layer of another material (or possibly both), and is back-scattered off the surface of a suitable reflector. The materials generally used to provide a uniform diffuse reflective surface include PTFE, ceramic and aluminium [103]. One of the applications of this method is in the food processing industry, where it is used, for example, to test samples for adulterants or other analytes [104, 105].

1.4.2.4 Interactance

The interactance mode of measurement is realized through the use of a concentric ring of radiation sources and a central detector, with the entire arrangement held either in contact with, or sufficiently close to, the surface of the sample. This arrangement is usually comprised of a number of optical fibre cables arranged in a ring formation used to illuminate the sample, and a concentric central fibre to record the signal transmitted through the sample to the receiving aperture. The outer illuminating fibres may be angled inwards to allow a region in the sample where the fields of view of the illuminating and the detecting fibres overlap. Some probes allow adjustment of the depth of this overlap by controlling the pitch of the illuminating fibres [106]. The use of the method has been reported in various test applications, such as measuring the Brix value of peaches [107].

1.5 Scope of work

As shown in Section 1.2.3, NIRS has found application in several industries as a powerful analytical tool. The utility of this technique is based in all applications on the extraction of qualitative and quantitative information about the various compositional

properties of the samples under test. It is, therefore, perceivable that the technique could be used to identify unknown samples by identifying any characteristic features in the spectra of the relevant samples. As the spectral information obtained in NIR scans often includes characteristics that are entirely material-specific [23], such information would prove invaluable in the requisite identification process. This approach could, therefore, be employed as the means to detect specific substances controlled by customs or deemed to be dangerous or harmful in a security screening perspective. Further, if the technique were to be considered for scanning/identifying samples concealed behind clothing or similar materials, tests would need to be conducted to establish the influence of such intervening layers on the interrogating NIR signal.

The above considerations form the basis of this work, aimed at detecting, identifying and possibly quantifying specific chemicals hidden behind clothing. The work was planned so that the scanning approach and instrumentation developed to perform the scans would conform to the principles of conventional NIRS. However, the application was modified in certain respects, for instance by performing measurements at a standoff distance, to reflect its potential use in a practical security screening system. The technique was employed to identify specific chemicals, and perform cross-sectional surface scans of the samples for spectroscopic imaging. It may be noted that the use of NIRS to detect and characterise chemicals hidden behind clothing is a novel proposition, which does not seem to have been considered to date as a primary candidate for through-clothing personal screening, outside of the work published by members of the research group at Warwick.

1.6 Conclusions

In recent decades, NIRS has emerged as a leading analytical tool used to perform qualitative and quantitative analyses of samples in multifarious applications spanning various industries. This owes to the many advantages this technique has to offer including, amongst others, inexpensive portable instrumentation, high data throughput rate and rich spectral content.

The origin of the spectral bands that appear in the NIR region can be traced to anharmonic molecular vibrational transitions, which are overtones and combinations of

the fundamental transitions. Such spectral content can be used to assign characteristic bands to various functional groups, and by extension, to specific molecular structures. However, the nature of the overtone and combination bands complicates this process, and necessitates a chemometrics-based approach to the problem. The technique can be applied in different modes of sample presentation, where each offers certain advantages in specific applications.

In the following chapters, studies are presented that have been carried out to test and categorize various fabric materials, and to identify and quantify specific chemicals hidden behind single fabric layers, using optical instrumentation and software systems designed and developed for the purpose.

1.7 References

[1] S. Singh and M. Singh, "Explosives detection systems (EDS) for aviation security," *Signal Processing,* vol. 83, pp. 31-55, 2003.

[2] G. M. Stone, "Application and limitations of advanced technologies in explosives detection," in *Proceedings of the 1990 International Carnahan Conference on Security Technology: Crime Countermeasures, October 10, 1990 - October 12, 1990*, Lexington, KY, USA, 1990, pp. 81-87.

[3] S. Kumar, W. C. McMichael, E. E. Magnuson, Y. K. Lee, C. R. Moeller, P. V. Czipott, T. J. Rayner, D. E. Newman and D. Wroblewski, "Liquid contents verification for explosives, chemical agents, and dissolved narcotics," in *Enabling Technologies for Law Enforcement and Security, November 5, 2000 - November 8, 2000*, Boston, MA, United states, 2001, pp. 206-216.

[4] H. Itozaki and Y. Yamauchi, "Liquid explosive detection from outside of the bottle by IR," in *Proceedings of SPIE - The International Society for Optical Engineering - Infrared Technology and Applications XXXV, April 13, 2009 - April 17, 2009*, Orlando, FL, United states, 2009.

[5] H. Schubert and A. Kuznetsov, "Detection of liquid explosives and flammable agents in connection with terrorism," in *Proceedings of the NATO Advanced Research Workshop on Detection of Liquid Explosives and Flammable Agents in Connection with Terrorism*, St. Petersburg, Russia, 2008.

[6] B. A. Klock, "Usability assessment of a bottle content tester for use in airports by screeners," in *Proceedings IEEE 34th Annual 2000 International Carnahan Conference on Security Technology, 23-25 Oct. 2000*, Piscataway, NJ, USA, 2000, pp. 174-7.

[7] X.-M. Fang and Z. Xu, "Method for explosive detection using nuclear quadrupole resonance/electromagnetic induction (NQR/EMI)," *Tongji Daxue Xuebao/Journal of Tongji University,* vol. 32, pp. 632-635, 2004.

[8] CNN-Travel. (2010, 22/06/2011). *Honey leaves travelers stuck at airport for hours* [TSA]. Available: http://articles.cnn.com/2010-01-05/travel/california.airport.shutdown_1_honey-transportation-security-administration-agents-bag?_s=PM:TRAVEL

[9] G. Bunte, M. Heil, D. Ruseling, J. Hurttlen, H. Pontius and H. Krause, "Trace detection of explosives vapours by molecularly imprinted polymers for security measures," *Propellants, Explosives, Pyrotechnics,* vol. 34, pp. 245-251, 2009.

[10] M. L. Ramirez-Cedeno, W. Ortiz-Rivera, L. C. Pacheco-Londono and S. P. Hernandez-Rivera, "Remote detection of hazardous liquids concealed in glass and plastic containers," *IEEE Sensors Journal,* vol. 10, pp. 693-698, 2010.

[11] C. Connolly, "NIR spectroscopy for foodstuff monitoring," *Sensor Review,* vol. 25, pp. 192-194, 2005.

[12] P. Pallav, G. Diamond, D. Hutchins and T. H. Gan, "A near infrared technique for non-destructive evaluation," *Insight: Non-Destructive Testing and Condition Monitoring,* vol. 50, pp. 244-248, 2008.

[13] A. A. Gowen, C. P. O'Donnell, P. J. Cullen and S. E. J. Bell, "Recent applications of Chemical Imaging to pharmaceutical process monitoring and quality control," *European Journal of Pharmaceutics and Biopharmaceutics,* vol. 69, pp. 10-22, 2008.

[14] H. W. Siesler, Y. Ozaki, S. Kawata and H. M. Heise, *Near-infrared spectroscopy: principles, instruments, applications*: Wiley-VCH, 2006.

[15] B. G. Osborne, "Near-Infrared Spectroscopy in Food Analysis," in *Encyclopedia of Analytical Chemistry*, John Wiley & Sons, Ltd, 2006.

[16] B. F. MacDonald and K. A. Prebble, "Some applications of near-infrared reflectance analysis in the pharmaceutical industry," *Journal of Pharmaceutical and Biomedical Analysis,* vol. 11, pp. 1077-1085, 1993.

[17] R. C. Denney, R. Sinclair and D. Mowthorpe, *Visible and ultraviolet spectroscopy*: Published on behalf of ACOL, Thames Polytechnic, London, by Wiley, 1987.

[18] I. Kavdir, R. Lu, D. Ariana and M. Ngouajio, "Visible and near-infrared spectroscopy for nondestructive quality assessment of pickling cucumbers," *Postharvest Biology and Technology,* vol. 44, pp. 165-174, 2007.

[19] J. A. Cayuela, "Vis/NIR soluble solids prediction in intact oranges (Citrus sinensis L.) cv. Valencia Late by reflectance," *Postharvest Biology and Technology,* vol. 47, pp. 75-80, 2008.

[20] W. Volland. (1999, 13/05/2011). Organic compound identification using infrared spectroscopy. [Online primer]. Available: http://www.800mainstreet.com/irsp/eir.html

[21] I. Murray, *Scattered Information: Philosophy and Practice of Near Infrared Spectroscopy*: Scottish Agricultural College, UK, 2003.

[22] Antonine-Education. (2008, 13/05/2011). *The Electromagnetic Spectrum.* Available: http://www.antonine-education.co.uk/physics_gcse/Unit_1/Topic_5/topic_5_what_are_the_uses_and_ha.htm

[23] J. Workman, *Introduction to Near Infrared Spectroscopy*: John Wiley & Sons, 2000.

[24] W. Bruegel, A. J. D. Katritzky and A. R. Katritzky, *[Einführung in die Ultrarotspektroskopie.] An Introduction to Infrared Spectroscopy ... Translated ... by A. R. Katritzky and A. J. D. Katritzky. [With illustrations.]*. Methuen & Co.: London; John Wiley & Sons: New York, 1962, 1962.

[25] J. Rubin. (2011, 16/05/2011). *The Discovery of the Spectrum of Light*. Available: http://www.juliantrubin.com/bigten/lightexperiments.html

[26] T. Davies, "The history of near infrared spectroscopic analysis: Past, present and future - From sleeping technique to the morning star of spectroscopy," *Analusis,* vol. 26, pp. 17-19, 1998.

[27] P. Williams and K. H. Norris, *Near-infrared technology in the agricultural and food industries*: American Association of Cereal Chemists, 1987.

[28] M. Uddin, E. Okazaki, M. Uddin Ahmad, Y. Fukuda and M. Tanaka, "Noninvasive NIR spectroscopy to verify endpoint temperature of kamaboko gel," *LWT - Food Science and Technology,* vol. 38, pp. 809-814, 2005.

[29] M. Uddin, S. Ishizaki, M. Ishida and M. Tanaka, "Assessing the end-point temperature of heated fish and shellfish meats," *Fisheries Science,* vol. 68, pp. 768-775, 2002.

[30] J. B. Misra, R. S. Mathur and D. M. Bhatt, "Near-infrared transmittance spectroscopy: a potential tool for non-destructive determination of oil content in groundnuts," *Journal of the Science of Food and Agriculture,* vol. 80, pp. 237-240, 2000.

[31] B. Steuer, H. Schulz and E. Läger, "Classification and analysis of citrus oils by NIR spectroscopy," *Food Chemistry,* vol. 72, pp. 113-117, 2001.

[32] H. Huang, H. Yu, H. Xu and Y. Ying, "Near infrared spectroscopy for on/in-line monitoring of quality in foods and beverages: A review," *Journal of Food Engineering,* vol. 87, pp. 303-313, 2008.

[33] M. J. C. Pontes, S. R. B. Santos, M. C. U. Araújo, L. F. Almeida, R. A. C. Lima, E. N. Gaião and U. T. C. P. Souto, "Classification of distilled alcoholic beverages and verification of adulteration by near infrared spectrometry," *Food Research International,* vol. 39, pp. 182-189, 2006.

[34] M.-F. Laporte and P. Paquin, "Near-Infrared Analysis of Fat, Protein, and Casein in Cow's Milk," *Journal of Agricultural and Food Chemistry,* vol. 47, pp. 2600-2605, 1999.

[35] D. Behmer, "Quality control of dairy products with NIR spectroscopy," *Food Science and Technology,* vol. 23, pp. 37-38, 2009.

[36] Y.-w. Dong, Z.-h. Tu, D.-z. Zhu, Y.-w. Liu, Y.-n. Wang, J.-l. Huang, B.-l. Sun and Z.-n. Fan, "Feasibility of Using NIR Spectroscopy to Detect Melamine in Milk," *Spectroscopy and Spectral Analysis,* vol. 29, pp. 2934-8, 2009.

[37] H. Lin and Y. Ying, "Theory and application of near infrared spectroscopy in assessment of fruit quality: A review," *Sensing and Instrumentation for Food Quality and Safety,* vol. 3, pp. 130-141, 2009.

[38] D. Han and J. Wang, "Review of nondestructive measurement of fruit quality by means of near infrared spectroscopy," *Zhongguo Jiguang/Chinese Journal of Lasers,* vol. 35, pp. 1123-1131, 2008.

[39] L. Xie, Y. Ying, H. Lin, Y. Zhou and X. Niu, "Nondestructive determination of soluble solids content and pH in tomato juice using NIR transmittance spectroscopy," *Sensing and Instrumentation for Food Quality and Safety,* vol. 2, pp. 111-115, 2008.

[40] A. H. Gomez, Y. He and A. G. Pereira, "Non-destructive measurement of acidity, soluble solids and firmness of Satsuma mandarin using Vis/NIR-spectroscopy techniques," *Journal of Food Engineering,* vol. 77, pp. 313-319, 2006.

[41] W. M. Miller and M. Zude-Sasse, "NIR-based sensing to measure soluble solids content of Florida citrus," *Applied Engineering in Agriculture,* vol. 20, pp. 321-327, 2004.

[42] Y. Shao and Y. He, "Nondestructive measurement of acidity of strawberry using Vis/NIR spectroscopy," *International Journal of Food Properties,* vol. 11, pp. 102-111, 2008.

[43] Y. Jiansong, Y. Haiqing and H. Yong, "Calibrating total acidity of tomato products using GA and Vis/NIR spectroscopy," in *2009 7th Asian Control Conference, ASCC 2009, August 27, 2009 - August 29, 2009*, Hong Kong, China, 2009, pp. 1697-1700.

[44] X. Li and Y. He, "Non-destructive measurement of acidity of Chinese bayberry using Vis/NIR-spectroscopy techniques," in *4th International Conference on Photonics and Imaging in Biology and Medicine, September 3, 2006 - September 6, 2006*, Tianjin, China, 2006, pp. National Natural Science Foundation of China; SPIE Russia Chapter; Int. Laser Center of M.V. Lomonoson Moscow State University; Bio-Optics and Laser Medicine Comm. of Chinese Optics Soc.; Science and Technology Garden of Tianjin University.

[45] R. Lu and B. B. Bailey, "NIR measurement of apple fruit soluble solids content and firmness as affected by postharvest storage," in *ASAE (American Society of Agricultural and Biological Engineers) Annual Meeting*, St. Joseph, Michigan, 2005, p. Paper number 056070.

[46] D. C. Slaughter, D. Barrett and M. Boersig, "Nondestructive Determination of Soluble Solids in Tomatoes using Near Infrared Spectroscopy," *Journal of Food Science,* vol. 61, pp. 695-697, 1996.

[47] F. Xiaping, Y. Yibin, L. Huishan, X. Huirong and Y. Haiyan, "FT-NIR diffuse reflectance spectroscopy for kiwifruit firmness detection," *Sensing and Instrumentation for Food Quality and Safety,* vol. 1, pp. 29-35, 2007.

[48] H. K. Purwadari and I. W. Budiastra, "Computer controlled on-line system for mango grading using image processing and NIR measurement," in *Proceedings of 2nd International Symposium on Mathematical Modelling and Simulation in Agricultural and Bio Industries, 7-9 May 1997*, Godollo, Hungary, 1997, pp. 259-64.

[49] C. V. K. Kandala, G. Konda Naganathan and J. Subbiah, "NIR reflectance method to determine moisture content in food products," in *Reflection, Scattering, and*

Diffraction from Surfaces, August 11, 2008 - August 12, 2008, San Diego, CA, United states, 2008, p. The International Society for Optical Engineering (SPIE).

[50] H. Forcinio, "Pharmaceutical industry embraces NIR technology," *Spectroscopy,* vol. 18, pp. 16-19+24, 2003.

[51] L. Alvarenga, D. Ferreira, D. Altekruse, J. C. Menezes and D. Lochmann, "Tablet identification using near-infrared spectroscopy (NIRS) for pharmaceutical quality control," *Journal of Pharmaceutical and Biomedical Analysis,* vol. 48, pp. 62-69, 2008.

[52] G. Reich, "Near-infrared spectroscopy and imaging: Basic principles and pharmaceutical applications," *Advanced Drug Delivery Reviews,* vol. 57, pp. 1109-1143, 2005.

[53] A. Eustaquio, M. Blanco, R. D. Jee and A. C. Moffat, "Determination of paracetamol in intact tablets by use of near infrared transmittance spectroscopy," *Analytica Chimica Acta,* vol. 383, pp. 283-290, 1999.

[54] M. C. Sarraguca and J. A. Lopes, "Quality control of pharmaceuticals with NIR: from lab to process line," *Vibrational Spectroscopy,* vol. 49, pp. 204-10, 2009.

[55] *Specifications : Test Procedures and Acceptance Criteria for New Drug Substances and New Drug Products: Chemical Substances,* International Conference on Harmonisation of Technical Requirements for Registration of Pharmaceuticals for Human Use. ICH Harmonised Tripartite Guideline: Q6A - Adopted by CPMP, November 1999, issued as CPMP/ICH/367/96; FDA: Published in the Federal Register, 29 December 2000, Vol. 65, No. 251, p. 83041-63., 1999.

[56] F. W. Koehler, E. Lee, L. H. Kidder and E. N. Lewis, "Near infrared spectroscopy: the practical chemical imaging solution," *Spectroscopy Europe,* vol. 14, pp. 12-19, 2002.

[57] H. Ding, C. Su, F. Lin, F. Wang and J. Ying, "Simulation and experiment on biological tissue for near infra-red (NIR) photon migration in a multi-layered model," in *Proceedings of the 20th Annual International Conference of the IEEE Engineering in Medicine and Biology Society. Vol.20 Biomedical Engineering Towards the Year 2000 and Beyond, 29 Oct.-1 Nov. 1998*, Piscataway, NJ, USA, 1998, pp. 932-5.

[58] M.-C. Pan, W.-H. Huang, C.-H. Chen and M.-C. Pan, "NIR electro-optical measurement for pseudo-models of biological tissues," in *Optical Methods for Tumor Treatment and Detection: Mechanisms and Techniques in Photodynamic Therapy XV, January 21, 2006 - January 22, 2006*, San Jose, CA, United states, 2006.

[59] H. Owen-Reece, M. Smith, C. E. Elwell, J. C. Goldstone and D. T. Delpy, "Near-infrared spectroscopy and cerebral hemodynamics," *Critical care medicine,* vol. 24, pp. 1424-5, 1996.

[60] C. Araujo Andrade, F. Ruiz, J. Refugio Martinez Mendoza, F. Escalante Padron and J. F. Hernandez-Sierra, "Feasibility for non invasive estimation of glucose concentration in newborns using NIR spectroscopy and PLS," in *Medical Physics. Ninth Mexicon Symposium on Medical Physics, 18-21 March 2006*, USA, 2006, pp. 224-6.

[61] H. Wabnitz, M. Moller, A. Liebert, A. Walter, R. Erdmann, O. Raitza, C. Drenckhahn, J. P. Dreier, H. Obrig, J. Steinbrink and R. Macdonald, "A time-domain NIR brain imager applied in functional stimulation experiments," in *Photon Migration and Diffuse-Light Imaging II, June 12, 2005 - June 16, 2005*, Munich, Germany, 2005, pp. 1-9.

[62] H. Zhao, Y. Onodera, Y. Tanikawa, F. Gao, A. Sassaroli, K. Tanaka and Y. Yamada, "Light propagation in adult heads obtained from a time-resolved NIR optical imaging system," in *Technical Digest. CLEO/Pacific Rim 2001. 4th Pacific Rim Conference on Lasers and Electro-Optics, 15-19 July 2001*, Piscataway, NJ, USA, 2001, pp. 362-3.

[63] J. Kohlenberg and T. Chau, "Detecting controlled signals in the human brain by near infrared spectroscopy," in *28th Annual International Conference of the IEEE Engineering in Medicine and Biology Society, EMBS'06, August 30, 2006 - September 3, 2006*, New York, NY, United states, 2006, pp. 5480-5482.

[64] K. Izzetoglu, G. Yurtsever, A. Bozkurt and S. Bunce, "Functional brain monitoring via NIR based optical spectroscopy," in *Proceedings of the IEEE 29th Annual Northeast Bioengineering Conference, 22-23 March 2003*, Piscataway, NJ, USA, 2003, pp. 335-6.

[65] L. Qingming, "On human brain activity with functional NIR optical imager," in *Imaging of tissue structure and function. Selected research papers on imaging of tissue structure and function 1998-2000 (SPIE Vol.4427)*, Bellingham, WA, USA, SPIE, 2001, pp. 1-16.

[66] T. Vaithianathan, I. D. C. Tullis, N. Everdell, L. Terence, J. Meek and D. T. Delpy, "Functional imaging of the brain using a portable NIR instrument," in *Optical Tomography and Spectroscopy of Tissue V, 26-29 Jan. 2003*, USA, 2003, pp. 96-102.

[67] K. Alford, Y. Wickramasinghe and A. J. El Haj, "Quantitation of brain oxygenation and blood volume using a new intensity modulated NIR instrument," in *Proceedings of*

the 20th Annual International Conference of the IEEE Engineering in Medicine and Biology Society. Vol.20 Biomedical Engineering Towards the Year 2000 and Beyond, 29 Oct.-1 Nov. 1998, Piscataway, NJ, USA, 1998, pp. 1851-4.

[68] L. Hanli, D. A. Boas, A. G. Yodh and B. Chance, "Influence of clear cerebrospinal fluid on NIR brain imaging and cerebral oxygenation monitoring," in *OSA Trends in Optics and Photonics on Advances in Optical Imaging and Photon Migration. Vol.2. From the Topical Meeting, 18-20 March 1996*, Washington, DC, USA, 1996, pp. 372-5.

[69] Z. Liu, H. S. Lee, S. Lokos, J. Kim, D. F. Hanley and D. A. Wilson, "PRM/NIR sensor for brain hematoma detection and oxygenation monitoring," in *Biomedical Sensing, Imaging, and Tracking Technologies II, 11-13 Feb. 1997*, USA, 1997, pp. 281-90.

[70] L. Zheng, H. S. Lee, D. A. Wilson, D. F. Hanley, S. Lokos and J. Kim, "Experimental studies on brain hematoma detection and oxygenation monitoring using PRM/NIR sensors," in *Proceedings of Optical Tomography and Spectroscopy of Tissue: Theory, Instrumentation, Model and Human Studies II, Febrary 9, 1997 - Febrary 12, 1997*, San Jose, CA, United states, 1997, pp. 437-446.

[71] A. D. Edwards, C. Richardson, M. Cope, J. S. Wyatt, D. T. Delpy and E. O. R. Reynolds, "Cotside measurement of cerebral blood flow in ill newborn infants by near infrared spectroscopy," *The Lancet,* vol. 332, pp. 770-771, 1988.

[72] J. E. Brazy and F. J. Vander-Vliet, "Clinical application of near infrared spectroscopy to neonatal intensive care," in *Images of the Twenty-First Century - Proceedings of the 11th Annual International Conference of the IEEE Engineering in Medicine and Biology Society. Part 1, November 9, 1989 - November 12, 1989*, Seattle, WA, USA, 1989, pp. 337-338.

[73] T. Durduran, Z. Chao, E. M. Buckley, M. N. Kim, Y. Guoqiang, R. Choe, J. W. Gaynor, T. L. Spray, S. M. Durning, S. E. Mason, L. M. Montenegro, S. C. Nicolson, R. A. Zimmerman, M. E. Putt, W. Jiongjiong, J. H. Greenberg, J. A. Detre, A. G. Yodh and D. J. Licht, "Optical measurement of cerebral hemodynamics and oxygen metabolism in neonates with congenital heart defects," *Journal of Biomedical Optics,* vol. 15, p. 037004 (10 pp.), 2010.

[74] S. M. Liao, N. M. Gregg, B. R. White, B. W. Zeff, K. A. Bjerkaas, T. E. Inder and J. P. Culver, "Neonatal hemodynamic response to visual cortex activity: high-density

near-infrared spectroscopy study," *Journal of Biomedical Optics,* vol. 15, p. 026010 (9 pp.), 2010.

[75] F. S. Falla, C. Larini, G. A. C. Le Roux, F. H. Quina, L. F. L. Moro and C. A. O. Nascimento, "Characterization of crude petroleum by NIR," *Journal of Petroleum Science and Engineering,* vol. 51, pp. 127-137, 2006.

[76] R. M. Balabin, R. Z. Safieva and E. I. Lomakina, "Gasoline classification using near infrared (NIR) spectroscopy data: Comparison of multivariate techniques," *Analytica Chimica Acta,* vol. 671, pp. 27-35, 2010.

[77] R. M. Balabin, R. Z. Safieva and E. I. Lomakina, "Comparison of linear and nonlinear calibration models based on near infrared (NIR) spectroscopy data for gasoline properties prediction," *Chemometrics and Intelligent Laboratory Systems,* vol. 88, pp. 183-8, 2007.

[78] Y. Xiaogang and D. Liankui, "A least squares SVM algorithm for NIR gasoline octane number prediction," in *Fifth World Congress on Intelligent Control and Automation, 15-19 June 2004*, Piscataway, NJ, USA, 2004, pp. 3779-82.

[79] J. B. Cooper, C. M. Larkin, J. Schmitigal, R. E. Morris and M. F. Abdelkader, "Rapid analysis of jet fuel using a handheld near-infrared (NIR) analyzer," *Applied Spectroscopy,* vol. 65, pp. 187-192, 2011.

[80] I. Gonzalez-Martin, J. M. G.-C. M. Bustamante-Rangel and M. Milagros Delgado-Zamarreno, "Near infrared spectroscopy (NIRS) reflectance technology for determination of tocopherols in animal feeds," *Analytica Chimica Acta,* vol. 558, pp. 132-136, 2006.

[81] L. Wang, Q.-X. Meng, L.-P. Ren and J.-S. Yang, "Near infrared reflectance spectroscopy (NIRS) and its application in the determination for the quality of animal feed and products," *Guang Pu Xue Yu Guang Pu Fen Xi/Spectroscopy and Spectral Analysis,* vol. 30, pp. 1482-1487, 2010.

[82] I. Gonzalez-Martin, N. Alvarez-Garcia and J. M. Gonzalez-Cabrera, "Near-infrared spectroscopy (NIRS) with a fibre-optic probe for the prediction of the amino acid composition in animal feeds," *Talanta,* vol. 69, pp. 706-710, 2006.

[83] I. Gonzalez-Martin, N. Alvarez-Garcia, C. Gonzalez-Perez and V. Villaescusa-Garcia, "Determination of inorganic elements in animal feeds by NIRS technology and a fibre-optic probe," *Talanta,* vol. 69, pp. 711-715, 2006.

[84] M. S. Millan, J. Escofet and M. Rallo, "Unsupervised flaw segmentation in textile materials under visible and NIR illumination," in *Optics, Photonics, and Digital Technologies for Multimedia Applications, 12-15 April 2010*, USA, 2010, p. 77230Q (8 pp.).

[85] Y. Langeron, M. Doussot, D. J. Hewson and J. Duchene, "Classifying NIR spectra of textile products with kernel methods," *Engineering Applications of Artificial Intelligence,* vol. 20, pp. 415-27, 2007.

[86] G.-F. Wu and Y. He, "Identification of varieties of textile fibers by using vis/NIR infrared spectroscopy technique," *Guang Pu Xue Yu Guang Pu Fen Xi/Spectroscopy and Spectral Analysis,* vol. 30, pp. 331-335, 2010.

[87] Y. Zhou, H.-R. Xu and Y.-B. Ying, "NIR analysis of textile natural raw material," *Guang Pu Xue Yu Guang Pu Fen Xi/Spectroscopy and Spectral Analysis,* vol. 28, pp. 2804-2807, 2008.

[88] W. Bi, A. Tan, Y. Zhao and M. Gao, "Identification of oil spills by near-infrared spectroscopy (NIR) and support vector machine (SVM)," in *Proceedings of SPIE - The International Society for Optical Engineering - 2009 International Conference on Optical Instruments and Technology - Optoelectronic Measurement Technology and Systems, October 19, 2009 - October 22, 2009*, Shanghai, China, 2009.

[89] F. E. Barton II, "Theory and principles of near infrared spectroscopy," *Spectroscopy Europe,* vol. 14, pp. 12-18, 2002.

[90] D. C. Harris and M. D. Bertolucci, *Symmetry and spectroscopy : an introduction to vibrational and electronic spectroscopy*. New York: Oxford University Press, 1978.

[91] O. Howarth, *Theory of spectroscopy : an elementary introduction*. London: Nelson, 1973.

[92] (2011, 18/05/2011). *Morse potential*. Available:

http://www.answers.com/topic/morse-potential

[93] J. L. Duncan, "The determination of vibrational anharmonicity in molecules from spectroscopic observations," *Spectrochimica Acta Part A: Molecular Spectroscopy,* vol. 47, pp. 1-27, 1991.

[94] C. E. Miller, "Near-Infrared Spectroscopy of Synthetic and Industrial Samples," in *Handbook of Vibrational Spectroscopy*, John Wiley & Sons, Ltd, 2006.

[95] W. Groh, "Overtone absorption in macromolecules for polymer optical fibers," *Die Makromolekulare Chemie,* vol. 189, pp. 2861-2874, 1988.

[96] M. Ito, T. Suzuki, S. Yada, A. Kusai, H. Nakagami, E. Yonemochi and K. Terada, "Development of a method for the determination of caffeine anhydrate in various designed intact tables by near-infrared spectroscopy: A comparison between reflectance and transmittance technique," *Journal of Pharmaceutical and Biomedical Analysis,* vol. 47, pp. 819-827, 2008.

[97] H. Martens and T. Næs, *Multivariate calibration*. Chichester [England]; New York: Wiley, 1989.

[98] V. Centner, J. Verdu-Andres, B. Walczak, D. Jouan-Rimbaud, F. Despagne, L. Pasti, R. Poppi, D. L. Massart and O. E. De Noord, "Comparison of multivariate calibration techniques applied to experimental NIR data sets," *Applied Spectroscopy,* vol. 54, pp. 608-23, 2000.

[99] D. Berger, "Organic Laboratory Techniques, 3rd Edition (Fessenden, Ralph J.; Fessenden, Joan S.; Feist, Patty)," *Journal of Chemical Education,* vol. 78, p. 1336, 2001.

[100] J. Gottfries, H. Depui, M. Fransson, M. Jongeneelen, M. Josefson, F. W. Langkilde and D. T. Witte, "Vibrational spectrometry for the assessment of active substance in metoprolol tablets: a comparison between transmission and diffuse reflectance near-infrared spectrometry," *Journal of Pharmaceutical and Biomedical Analysis,* vol. 14, pp. 1495-1503, 1996.

[101] R. D. Driver and K. Didona, "On-line high-speed nir diffuse-reflectance imaging spectroscopy in food quality monitoring," in *Proceedings of SPIE - The International Society for Optical Engineering - Sensing for Agriculture and Food Quality and Safety, April 14, 2009 - April 15, 2009*, Orlando, FL, United states, 2009.

[102] R. Lu, D. E. Guyer and R. M. Beaudry, "Determination of firmness and sugar content of apples using near-infrared diffuse reflectance," *Journal of Texture Studies,* vol. 31, pp. 615-630, 2000.

[103] A. Springsteen, "Standards for the measurement of diffuse reflectance - an overview of available materials and measurement laboratories," *Analytica Chimica Acta,* vol. 380, pp. 379-390, 1999.

[104] M. Garcia-Alvarez, J. F. Huidobro, M. Hermida and J. L. Rodriguez-Otero, "Major Components of Honey Analysis by Near-Infrared Transflectance Spectroscopy," *Journal of Agricultural and Food Chemistry,* vol. 48, pp. 5154-5158, 2000.

[105] L. León, J. D. Kelly and G. Downey, "Detection of Apple Juice Adulteration Using Near-Infrared Transflectance Spectroscopy," *Appl. Spectrosc.,* vol. 59, pp. 593-599, 2005.

[106] (2011, 18/06/2011). *Ocean Optics Inc.: QF600-8-VIS/NIR Fiber Fluorescence Probe*. Available: http://www.oceanoptics.com/products/qf600-8.asp

[107] S. Kawano, H. Watanabe and M. Iwamoto, "Determination of sugar content in intact peaches by near infrared spectroscopy with fibre optics in interactance mode," *Journal of the Japanese Society for Horticultural Science* vol. 61, pp. 445–451, 1992.

Chapter 2
NIR transmission through clothing barriers

2.1 Introduction

One of the main aims of the research was to show that NIR signals could be used to detect and quantify chemicals that are hidden behind clothing layers. An important variable that will have a large effect on the resultant measurement is the transmission characteristics of NIR signals through clothing [1]. It was thus thought important that this was studied in some detail. Of interest is the way in which both the fibre material and the weave pattern affect the transmitted NIR signal, in terms of the total intensity transmitted, the spatial variations in the transmitted beam (i.e. the resultant diffraction pattern) [2] and the effect on transmitted spectra [3].

A selection of clothing materials were chosen for study, along with some thin layers of other materials that give an insight into the mechanisms involved. Paper was studied initially, as this was available in known densities and thicknesses as a random mesh. Also studied were metallic grids with a known regular pattern. Both gave an additional insight into the transmission characteristics of NIR signals though thin, scattering layers.

2.2 Initial investigations in non-clothing material

2.2.1 Introduction

Preliminary experiments were carried out to investigate the way in which scattering took place as a collimated beam of NIR radiation passed through different thicknesses of different types of material. Clothing is a complicated case; hence, it was decided to study a range of different scattering media, to try and establish some basic properties, before the more difficult task of understanding transmission through clothing was attempted. Paper provided a relatively thin and uniform scattering medium [4] compared to fabric samples [5], and was looked at firstly to gain insight into transmission properties. The initial material chosen was 80gsm paper, "gsm" being an industry unit for the density of paper in grams per square meter. Later measurements looked at thicker polystyrene samples, as described more fully below. Finally, metallic

grids with known pore sizes were also investigated as an example of material with a uniform spatial porosity.

2.2.2 Apparatus

An example of the surface of the paper sample used is shown in the photograph of Figure 2.1, taken with an optical microscope. The sample was placed in the path of an incident 5mW NIR laser beam at 850nm wavelength with 5mm cross-sectional aperture generated with an NIR laser diode. The through-transmitted energy was recorded using a 2mm aperture NIR photodiode housed in a metal casing mounted on a 2D scan stage.
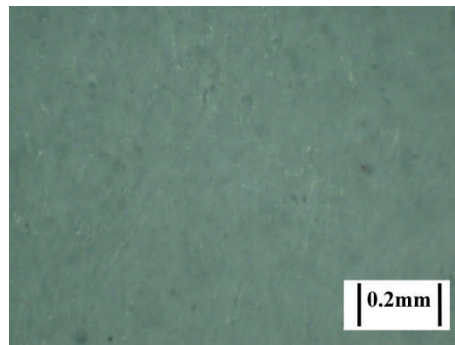
Figure 2.1 – Sheet of 80gsm paper imaged under a light microscope.

Two sets of measurements were recorded. In the first case, the scan geometry was set to measure NIR intensity values in the plane perpendicular to the direction of propagation of the NIR beam, while in the second case, the measurement plane was axially aligned with the direction of propagation of the beam. Schematic diagrams and photographs of the two arrangements are shown in Figures 2.2 and 2.3 respectively. As seen, the laser diode and the paper sample/s were held stationary while two-dimensional scans were performed by moving the detector with the 2D scanning stage shown. Signal enhancement was carried out by modulating the transmitted beam with a 200 Hz carrier frequency, the latter used as reference to perform lock-in amplification of the received signal [6]. As shown below, this allowed detection of signals buried in noise many orders of magnitude higher than the recorded signal level, enabling detection of signals across up to forty layers of paper.

In the first case, scans were obtained in the *x-y* plane as shown in Figure 2.2(b), which was parallel to the paper sample and perpendicular to the NIR beam axis i.e. *z*-axis. This allowed radial spreading of the beam to be observed, following transmission through an

incremental number of paper sheets. The sheets were held in a frame aligned horizontally on top of the laser diode that was transmitting vertically upwards. Sheets could be added one at a time, starting with one sheet of paper and going up to forty sheets. The longitudinal displacement of the detector from the sample was kept constant at 6.8 cm ± 0.1 cm. The total scan area covered in each case was 80 mm x 80 mm, with a step size of 1 mm. As shown in Figure 2.2(a), the scan was controlled by a PC running LabView^{TM}, with the output from the lock-in being recorded on a digital oscilloscope. The motors were switched off after each scan to a new position before data was collected, to reduce noise from the motors.
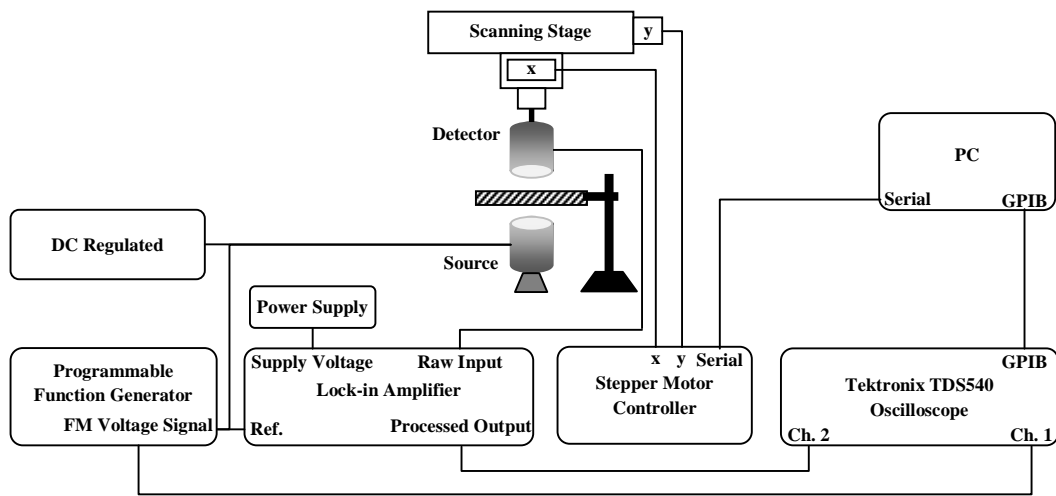
(a)
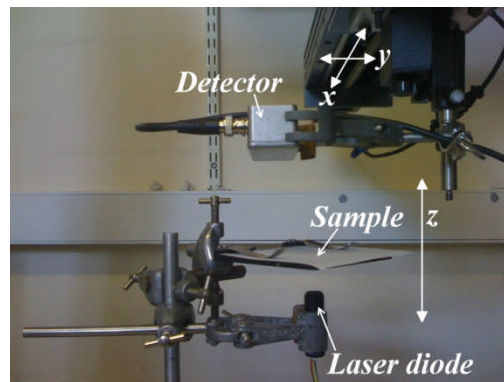
(b)

Figure 2.2 – Arrangement used to detect beam cross-section in x-y plane parallel to the paper samples and perpendicular to NIR beam axis (z-axis). (a) Schematic diagram of the apparatus, and (b) photograph of the sample and optical source (laser diode)/ detector.

In a second set of experiments, the detector was scanned in the *x-z* plane, so as to capture the radiation pattern along the direction of propagation of the beam (the *z* direction) as it scattered after traversing the sample. The total area covered was 60 mm

(*x*-axis) x 40 mm (*z*-axis) with a 0.25 mm step size. The arrangement is shown in Figure 2.3.

2.2.3 Experiments with paper

Cross-sectional intensity patterns recorded across free space and with 1-3 sheets of paper using the arrangement in Figure 2.2 are shown in Figure 2.4(a)-(d) respectively. As seen, compared with (a) unobstructed beam, there is considerable broadening of the beam when sheets of paper are placed between the source and the detector. Further, in all the patterns recorded with paper sheets, the highest intensity readings are concentrated in the centre (coincident with the axis of the incident beam), with rapidly decreasing intensities radially outwards from the centre. Finally, while the overall intensity is seen to reduce with increasing number of paper sheets, the intensity distribution pattern remains essentially the same.
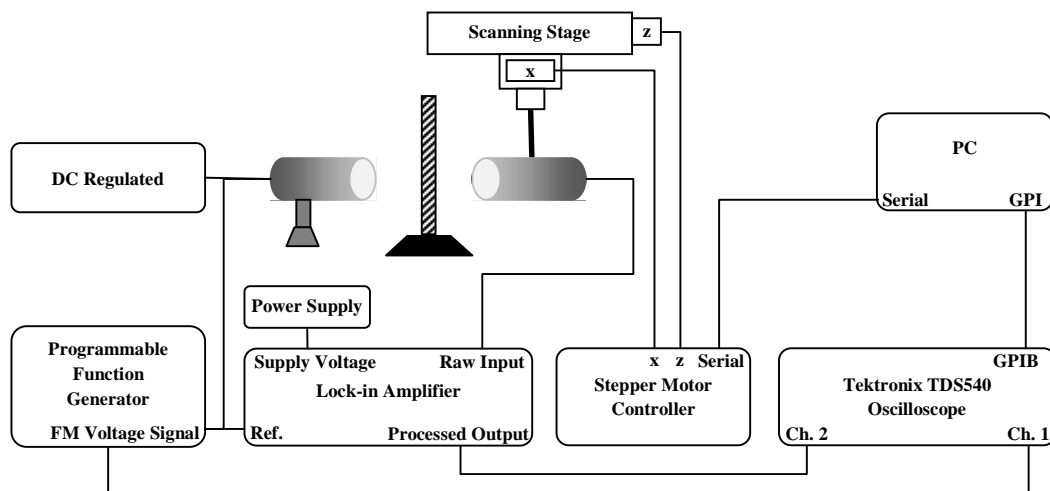
(a)
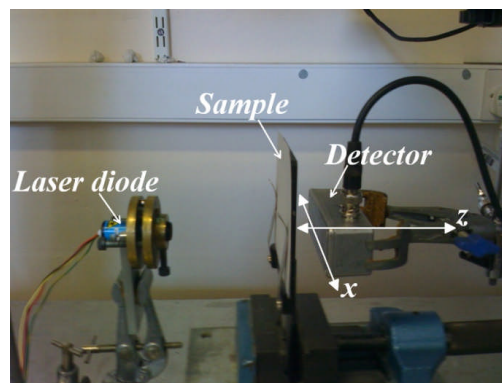
(b)

Figure 2.3 – Arrangement used to detect beam cross-section in x-z plane parallel to NIR beam axis and normal to the paper samples. (a) Schematic diagram of the apparatus, and (b) photograph of the sample and optical source (laser diode)/ detector.

In order to deduce the effect of increasing number of scatterers on the cross-sectional magnitude of resulting scatter patterns, full width at half maximum (FWHM) values were measured [7] to quantify the magnitude of the scatter. These measurements were made for line scans across 1-40 sheets of paper recorded along the *x*-axis at a distance of *z* = 1 mm from the top paper surface (ref. Figure 2.2(b)). Normalized intensity curves for the forty scans are shown in Figure 2.5(a), with the corresponding FWHM values plotted in Figure 2.5(b). As seen, the FWHM values clearly show an approximately linear upward trend save for a few anomalous readings attributable to experimental errors, with an almost 40% increase in magnitude as the number of scatterers is increased from 1 to 40. This shows that the cross-section of the scatter profile increases almost linearly with the thickness of the scattering medium, an observation which is borne out by measurements with different scattering media detailed in the following sections.

(a) *(b)* *(c)* *(d)*
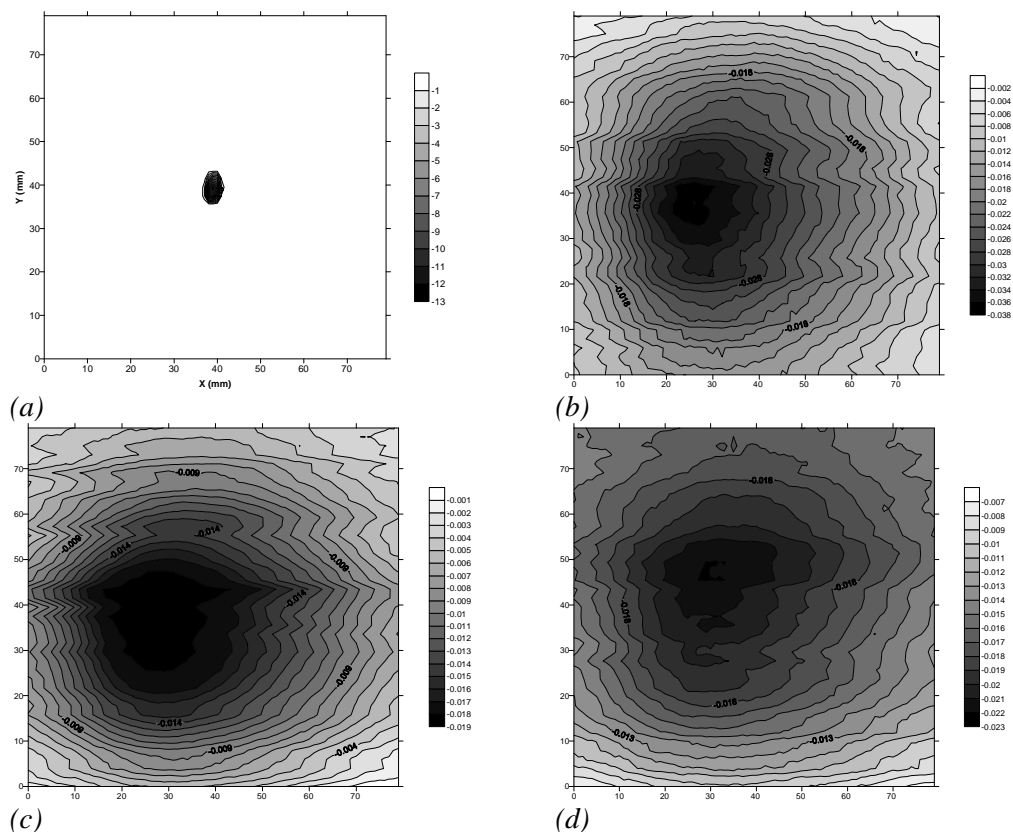
Figure 2.4 – Cross-sectional intensity scans recorded in the x-y plane across
(a) free space, and (b)-(d) 1-3 layers of paper respectively.

Figure 2.6 shows intensity patterns recorded across free space and 1-3 layers of paper in the *x-z* plane that was collinear with the transmission axis, using the apparatus

arrangement shown in Figure 2.3. As seen in (a) free-space beam profile, there is no detectable divergence in the beam up to the limit of the scanned distance (approximately 35 cm from the source). However, as noted before, the intensity patterns show marked broadening when the beam is obstructed by paper sheets. Additionally, while intensity readings decrease as the number of layers is increased, the overall pattern of intensity distribution remains similar in (b)-(d).

(a)   *(b)*
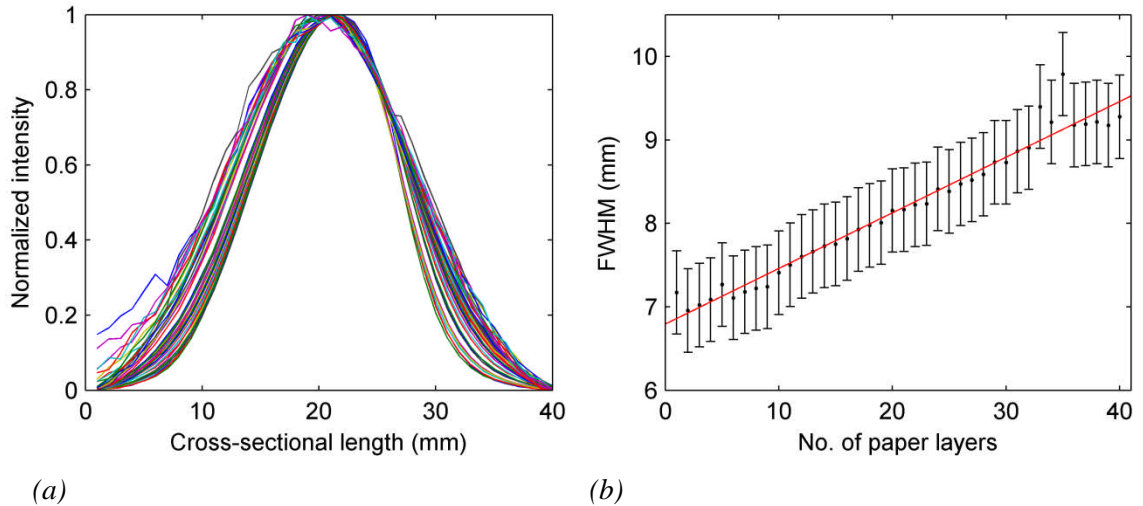
Figure 2.5 – Results of cross-sectional line scans across 1-40 sheets of paper;
(a) Normalized intensity curves; (b) FWHM values for the curves in (a).

(a)   *(b)*

(c)   *(d)*
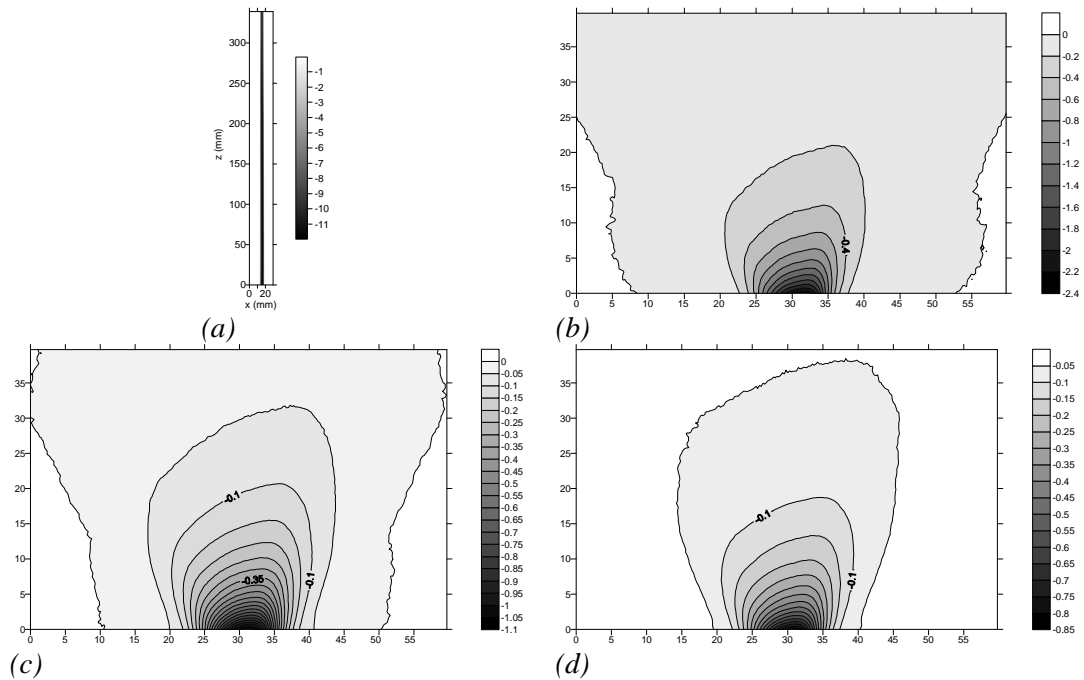
Figure 2.6 – Intensity scans in a plane collinear with the direction of propagation of the beam,
recorded across (a) free space, and (b)-(d) 1-3 layers of paper respectively.

The decay in optical intensity as the transmitted signal propagated away from the far side of the paper sample was also studied. Intensity readings were collected along the z direction, *i.e.* direction of travel of the beam, for increasing number of paper layers. The readings recorded with two sheets of paper are plotted (labelled Experimental Data) in Figure 2.7(a). As seen, the decay appears to be approximately exponential. If this were the case, a simple relationship [8] that described the drop in axial intensity with distance z could be written as:

$$I = I_0 e^{-\alpha_p z} \tag{2.1}$$

Here, the instantaneous intensity I is linked to initial intensity I_0 via α_P, the propagation attenuation coefficient, and z, the location of the point along the z-axis. The value of α_P is thus calculated for each point along the z-axis using:

$$\alpha_P = -\frac{1}{z} \ln \frac{I}{I_0} \tag{2.2}$$

All calculated α_P values, plotted in Figure 2.7(a), are averaged to obtain α_{P_Avg} as shown. Using this average value of α_P, the exponential decay curve based on (2.1) is obtained and plotted as shown. As seen, this curve closely follows the trajectory of the experimental data, thus validating the original approximation to such exponential function.

The above procedure was used to obtain values of α_{P_Avg} across 1-5 layers of paper. These are plotted against respective number of layers in Figure 2.7(b). The plot exhibits an approximately linear characteristic, with α_{P_Avg} decreasing as the number of paper sheets is increased. This indicates that for a single sheet of paper, intensity values start from a relatively high initial level and decrease rapidly along the z-axis with a correspondingly high α_{P_Avg}. As the number of layers i.e. thickness of the scattering medium is increased, however, the initial intensity readings decrease substantially, and the measured intensity then decays more gradually, as characterised by decreasing values of α_{P_Avg}.

In summary, these studies have indicated that the likely effect of scattering within media such as paper is that beam cross-sections increase on transmission through more layers, with the peak intensity decreasing. Once these beams propagate away from the sample

Chapter 2: NIR transmission through clothing barriers

on the far side, the decay in intensity is exponential, with a characteristic value of α_{P_Avg}, the value of which decreases with the number of paper layers.

(a)   *(b)*
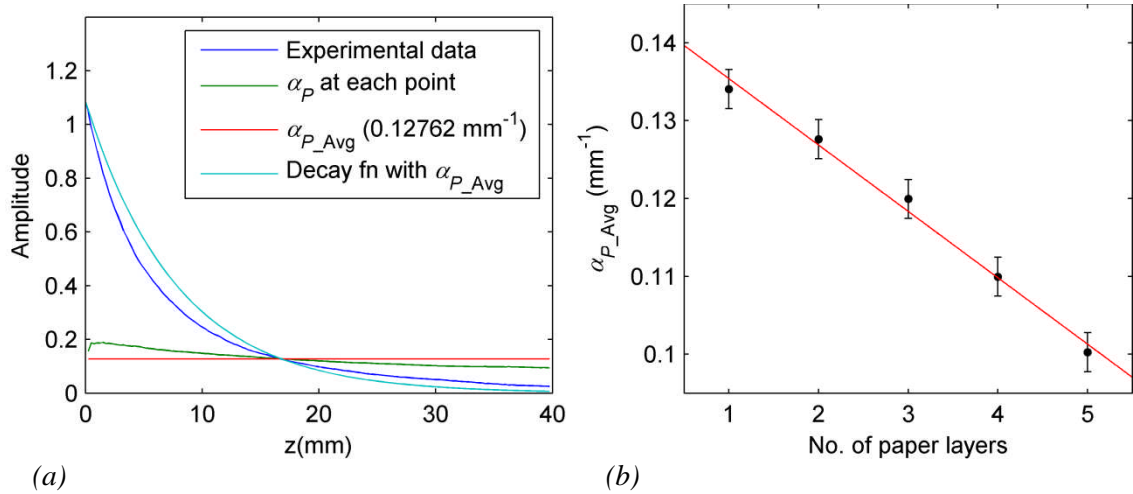
Figure 2.7 – Signal decay across paper samples along the direction of travel of the beam (z-axis), recorded using the arrangement in Figure 2.3. (a) Characteristic plots for 2 sheets of paper; (b) α_{P_Avg} for 1-5 layers of paper.

2.2.4 Scattering through expanded polystyrene foam

Expanded polystyrene foam is an example of a material that is much thicker than paper, but which also would cause a high degree of scattering of NIR energy in through-transmission [9]. The relationship between cross-sectional width of the scattered beam and the thickness of the scattering medium could be studied for varying thickness of the same polystyrene sample. The intrinsic structure of the sample, as seen under an optical microscope (Figure 2.8(a)), appeared less uniform than that of paper. However in this case, a changing thickness could be machined into the sample as shown in Figure 2.8(b), thus avoiding the presence of air gaps between multiple layers (as in the case of paper sheets). Line scans were performed for various thicknesses of polystyrene between 5 mm and 45 mm, in 5 mm increments. The detector was held close to the flat surface to minimise any air gaps, and moved horizontally to make the line scans.

Figure 2.8(c) shows the normalized scan data recorded with the above arrangement. As can be seen, the normalised width of the NIR beam on transmission through the sample increased with sample thickness, due to scattering. From this data, the FWHM of the radial intensity profile was estimated for each step size, and the results plotted in Figure 2.8(d). This further confirms the approximately linear dependence of the cross-sectional

scatter diameter of the through-transmitted NIR beam on the thickness of the sample, assuming all other parameters remain constant.
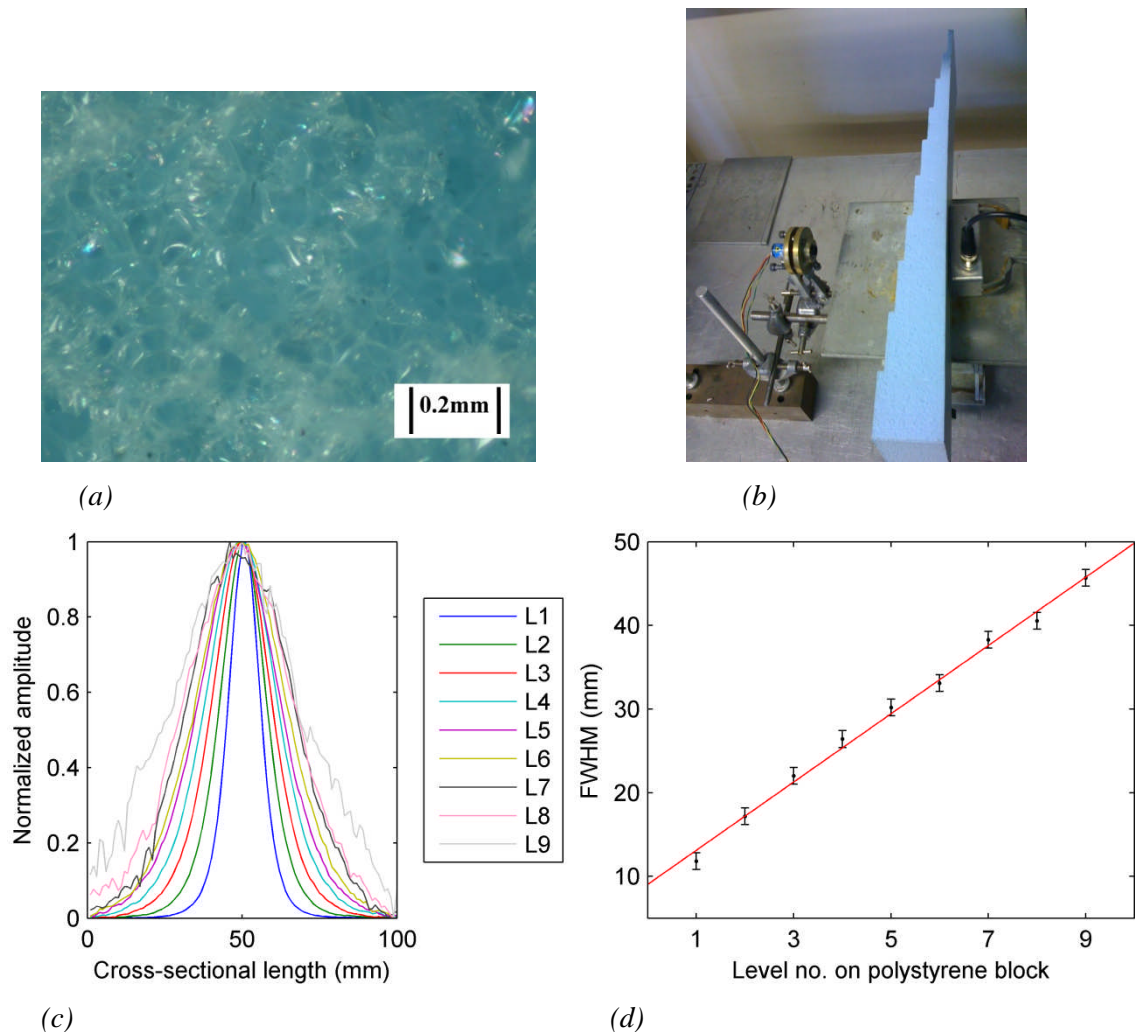
Figure 2.8 – Measurements with polystyrene sample; (a) Sample imaged with light microscope; (b) Equipment layout; (c) Normalized line scan data (Thickness of level Ln = 5 × n mm); (d) FWHM values measured for the line scan curves shown in (c).

2.2.5 Measurements with metallic TEM grids

In order to study the diffractive effect of pore size on the spatial distribution of through-transmitted energy, samples of copper grids designed for use in transmission electron microscope (TEM) were used [10]. These all had the same uniform diameter of 3.05 mm and thickness of 9 µm, while the pore sizes in the eleven different configurations used for the tests ranged from 6 µm to 100 µm. The general layout of the grids is shown in Figure 2.9, which shows scanning electron microscope (SEM) images of one of the grids, to illustrate its close resemblance to the more random porous structure found in fabrics.

The equipment layout shown in Figure 2.10 was used to record three-dimensional cross-sectional images of NIR energy transmitted through each of the grids in turn. The grid samples were held in an SEM stub designed for TEM grids, which in turn was mounted underneath the 850 nm NIR laser diode so that the beam axis was normal to the surface of the grid. This source/ grid assembly was held in a scan stage and scanned in two dimensions over a photodiode detector held stationary underneath on a variable-height stand. Intensity images were recorded with this arrangement in 3D volume with the distance between the source/ grid assembly and the detector varied (by adjusting the height of the stand) from 15 mm to 55 mm in steps of 10 mm. Five cross-sectional scans were thus recorded with each grid sample, with a vernier height gauge used to measure and set the distance between the grid sample and detector for each scan.
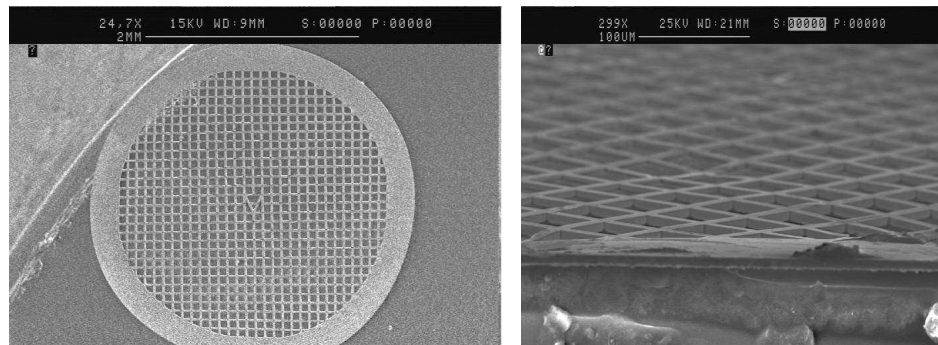
*Figure 2.9 – SEM images of copper grids used to study
the interaction of pores with NIR energy.*
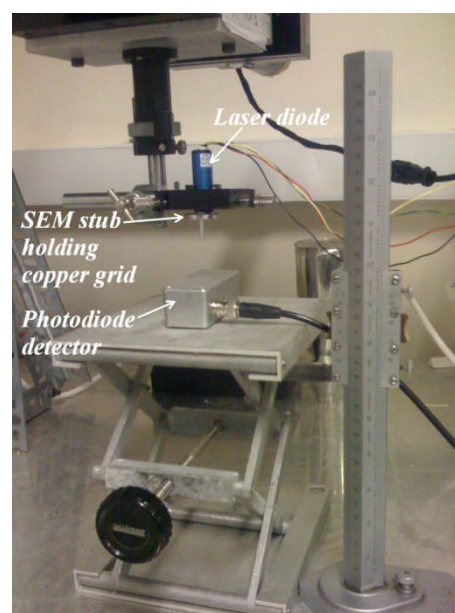
*Figure 2.10 – Scanning arrangement used to make NIR intensity
measurements in 3D across copper grids.*

The scans obtained with two of the grid samples with pore sizes 50 µm and 6 µm illustrate the two limiting cases, and are shown in Figure 2.11(a) and (b) respectively. In the first case, the 50 µm pores are approximately 60 times wider than the 850 nm wavelength of the NIR beam, and thus do not cause any appreciable diffraction effects, as evidenced by the nearly uniform cross-sectional intensity contours recorded over the measured volume as seen in Figure 2.11(a). On the other hand, the 6 µm pores are seen to introduce relatively wide angular spread in the through-transmitted beam as shown in Figure 2.11(b), with diffraction effects and side lobes marked out in the contour plots.

(a)   (b)
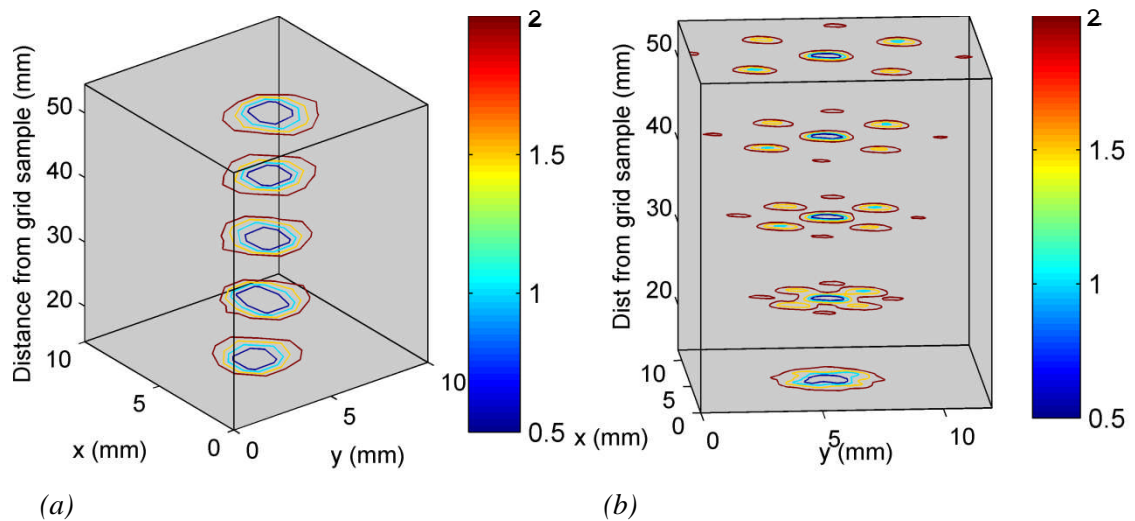
Figure 2.11 – Cross-sectional contour plots of NIR intensity distribution transmitted through copper grids with regular pore sizes of (a) 50 µm and (b) 6 µm.

2.2.6 Discussion

By studying the through-transmission properties of three different materials, it has been demonstrated that scattering can lead to a variety of effects at a wavelength of 850 nm. In effect, the transmission intensity falls, and the beam width widens, as either the thickness of the sample is increased or multiple layers of the same sample are introduced. This assumes a random scattering effect (as seen in paper and the polystyrene foam). The beam cross-section at FWHM appears to depend linearly on the thickness of the sample in such cases. In addition to this, the size of any pores in a structure will have an effect, by introducing a diffraction effect. This will be in addition to the above, and was demonstrated by the transmission properties seen in the copper TEM grids.

2.3 NIR scattering in fabric samples

2.3.1 Selection of clothing materials

One of the primary concerns in the context of developing a practical personal screening/ imaging system is the way in which incident radiation interacts with the clothing materials worn by the subjects in a personal screening test [11]. The weaves found in typical clothing layers are likely to have through-transmission characteristics in the NIR wavelength range that contain aspects of both of the main features mentioned above in Section 2.2, in that they would be likely to introduce a degree of scattering (due to fibres) which would cause beam spreading, and the various degrees of porosity which would also affect overall transmission levels.

In order to gain an appreciation of the different phenomena that dictate the behaviour of various clothing materials, a range of different fabric samples was used to carry out comparative tests. Photographs of some of these samples taken under an optical microscope are shown in Figure 2.12(a) and (b), where the latter includes two cotton samples in both dry and wet states. Note that wetting seems to have caused the fibres to swell, decreasing the porosity of the samples.

2.3.2 Webcam measurements to illustrate scattering

In order to investigate the effects of traversing a layer of clothing on the cross-sectional shape of the beam, a modified arrangement shown in Figure 2.13 was used to collect data more effectively from multiple samples. Instead of scanning a source-detector pair as in the preliminary work with paper, the NIR laser diode, seen on the left, was used to transmit an 850nm unmodulated beam through the clothing sample (denim in the photograph), and the pattern emerging on the other side was imaged using a portable webcam [12] (Trust 150 Spacecam model) seen on the right. An NIR filter was mounted inside the webcam to restrict sensitivity to the NIR range. A red LED was mounted in front of the sample to provide a constant reference level. This was done in view of the fact that the webcam by default auto-adjusted and normalized the brightness of all captured intensity images. Using the constant reference level, the captured intensities were therefore re-adjusted to make the reference intensity constant in all the images, thus allowing comparison between the results obtained with different clothing materials.

(a)

(b)
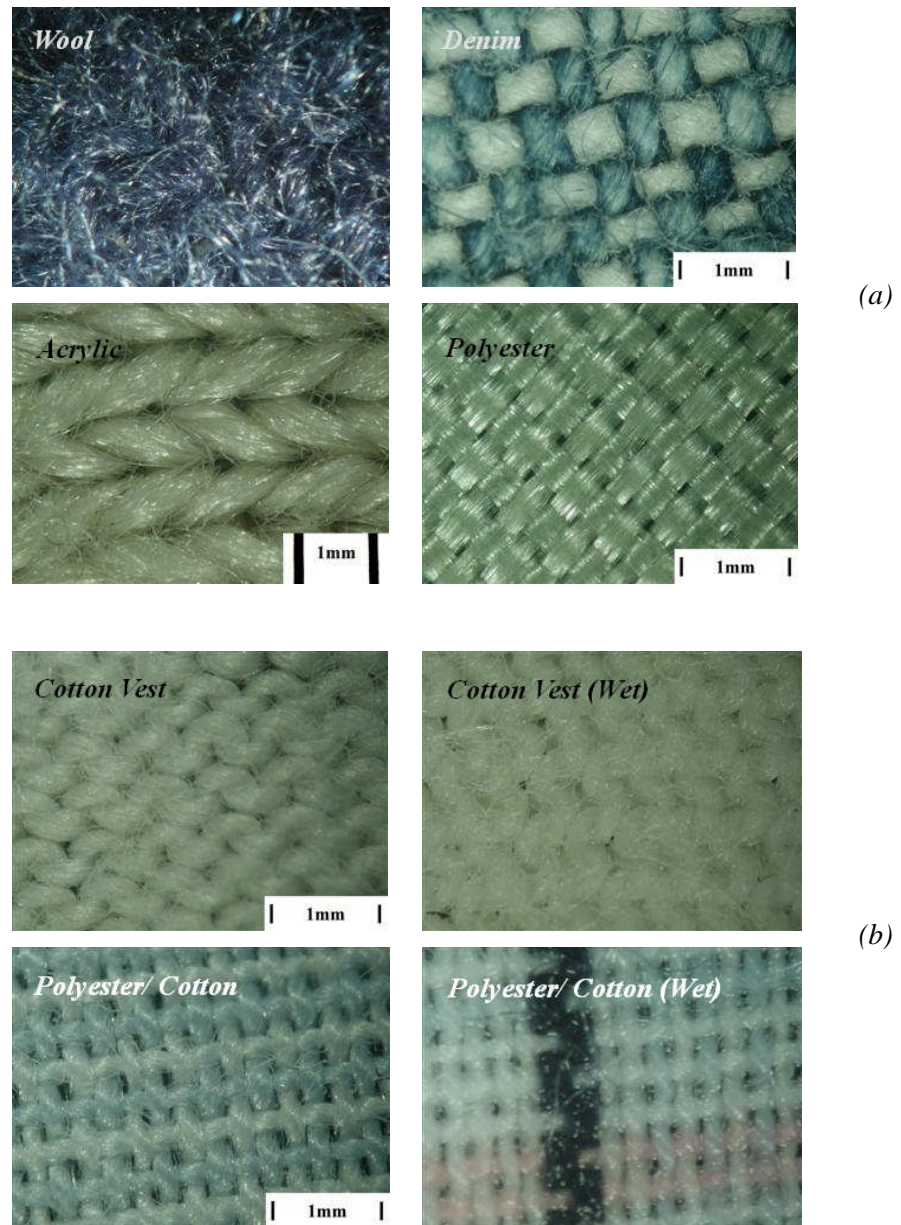
Figure 2.12 – Optical microscope photographs of (a) four of the fabric samples investigated, and (b) some fabrics both in the dry state and when moistened with water.
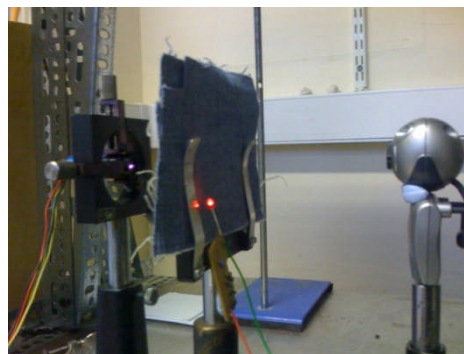
Figure 2.13 – Studying the characteristics of through-transmitted NIR beam using webcam.

The intensity-corrected webcam images obtained for four fabric samples are shown in Figure 2.14. All images show a fairly significant broadening of the beam, which is attributable to the effects of scattering. However, the intensity recorded in each case is seen to be different, which illustrates the different transmission characteristics of these samples. It is evident that scattering is an important factor in these materials, and is the factor likely to dominate NIR transmission levels.
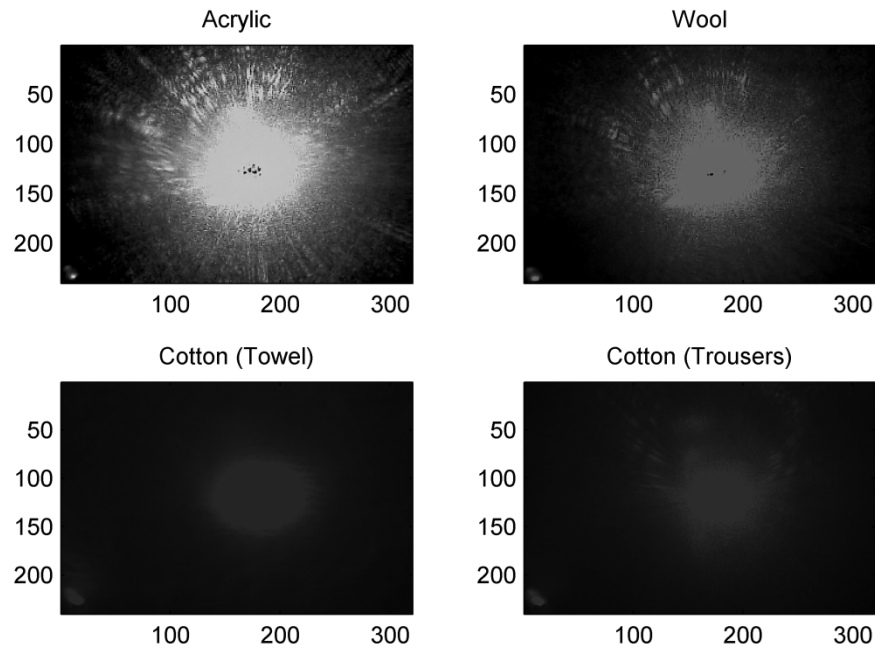
Figure 2.14 – Intensity-corrected webcam images of NIR beam transmitted through single fabric layers.

2.3.3 Intensity measurements across multiple fabric layers

In order to gain an understanding of the properties that give rise to these different intensity levels and the over-arching effects of scattering, further tests were carried out as follows.

All the samples were exposed in turn to an NIR laser beam at 850 nm using the same arrangement as shown in Figure 2.2(b), and point measurements were made to record intensity levels with the photodiode detector axially aligned with the laser source. Measurements were taken across increasing number of layers of the fabric samples until no further signal could be detected. While the results, shown in Figure 2.15, illustrate the general overall decrease in signal levels with increasing number of layers, the rate of decline is seen to vary greatly between samples such as denim that cause complete

attenuation of through-transmitted energy within 2-3 layers, and samples like cotton/ polyester that provide measurable signal levels even through 10-12 layers.
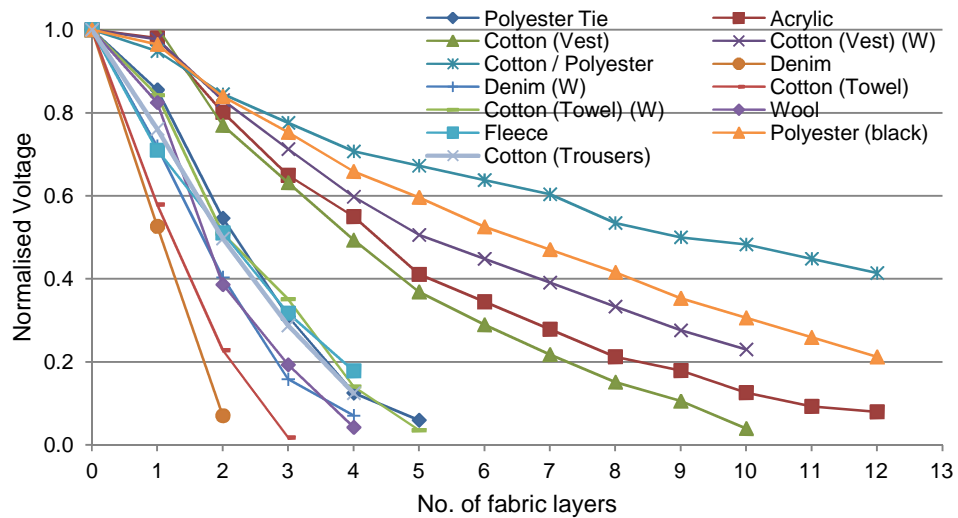
Figure 2.15 – Point measurements showing drop in NIR intensity across multiple fabric layers. (W) signifies wet samples.

Further tests were undertaken to test whether the colour of a particular fabric affected through-transmitted energy level, albeit with the understanding that an affirmative finding would be counter-intuitive as the 850 nm wavelength used was well-separated from the visible spectrum [13]. For this purpose, five samples of a white cotton fabric were dyed red, green, blue, yellow and black, and a further two samples of a polyester fabric were obtained in white and black colours. The normalized through-transmitted signal levels recorded across these samples are shown in Figure 2.16.While these results show some variation between the different colours, this is deemed insignificant compared with the differences amongst the different fabric types, and can be attributed to the different chemical compositions of the relevant dyes [14] affecting the through-transmitted signal levels differently.

The data plotted in Figures 2.15 and 2.16 includes the readings across wet samples (marked as 'W'). As seen, wet samples provided higher through-transmission levels than the same samples in dry state. This effect was further investigated by testing a range of samples containing varying levels of moisture. Each sample was saturated with water and allowed to dry through evaporation. Its weight, measured at regular intervals with a microbalance, was used as an indicator of moisture content, and recorded against the through-transmitted signal level. The results are shown in Figure 2.17.
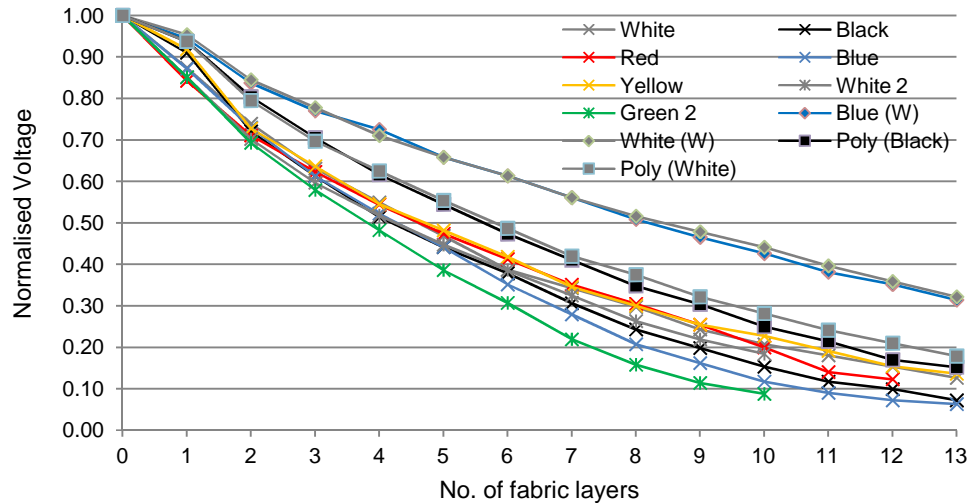
Figure 2.16 – Signal variation across various dyed fabric samples of cotton (six colours) and polyester (black and white only). (W) signifies wet samples.
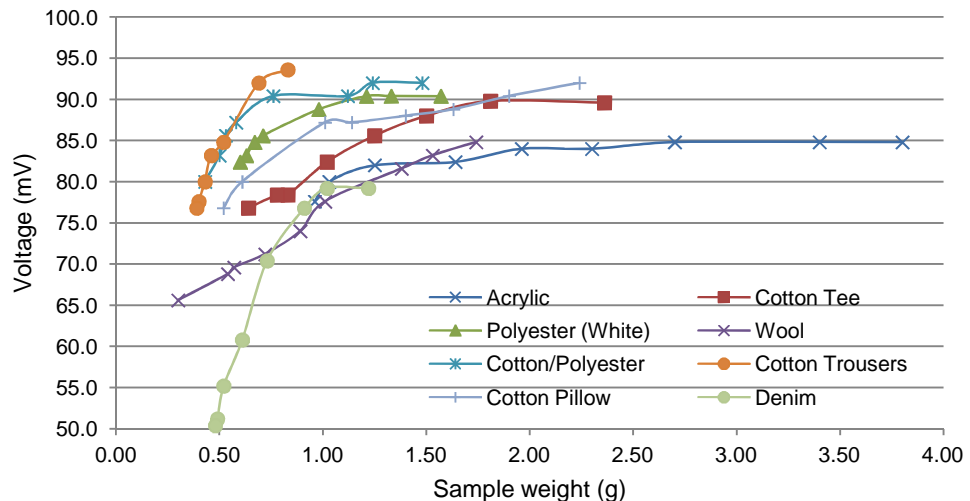
Figure 2.17 – Effect of moisture on through-transmitted signal levels.

It is seen that in all cases, increasing moisture content results in an increase in through-transmitted signal. This higher transmission in the presence of water is thought to be the result of water acting as an impedance matching layer [15] to reduce optical impedance mismatch between air and the sample, as the refractive index of water is closer to that of air [16] compared with the fabrics [17]. This reduces the amount of scattering, resulting in more signal energy emerging on the other side of the sample. Additionally, as the moisture content increases, the water progressively fills in the pores in the fabric, which would render the structure more optically homogeneous with associated higher through-transmitted signal levels.

In order to clarify the results obtained with wool, the structure of the sample was examined in optical microscope, and was seen to be highly chaotic as shown in the photograph in Figure 2.18(a). This can thus be considered a possible limiting case for scattering within fabric samples, which would be compounded further by air gaps between multiple layers of the fabric. Using scan geometry and equipment setup shown in Figure 2.18(b) (similar in concept to that shown earlier in Figure 2.3(b)), line scans were obtained across incremental layers by folding a highly-coloured woollen scarf, with discernible signal intensities recorded across a maximum of 6 layers. Line scans obtained with the scarf are shown in Figure 2.18(c), with corresponding FWHM values plotted against the respective number of layers in Figure 2.18(d).

(a)   *(b)*

(c)   *(d)*
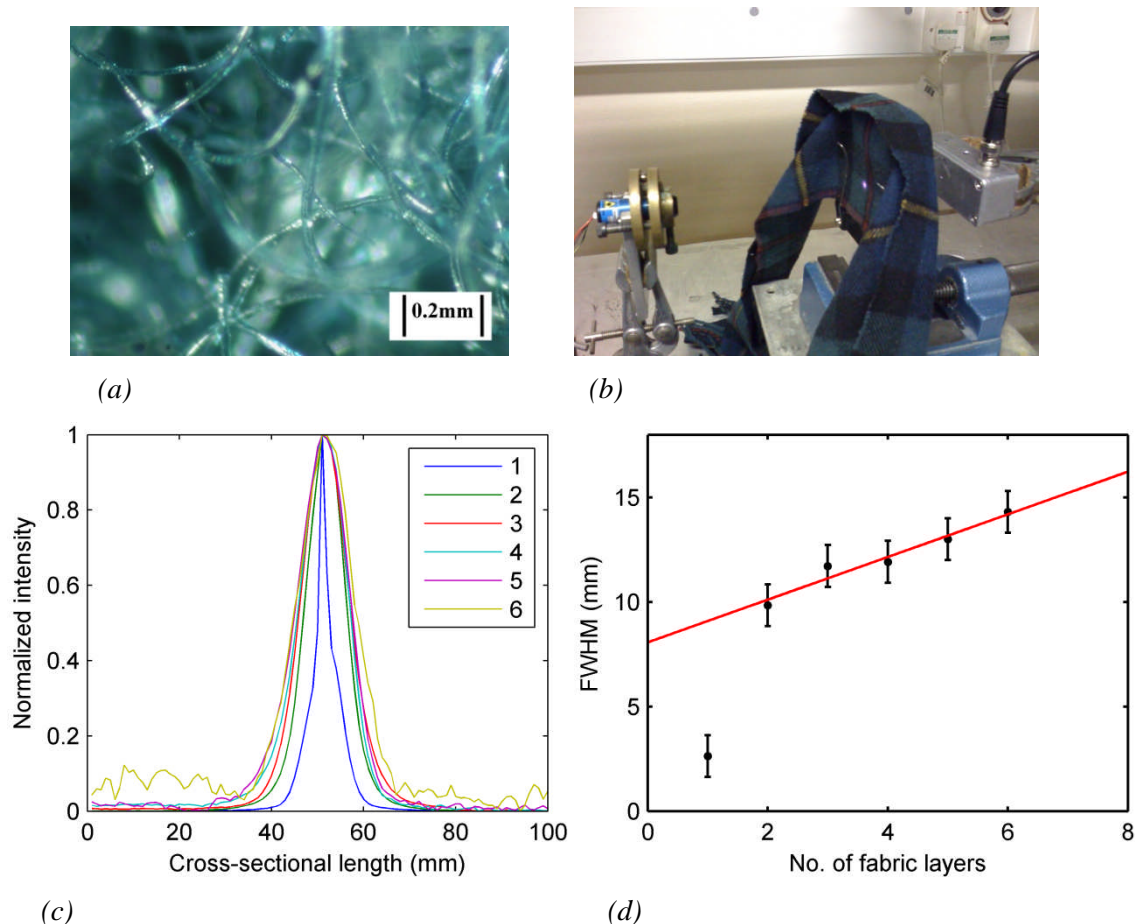
Figure 2.18 – Measurements with woollen scarf. (a) Sample imaged with light microscope; (b) Equipment arrangement; (c) Normalized line scan data for 1-6 layers; (d) FWHM values measured for the line scan curves shown in (c) (1st value excluded from linear fit)

As expected, the values exhibit an upward trend with increasing number of layers or thickness of the medium. However, the linearity of the trend is less well-defined due to an exceptionally low reading across one layer. This is deemed to be a consequence of

the added complication introduced in measurements taken with multiple layers, due to the increased scattering through air gaps between adjacent layers.

2.3.4 The effect of porosity

The studies above have shown that the transmission characteristics are a complicated function of the weave pattern and the material used for the fibres. To try and establish a clearer link with porosity, a set of experiments was performed on fabric samples to measure their porosity [18], and link this to overall NIR transmission.

Porosity was measured using the equipment shown in Figure 2.19. This involved exposing the fabric samples held between two plates in a mass flow meter to a stream of air at a pre-determined flow rate F, and measuring the resulting differential pressure P across the sample with a Sensirion SDP1000-R low-range differential pressure transducer attached to the mass flow meter. The high pressure input was provided from a compressed air source via a control unit used to adjust the air flow rate as desired, while the low pressure output was connected to a vent with a long stretch of pipe. Pressure P was deemed to be inversely proportional to the porosity of the sample at a given flow rate F.

Figure 2.19 – Mass flow meter setup for porosity estimation

The voltage readings provided by the differential pressure transducer were converted to pressure P using the following relationship as per manufacturer's guidelines [19]:

$$P = 35.55556 \times (V - 0.25)^2 \qquad (2.3)$$

where V denotes measured output voltage in volts, and P is the pressure in pascals. The measure of porosity (Por) was then taken as the ratio of flow rate F, recorded in ml/min, to pressure P:

$$Por = F/P \qquad (2.4)$$

A range of readings was taken with each fabric sample at different flow rates, and averaged to find the final estimate of porosity. The results for all fabric samples are shown in Figure 2.20.
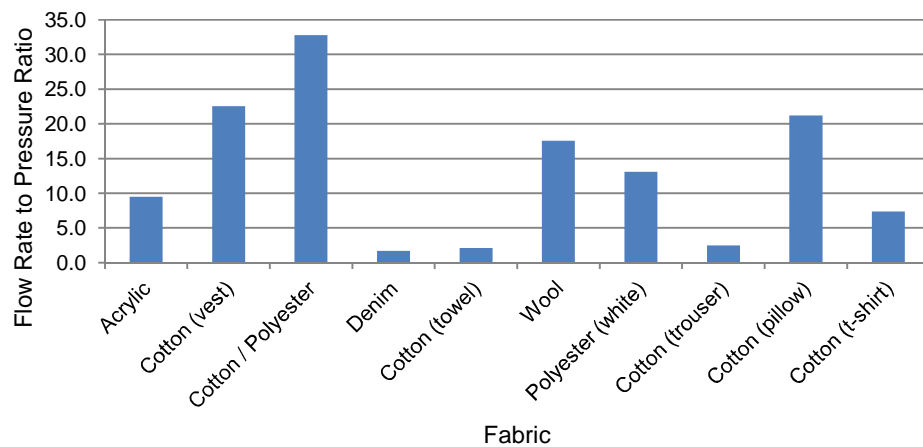
Figure 2.20 – Variation in porosity with different fabric samples

When these measurements are correlated with the through-transmission results shown in Figure 2.15, it is seen that in general, higher porosity values provide higher through-transmitted signals and vice versa. For example, the three samples with the lowest porosity estimates, *i.e.* denim, cotton (towel) and cotton (trousers), are seen to have the lowest transmission values, while the cotton/ polyester sample with the highest porosity estimate gives highest transmission readings as well. An interesting exception is wool, which provides the third lowest transmission values (lower than the cotton (trousers) sample), although its porosity estimate is relatively high. This behaviour is deemed to be the result of the unusually chaotic surface texture of wool as seen in Figures 2.12(a) and 2.18(a), which scatters more NIR energy than other materials with similar porosity values.

As the values shown in Figure 2.15 were recorded with a point detector as explained above, only the fraction falling within the 2mm aperture of the detector was recorded.

As a result, a sample scattering more energy might record a lower value than one scattering less, although the total amount of through-transmitted signal in the former case might be higher due to higher porosity. The following experimental arrangement was thus adopted to provide a possible work-around for this issue. In order to collect all the light transmitted through a fabric sample rather than only the fraction within the aperture of the detector, an integrating sphere was used to collect the through-transmitted signal [20]. Intensity readings across one and two layers of different fabric samples were recorded using Ocean Optics FOIS-1 integrating sphere connected via an optical fibre cable to an HR4000 Ocean Optics NIR Spectrometer. The arrangement is shown in Figure 2.21.
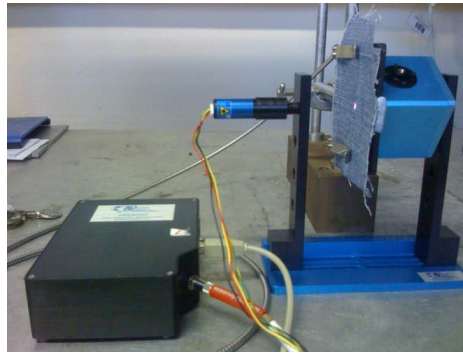
Figure 2.21 – Experiments to measure total transmitted intensity with integrating sphere

The intensity readings recorded across four representative fabric samples are shown in Figure 2.22. As opposed to Figure 2.15, the readings for wool are higher in this case than cotton (trousers), which is in conformity with the higher porosity of wool. However acrylic, with lower porosity than that of wool, still records higher readings than wool. This could be the result of greater backscatter from the surface of wool caused by the significantly higher proportion of randomly-distributed scatterers in the path of the impinging NIR radiation. Similarly, greater backscatter could explain the slightly lower intensity readings recorded with two layers when the warp/weft patterns are set at right angles compared with when they are aligned.

The above results show that the magnitude of through-transmitted radiation depends not only on the overall porosity of the sample, but also on the size and spatial distribution of the pores.
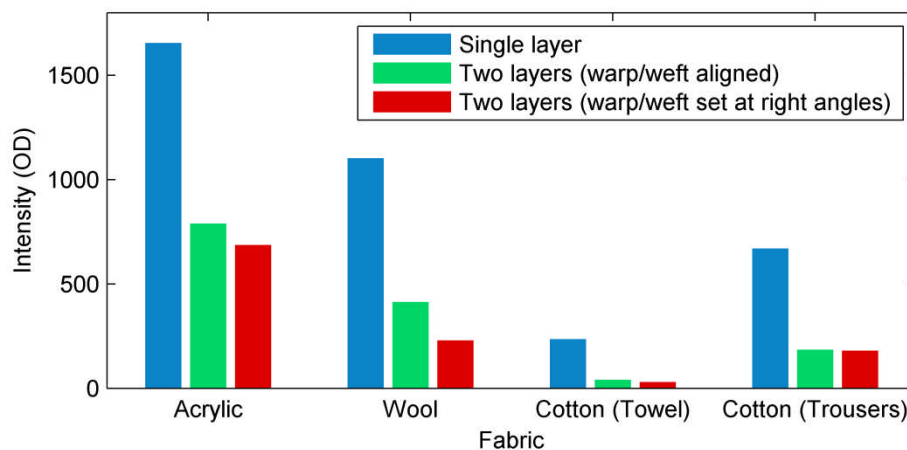
Figure 2.22 – Intensity readings recorded across fabric samples with integrating sphere

2.4 Conclusions

Based on the above observations, it may be concluded that the dominant factors in the transmission and scattering of energy across fabrics are the porosity of the fabrics and the spatial distribution of pores. While the overall porosity may determine the total amount of energy that passes through, the intensity distribution across the transmitted volume is determined by the geometric layout of the fibres, and hence that of the pores. Additionally, the chaotic surface texture of fabrics such as wool may impose further limitations on the amount of transmitted light notwithstanding the overall porosity. Furthermore, introduction of moisture in the fabrics tends to increase transmission levels by reducing the refractive index mismatch at the boundary between air and fabric, and thus reducing the optical impedance of the fabric. Therefore, dry fabrics may be expected to transmit higher intensities with increasing pore size and more uniform surface texture.

It was observed that the dye used on many fabric samples had only a minor effect on the amount of transmitted NIR energy.

2.5 References

[1] Y. Zhou, H.-r. Xu and Y.-b. Ying, "NIR analysis of textile natural raw material," *Spectroscopy and Spectral Analysis,* vol. 28, pp. 2804-7, 2008.

[2] M. S. Millan, J. Escofet and M. Rallo, "Unsupervised defect segmentation of patterned materials under NIR illumination," in *17th Reunion Iberoamericana de Optica, RIAO and 10th Encuentro de Optica, Laseres y Aplicaciones, OPTILAS,*

September 20, 2010 - September 24, 2010, Lima, Peru, 2011, p. OSA; SPIE; ICO; JPCS; Quantel; CIO.

[3] G. Wu and Y. He, "Identification of fine wool and cashmere by Vis/NIR spectroscopy technology," in *International Symposium on Photoelectronic Detection and Imaging 2007: Related Technologies and Applications, 9 Sept. 2007*, USA, 2007, pp. 66251-1.

[4] J. Havermans, H. A. Aziz and N. Penders, "NIR as a tool for the identification of paper and inks in conservation research," *Restaurator,* vol. 26, pp. 172-180, 2005.

[5] H.-F. Yuan, R.-X. Chang, L.-L. Tian, C.-F. Song, X.-Q. Yuan and X.-Y. Li, "Study of nondestructive and fast identification of fabric fibers using near infrared spectroscopy," *Guang Pu Xue Yu Guang Pu Fen Xi/Spectroscopy and Spectral Analysis,* vol. 30, pp. 1229-1233, 2010.

[6] V. Corluka, M. Filic and Z. Valter, "Lock-in amplifier in NIR reflectance measurement system," in *Annals of DAAM for 2005 & Proceedings of the 16th International DAAM Symposium "Intelligent Manufacturing & Automation: Focus on Young Researches and Scientists", 19-22 Oct. 2005*, Vienna, Austria, 2005, pp. 75-6.

[7] N. Markevich and I. Gertner, "Comparison among methods for calculating FWHM," *Nuclear Instruments & Methods in Physics Research, Section A (Accelerators, Spectrometers, Detectors and Associated Equipment),* vol. A283, pp. 72-7, 1989.

[8] S. Tagesen and G. Winkler, "Troubles, traps and tricks in fitting exponential decay data," in *International Symposium on Nuclear Data Evaluation Methodology, 12-16 Oct. 1992*, Singapore, Singapore, 1993, pp. 267-72.

[9] Y. Thomas, K. C. Cole, L. E. Daigneault and L.-M. Caron, "In-line NIR monitoring of composition and bubble formation in polystyrene/blowing agent mixtures," *Journal of Engineering and Applied Science,* vol. 2, pp. 1855-1859, 1996.

[10] Agar-Scientific. (2011, 12/05/2010). *Agar Scientific - Catalogue sections - Grids*. Available:

http://www.agarscientific.com/catalogue/action_catalogue.asp?sat=2&saa=2&path=(G|1|||0|1)(G|1||01|1|1)

[11] J. E. Bjarnason, T. L. J. Chan, A. W. M. Lee, M. A. Celis and E. R. Brown, "Millimeter-wave, terahertz, and mid-infrared transmission through common clothing," *Applied Physics Letters,* vol. 85, pp. 519-21, 2004.

[12] D. Bhattacharyya, A. Shrotri, S. C. Rethrekar, M. H. Patil, F. A. Alisherov and T.-H. Kim, "Biometric authentication using infrared imaging of hand vein patterns," in *4th International Conference on Information Security and Assurance, ISA 2010, June 23, 2010 - June 25, 2010*, Miyazaki, Japan, 2010, pp. 108-115.

[13] W. Huang, G. Wang, X. Xu, T. Yu and Z. Yang, "Forensic inspection of document using visible and near-infrared spectral imaging," in *Optoelectronic Imaging and Multimedia Technology, 18-20 Oct. 2010*, USA, 2010, p. 78500W (12 pp.).

[14] H. Tavanai, A. Z. Hamadani and M. Valizadeh, "Colour yield in two phase wet fixation dyeing of cotton cloth with reactive dyes as a function of time, temperature and alkali concentration," *Iranian Polymer Journal (English Edition),* vol. 12, pp. 459-475, 2003.

[15] R. Kronig, B. Blaisse and J. v. d. Sande, "Optical impedance and surface coating," *Applied Scientific Research, Section B,* vol. 1, pp. 63-76, 1950.

[16] E. Hecht, *Optics / Eugene Hecht*, 4th ed. ed. Reading, Mass. :: Addison-Wesley, 2002.

[17] N. Barakat and H. A. El-Hennawi, "Interferometric Studies of Fibers," *Textile Research Journal,* vol. 41, pp. 391-396, May 1, 1971 1971.

[18] R. T. Ogulata and S. Mavruz, "Investigation of porosity and air permeability values of plain knitted fabrics," *Fibres & Textiles in Eastern Europe,* vol. 18, pp. 71-5, 2010.

[19] *SDP1000 / SDP2000 Low Range Differential Pressure Sensor for Air and Non-Aggressive Gases,* Sensirion-AG Datasheet – v4.0, October 2008.

[20] K. T. Ojala, E. Koski and M. J. Lampinen, "Reflection and transmission measurements with an integrating sphere and Fourier-transform infrared spectrometer," *Applied Optics,* vol. 31, pp. 4582-9, 1992.

Chapter 3
NIR spectroscopy through clothing

3.1 Introduction

The aim of this chapter is to demonstrate the feasibility of near infrared spectroscopy as a means of performing measurements through layers of clothing. Once this has been established, then it is possible to move on to other studies, as detailed in Chapters to follow, which would enable the identification of specific chemicals concealed behind clothing.

As detailed in Chapter 1, there are advantages offered by this technique over competing technologies. These include, amongst others, its safety in the context of personal screening (as opposed to ionizing x-rays [1, 2]), cost-effectiveness (with equipment costs significantly less than x-ray and terahertz systems [3]) and availability of detailed chemical information within the pertinent spectra. This latter property, however, necessitates a careful chemometrics-based approach in processing the results, in order to overcome the lack of specificity often encountered, for reasons explained earlier in Chapter 1.

In the context of this study, the spectral features of a range of clothing materials were investigated, and the transmission level of NIR signals was found to be sufficient for spectroscopy at detector stand-off distances of up to 3 m. The study has shown that specific chemicals both in solid and aqueous solution forms can be identified when hidden behind a layer of clothing. Examples of chemicals used in this study include ammonium nitrate (solid and in solution), other ammonium salts in solid form, and solutions of ethanol and hydrogen peroxide in varying concentrations. Details of the current measurements and results are given, together with suggestions for increasing detection sensitivity.

As mentioned above, the objective of the study is to identify chemicals through barriers such as clothing using spectral data over the NIR (0.9 – 2.5 µm) wavelength range. In this regard, the NIR transmission characteristics of various clothing fabrics as well as

spectra of the above-mentioned chemicals have been studied. It has been observed that both the microstructure of fabrics and the chemical structure of fibers have an effect on NIR transmission spectra at these wavelengths, whereas the dyes used by textile manufacturers affect mainly transmission in the visible region. Hence, the measurements have been restricted to the 0.9 – 2.5 µm range in order to reduce absorption within clothing dyes and allow a study of the several spectral overtone peaks from the chemicals. The spectral features of fabrics concealing the chemical sample are superimposed on those of the hidden chemical to be detected. However, as will be demonstrated, it is found that scattering in the clothing material due to its weave structure is the dominant feature affecting transmission intensity levels.

The research was performed with the specific aim of testing the feasibility of measurements at reasonable stand-off distances. Thus, investigations were made with the spectrometer positioned at a distance of 3 m from the sample. The results presented start with a discussion of the spectral features of various fabrics and the spectra of selected chemicals of interest. It is then demonstrated that absorption peaks of these chemicals occur at the same recognizable wavelengths when they are both directly irradiated by the NIR source, and subsequently placed behind a layer of clothing. The work also shows that the chemical which needs to be detected does not have to be placed in very close proximity of the concealing fabric in order to allow a sufficiently-strong signal in diffuse backscatter. Thus, an air gap of up to 10 mm has a manageable effect on detection through most of the tested fabrics. This work represents the most current study on NIR spectroscopy through clothing for personal screening applications to date, and has recently been published [4, 5].

3.2 Background to NIR spectroscopy

Infrared spectroscopy is an established chemical technique for the identification of chemical species. Absorption peaks in the mid-infrared (MIR) region, over a wavelength range of approximately 2.5 – 25 µm, result mainly from fundamental vibrational modes of chemical bonds. However, NIR spectroscopy within the 0.9 – 2.5 µm wavelength range is based on molecular overtone and combination modes. Because of the low transition probabilities of molecular overtone and combination vibrations compared to fundamental vibrations, the strength of the absorption peaks decreases

from the MIR to the visible region by a factor of 10 – 100 between each overtone. Consequently, NIR spectra are dominated by absorption from vibrational modes that have their 1st and 2nd overtone bands in the NIR range. The fundamental absorption peaks of X-H (X = C, N, O) bonds usually occur at wavelengths lower than 5 µm, leading to their 1st overtone appearing in the NIR range below 2.5 µm. In other words, molecules incorporating CH, OH, and NH functional groups that demonstrate large mechanical anharmonicity in the vibrations of the constituent atoms will demonstrate reasonable NIR absorption [6]. NIR spectroscopy is therefore a good choice for the characterization of absorption due to substances such as water, ethanol, hydrogen peroxide, ammonium nitrate (NH_4NO_3) and other substances with suitable bonds, and tables are available to assign peaks to bonding vibrations at particular wavelengths [7].

The quantitative evaluation of a particular chemical's concentration with NIR spectroscopy is based on Beer-Lambert law:

$$A = -\log_{10}\left(\frac{I}{I_0}\right) = \varepsilon l c \qquad (3.1)$$

where A is the absorbance, I_0 the reference intensity, I the intensity after absorption, ε the molar absorptivity of the absorber, l the optical path (distance the light travels through the material), and c the concentration of the absorbing species. Hence, the quantitative value of absorbance A is based on, amongst other parameters, the reference intensity level I_0. In transmission spectroscopy, I_0 can be assigned the value of the incident light source intensity. However, this is not practicable in diffuse reflectance spectroscopy, as performed in this study. Hence, I_0 was based instead on the diffuse-reflected signal from a piece of polytetrafluoroethylene (PTFE or Teflon^{TM}), which acted as a reference. The choice of this material was based on its relatively constant optical properties over the UV to NIR wavelength range [8]. However, the use of PTFE as a standard does have its associated problems. For instance, it has been observed that physical characteristics such as thickness and surface roughness of the PTFE specimen affect the angular properties of the diffuse reflected beam. Likewise, each chemical or fabric sample reflects and scatters light in different ways. The spectra thus obtained through diffuse reflection often contain a DC offset coupled with a linear or curving function baseline shift as a result of scattering from the constituent samples and non-systematic effects. A technique known as de-trending, described below, is particularly

useful as a preprocessing step to enable comparisons between NIR spectra of chemicals collected in situations where a truly constant reference level is not available.

3.3 Experiment

The instrumentation for the study was designed to achieve the best possible balance between the definitive properties of an effective spectroscopic system, including a large range of wavelengths, high dynamic resolution and high throughput.

3.3.1 Experimental arrangement

The layout of the optical bench used for the experiments is shown schematically and photographically in Figure 3.1(a) and (b) respectively. The two main subsystems of this arrangement were a source of broadband optical illumination and a diffuse reflectance light collection system, attached to a spectrometer. Two halogen lamps were chosen as the source of optical illumination for their large emission spectrum, especially in the near infrared region. The beams from these lamps were collimated with the two lenses labeled L1 in Figure 3.1(a), and then focused with lenses L2 to obtain a homogeneous spot of illumination over a 50×30 mm^2 area on the surface of the sample under test. Diffuse reflected light from the sample was then collected via lens L3 into an optical fiber cable, which was connected to an NIR spectrometer. The spectrometer's sensor and internal grating were chosen to cover the wavelength range 860 – 2,200 nm, and gave a combined resolution of 6.9 nm. The separation between the sample being investigated and the collection subsystem was kept at 3 m to simulate chemical identification at stand-off distances. The spectrometer, connected to a PC, was controlled via SpectraSuite^{TM} software from Ocean Optics B.V. The integration time for spectrometer sensor was set at 500 ms, and an average of four spectra was taken during each reading to reduce noise. Detailed specifications of system components are given in Table 3.1.

The measurements were performed on objects generally composed of a chemical in granular solid form or in solution, held in a $50\times50\times10$ mm^3 glass cell hidden behind a layer of fabric material. The choice of glass was based on its negligible absorbance compared with the chemicals tested. For granular solids, there was a strong specular reflection, and the inclusion of the PTFE reflecting surface was not needed. However,

Chapter 3: NIR spectroscopy through clothing

when spectral readings were taken with liquids, it was observed that the liquid itself, being a weak scatterer, did not generate a sufficiently strong signal in diffuse reflectance, especially when hidden behind a fabric layer. Hence, in order to augment this signal level, a 10 mm thick PTFE block was placed behind each liquid sample, as shown in Figure 3.1, to provide a uniform diffuse reflecting surface [8]. The reasons for this reflector were given earlier in Section 3.2. The resulting arrangement is shown schematically in Figure 3.2.
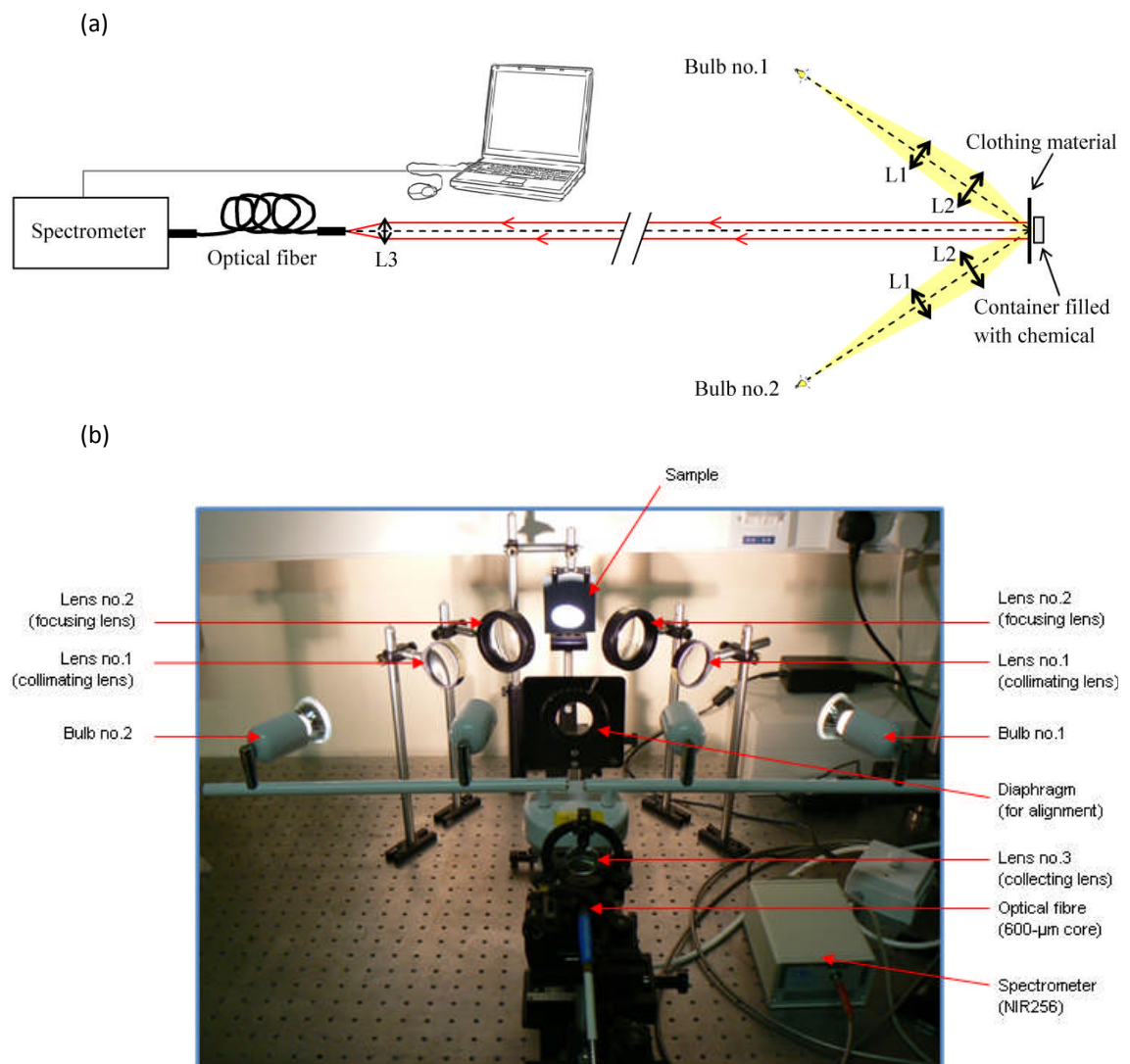
Figure 3.1 – (a) Schematic layout of the optical bench. (b) Photograph of the same arrangement (lens L3 and optical fibre cable were moved back 3 m from the sample before making stand-off spectral measurements).

It should be noted that the use of PTFE in this manner would not be possible in a practical screening application. However, it may be appreciated that in such applications, light would probably be diffused in a similar manner by other materials

present behind the chemical, such as a second layer of clothing, human skin, packaging material etc. The advantage of using PTFE in this case was based on its relatively flat spectrum in the pertinent wavelength range, which did not introduce any additional complication in the recorded spectra.

Table 3.1 – Specifications of components used in the optical bench.

Component	Qty	Vendor/ Model	Specifications
Illumination subsystem			
Halogen lamp	02	Ikea	Power: 50 W.
Lenses L1	02	Thorlabs LA1979	Plano-convex; BK7; uncoated; f' = 200mm; ϕ = 50.8mm.
Lenses L2	02	Melles Griot LPX-60.0-51.9-C	Plano-convex; BK7; uncoated; f' = 100mm; ϕ = 60mm.
Light collection subsystem			
Lens L3	01	Thorlabs LA1131	Plano-convex; BK7; uncoated; f' = 50mm; ϕ = 25.4mm.
Optical fibre cable	01	Ocean Optics VIS-NIR low OH fibre	Core = 600 µm; numerical aperture = 0.22.
NIR spectrometer	01	Ocean Optics NIR256-2.1	Sensor: InGaAs linear array (256 pixels); sensitivity range = 860 – 2 200 nm.
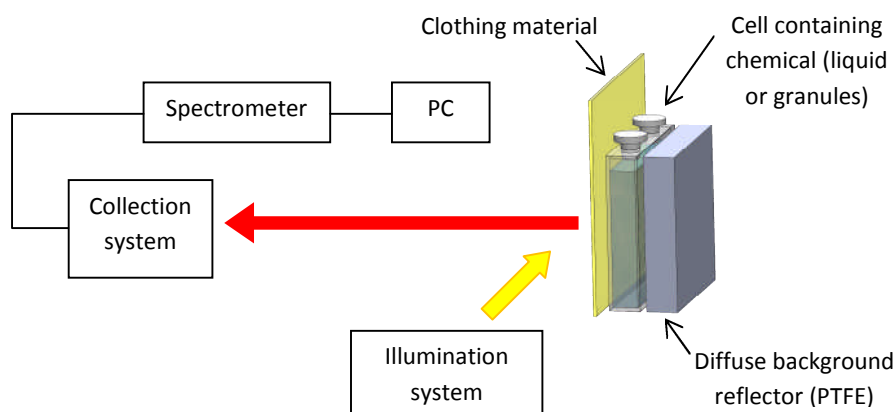
Figure 3.2 – Optical bench arrangement depicting the use of a PTFE standard reflection block with liquid samples.

In addition to its use as described above, the 10 mm thick PTFE block was also used to record reference intensity I_0. Intensity I was then recorded with the chemical cell placed as above, and absorbance A calculated.

3.3.2 Clothing materials and hidden chemicals

In order to study the effects of different types of clothing on NIR spectra, a number of different fabric samples were chosen, for the following reasons:

Chapter 3: NIR spectroscopy through clothing

- to include a variety of fabric materials (cotton, acrylic, polyester, wool…),
- to study the effect of colour on the recorded NIR spectra (white, black, multicoloured…),
- to include fabrics from different clothes (shirts, trousers…) that have different thicknesses.

The fourteen fabric samples that were used are listed in Table 3.2, and shown in Figure 3.3.

Table 3.2 – Samples of clothing fabrics used for testing.

Sample #	Fabric	Colour	Description
1	Unknown	White/ Black (cheque)	Thin texture (shirt); test sample
2	Polyester	Black	
3	Polyester	White	
4	Cotton 1	White	Soft (vest)
5	Acrylic	Off-white	
6		Blue	
7		Yellow	Same sample (originally white) dyed in various colours
8	Cotton 2	White	
9		Red	
10		Black	
11	Cotton/ Polyester	White	50% content of each fabric
12	Wool	Dark/ Patterned	Thick texture (scarf)
13	Cotton 3	Black	Thick texture (trousers)
14	Cotton (denim)	Blue	Trousers
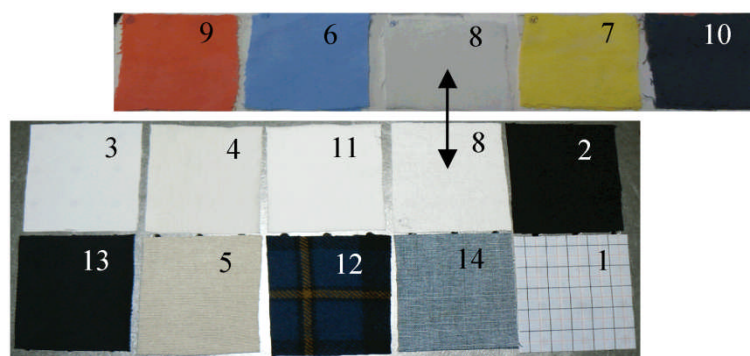
Figure 3.3 – Photographs of the 14 fabric samples, identified by numbers that correspond to the data in Table 3.2.

As can be seen, the range of samples represented a reasonable cross-section of common clothing fabrics.

The chemicals that were investigated are listed in Table 3.3. As seen, these included ammonium nitrate, a fertilizer used in the agricultural industry that can be found in improvised explosive devices (IEDs). It was obtained in two forms: (1) Fine powder containing granules with diameter in the range 0.5 – 1 mm, and (2) coarse powder comprised of even granules with 2 mm diameter and an anti-caking agent. Further experiments were performed on (3-4) other ammonium salts to determine the contribution of the ammonium ion. Additionally, experiments were performed with aqueous solutions in given concentrations made from (5) absolute ethanol (>99%), (6) 30% w/v hydrogen peroxide, and (7) reagent grade ammonium nitrate in granular form. Finally, the spectra of (8) table sugar were collected for comparison with fabrics belonging to the same class of polymers.

Table 3.3 – Chemicals tested for detection in solid and aqueous solution forms.

SN	Chemical	Formula	Supplier	Form/ Concentration
1	Ammonium nitrate	NH_4NO_3	Fisher scientific	Powder
2	Ammonium nitrate	NH_4NO_3	Sigma-Aldrich	Large granules[1]
3	Ammonium sulphate	$(NH_4)_2SO_4$	Fisher scientific	Powder
4	Ammonium chloride	NH_4Cl	Fisher scientific	Powder
5	Ethanol	C_2H_5OH	Fisher scientific	10, 20, 30, 40, 50, 60, 70, 80, 90, 100 % v/v
6	Hydrogen peroxide	H_2O_2	Fisher scientific	3, 5, 10, 15, 20, 25, 30 % v/v
7	Ammonium nitrate	$NH_4NO_3(+H_2O)$	Fisher scientific	0.3, 0.5, 0.7, 0.9, 1.1, 1.3, 1.5 g.ml^{-1}
8	Sugar (saccharose)	$C_{12}H_{22}O_{11}$	Costcutter	Powder

3.3.3 Data pre-processing

Different pre-processing steps were carried out on the collected spectra before further analysis, in order to enhance the useful features in the spectra, suppress noise, and restrict the wavelength range to include only valid information. The processing routines were implemented in Matlab^{TM}, and involved the following steps:

- Filtering
- De-trending
- Wavelength range selection

---

[1] The sherical prills are coated with clays or diatomaceous earth to reduce water absorption by the hygroscopic ammonium nitrate. Fertilizers are often found in this form.

- Amplitude translation
- Normalization

3.3.3.1 Filtering

The first step involved filtering the raw spectra to improve its signal-to-noise ratio. This was a key step to enable subsequent extraction of useful chemical information from the spectra, especially when working with exceedingly low (up to 10 times lower) spectral amplitude signals for chemicals hidden behind fabric layers.

The kind of filter employed for the purpose was a Savitzky-Golay FIR smoothing filter. This filter, also known as a digital smoothing polynomial filter or least-squares smoothing filter, is typically used to smooth out a noisy signal whose frequency span (without noise) is large. As such, it is deemed particularly suitable for filtering spectroscopic data [9]. In this type of application, this filter performs much better than a standard averaging FIR filter, which tends to filter out a significant portion of the signal's high frequency content along with the noise. Conversely, although a Savitzky-Golay filter is more effective at preserving the pertinent high frequency components of the signal, it is less successful than a standard averaging FIR filter at rejecting noise. In this context, a Savitzky-Golay filter may be regarded as optimal in the sense that it minimizes the least square error in fitting a polynomial to frames of noisy data.

The filter used in this case comprised local 2nd-degree polynomial regression on a moving frame of 15 or 7 spectral values, with the median value of each frame replaced with the value of the corresponding polynomial evaluated at that point. A larger frame size was used for granular solids (15) than aqueous solutions (7), to allow more aggressive noise cancellation in the spectra of solids (at the cost of losing some high frequency spectral peaks) while preserving sharp peaks in the relatively less noisy spectra of the solutions.

3.3.3.2 De-trending

Each spectral reading taken during this study potentially incorporated a unique baseline shift due to the different scattering properties of the samples and/ or small angular variations in the relative positions of chemical cells, fabric samples and the reference

PTFE specimen. Such factors were understood to influence the spatial distribution of wavelengths in the diffuse-reflected signal, in turn affecting transmission through the optical fibre cable connected to the detector, as the refractive index of the optical fibre core (silica), and hence its acceptance angle, was wavelength-dependent. The resulting distortion in the spectral baseline was more pronounced in the spectra of solids, presumably due to greater scattering of the interrogating signal by these samples.

With the distribution of the diffuse reflected signal thus influenced by multiple factors, it was observed that the resulting spectral baseline shift could be closely approximated by 1st or 2nd degree polynomial curves. Thus, the spectra could be regressed in a least squares sense to fit a polynomial $p(x)$ of the form:

$$p(x) = p_1 x^n + p_2 x^{n-1} + \cdots + p_n x + p_{n+1} \tag{3.2}$$

where n, the degree of the polynomial, was set to either 2 or 1, and x represented the wavelength channels (independent variables). Having thus obtained the coefficients $(p_1, p_2, p_3 \ldots)$, $p(x)$ was evaluated for all wavelength channels x:

$$y = p(x) \tag{3.3}$$

The vector y was then used to calculate the de-trended spectra [10]:

$$S_d = S - y \tag{3.4}$$

where S_d and S were the de-trended and the original spectra respectively.

An illustration this process, using filtered absorbance spectra of white polyester fabric recorded with two different reference levels, is given in Figure 3.4. As seen in Figure 3.4(a), the same absorption peaks occur in both cases, confirming the origin of these peaks in the polyester sample. However, the baseline shift, dictated by the pertinent reference levels, is different in each case and can be approximated with least squares regression as shown. These regression functions are then used in (3.3) and (3.4) to obtain the de-trended spectra shown in Figure 3.4(b). With the artificial baselines thus removed and the spectra zero-centred, this demonstrates the effectiveness of this technique in enhancing the spectral features and facilitating subsequent comparisons amongst spectra.
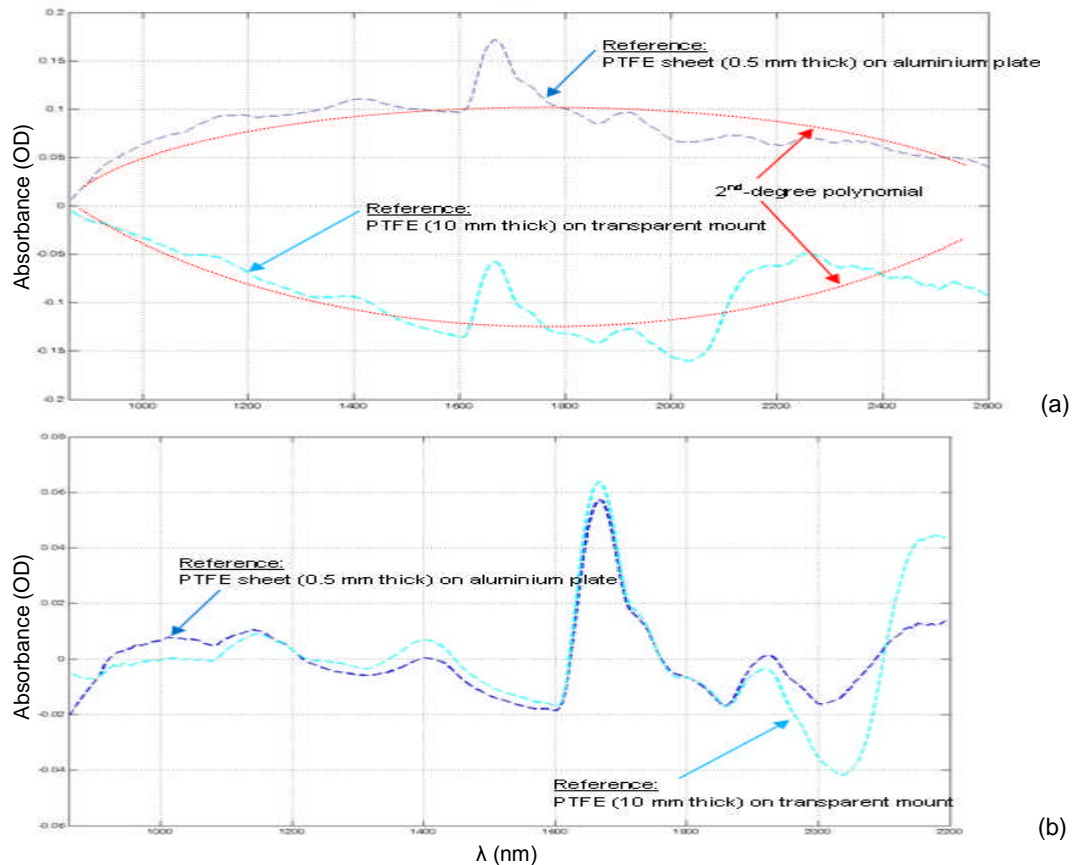
Figure 3.4 – Absorbance spectra of white polyester fabric sample, recorded with two different references. (a) 2nd degree polynomial functions that fit the spectra in a least squares sense. (b) Spectra in (a) after de-trending, illustrating same spectral features in the two cases.

The algorithm was mainly used to de-trend the spectra of solid chemicals. In the case of liquids, weaker scattering generally amounted to a constant DC offset in the baseline, which was eliminated as explained in Section 3.3.3.4.

3.3.3.3 Wavelength range selection

The spectrometer used in this study (see Table 3.1) had a default wavelength range of 854 – 2,620 nm. However, the range used for spectral analysis needed to be curtailed in accordance with the sensitivity of the spectrometer's sensor array. As seen in the spectral response curve of the spectrometer (marked NIR256-2.1) in Figure 3.5 [11], the sensitivity dropped sharply between 2,100 – 2,200 nm. Accordingly, the upper range limit for all subsequent analysis was set at 2,000 nm.

In addition to the above, the nature of the spectra collected with liquid samples further restricted the useable wavelength range. This resulted from exceptionally strong absorption due to the first overtone of water (1,450 nm) [6], which typically saturated

Chapter 3: NIR spectroscopy through clothing

the spectra in the 1,400 – 1,800 nm wavelength range. An illustration of this phenomenon is given in Figure 3.6(a), where the spectra of water and ethanol are seen to saturate in the said range, irrespective of the contents or concentration of sample solutions.
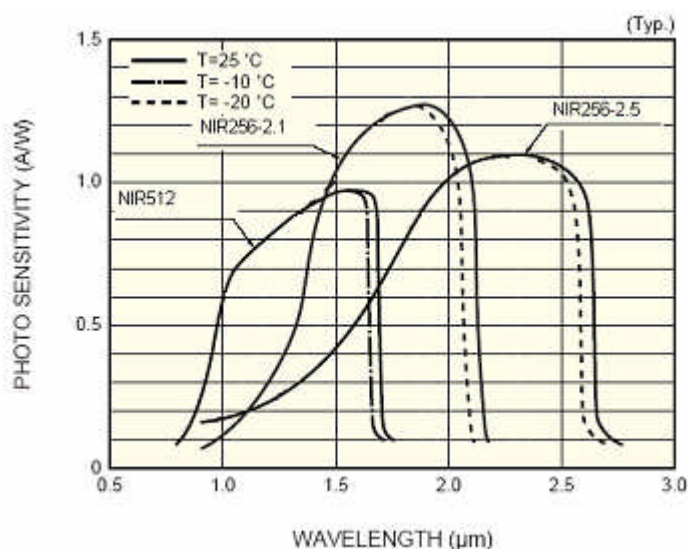
Figure 3.5 – Spectral response curve of spectrometer (marked NIR256-2.1) [11]

In order to verify the origin of this saturation, a number of spectral readings of water were taken in glass cells of different sizes, thus varying the optical path length l in equation (3.1). The results are shown in Figure 3.6(b). As seen, the first overtone at 1,450 nm is well-defined for optical paths shorter than 1 mm, with spectral saturation progressively setting in at longer path lengths. As all subsequent experiments were conducted using chemical cells with a width of 10 mm (ref. Section 3.3.1.2), which corresponded to a minimum optical path length of 20 mm in diffuse reflectance for liquid samples, the upper wavelength limit for all liquid spectra was set at 1,350 nm.

3.3.3.4 Amplitude translation

This technique was used to correct the baseline shift in the spectra of chemicals in solution form. In this case, the relatively low repeatability error, arising from factors such as minor variations in the temperature of the sensor and positioning of the clear sample solutions, introduced relatively less baseline distortion as compared with granular solids. This typically showed up as a nearly constant amplitude offset (positive or negative) across all wavelength channels. As the spectra of liquids were known to saturate at wavelengths longer than 1,400 nm (see Section 3.3.3.3), this offset was

removed by translating the spectra along the amplitude axis so as to have a constant absorbance value at a specific wavelength channel (1 600 nm) in the saturated region. Finally, with this DC shift implemented, the saturated regions were discarded as above. The process generally produced spectra that were arranged in accordance with the relevant sample concentrations in solution. This can be seen in Figure 3.7, which shows spectra of ethanol samples in various concentrations pre-processed as above.

(a)   (b)
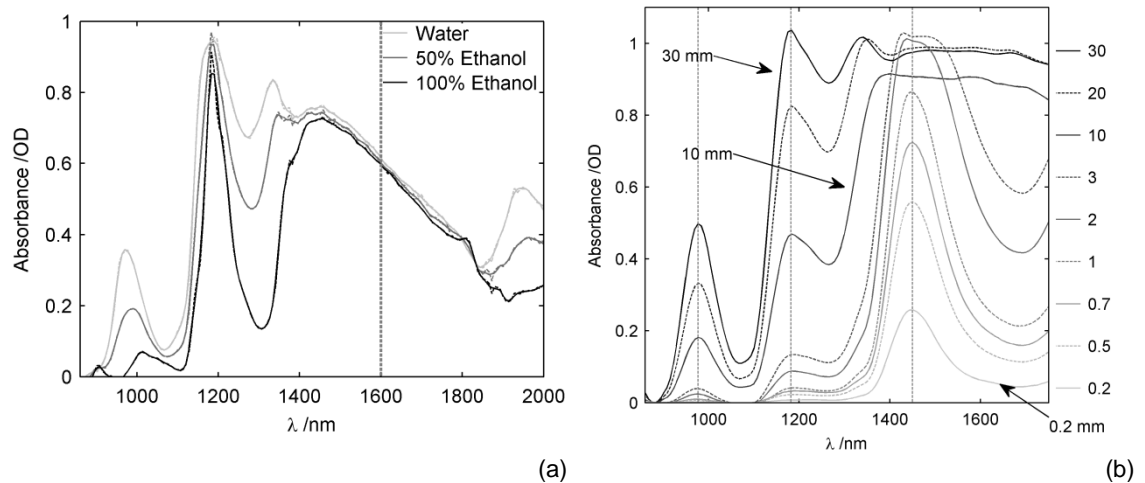
Figure 3.6 – Spectral saturation due to the first overtone of water (1 450 nm). (a) Spectra of water and two ethanol solutions, showing saturation in the 1 400 – 1 800 nm wavelength range (measured in diffuse reflection with optical path ~20 mm; reference: empty cell with PTFE). (b) Spectra of water for different optical paths (measured in transmission in glass cells of different widths); the first overtone is defined for path lengths up to 1 mm.

3.3.3.5 Normalization

An optional final step involved normalizing the spectra to span the values between 0 – 1. This allowed enhancement of spectral features for effective comparisons, albeit with the loss of original spectral amplitudes.

3.4 Results

3.4.1 Properties of clothing fabrics in the NIR region

The optical transmission characteristics of various clothing fabrics were investigated by measuring the amplitude of through-transmitted signals over the 900 – 1,300 nm wavelength range. An integrating sphere was used to measure the cumulative transmission intensity over this range, in order to verify the presence of sufficient through-transmitted signal levels in this region of the spectrum. The results are shown for various fabric samples in Figure 3.8. As can be seen, most of the fabrics exhibit

transmission levels that exceed 30% in this wavelength range. It can also be seen that NIR transmission depends not only on the fibre material, but also on the particular weave of the material.
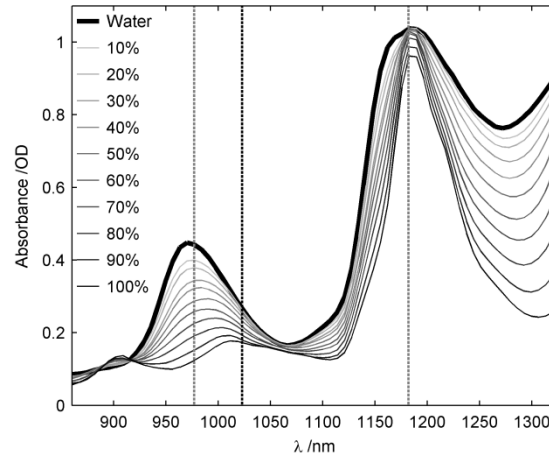
Figure 3.7 – Spectra of water and ethanol solutions in various concentrations, after filtering, translation and range selection (measured in diffuse-reflectance across optical path of 20 mm, with reference to empty cell and PTFE)
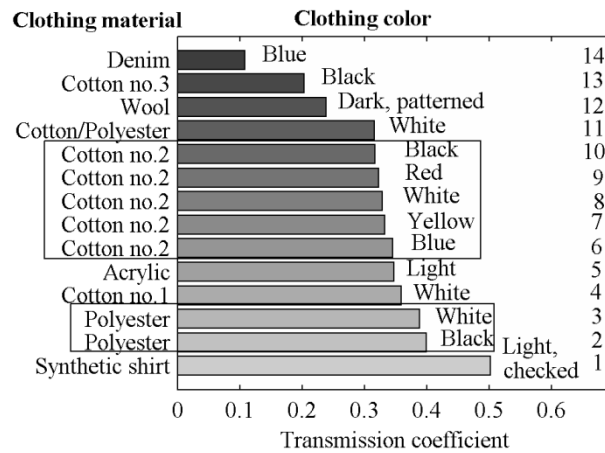
Figure 3.8 – Transmission coefficients of fabric samples listed in Table 3.2. Measurements were made in through-transmission, using an integrating sphere to determine the total integrated transmission intensity over the 900 – 1,300 nm wavelength range.

This can be illustrated further by studying the weave pattern of three samples (cotton no. 1, cotton no. 3 and denim (a rugged cotton twill textile)), using a conventional optical microscope, as shown in Figure 3.9. For cotton no. 1 sample, clear air pores between fiber strands are observed. On the other hand, cotton no. 3 and denim have lower porosity due to tighter weave and larger diameter fiber strands, which serves to reduce pore density. Hence, based on the relative transmission levels observed through these samples, it was assumed that the main contribution to the NIR transmission

coefficient was from photons transmitted through the pores. However, while Figure 3.9(d) shows that the pores in polyester sample are small compared with the size of the strands, meaning polyester sample has lower porosity than cotton, the former was seen to have a higher transmission coefficient. This was attributed to the fact that the polyester sample was one of the thinnest samples tested, which aided in higher transmission through the solid woven fibre. It thus appears that the weave pattern as well as material thickness affect the scale of NIR transmission.
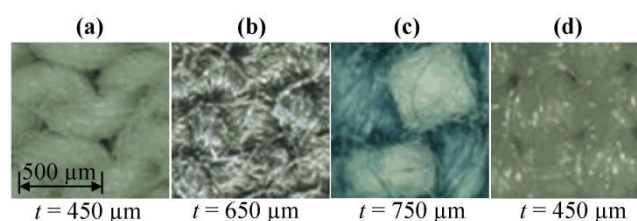
Figure 3.9 – Optical microscope photographs of selected fabric samples; (a) white cotton (cotton no. 1), (b) black cotton (cotton no. 3), (c) denim and (d) white polyester. The thickness t of each sample is also shown.

Figure 3.8 also shows that dye colour does not have any significant impact on optical transmission in the NIR region. To study this further, the absorbance spectra of dyed cotton samples (cotton no. 2 in Figure 3.8) were measured in diffuse reflectance with the apparatus shown in Figure 3.1, over both the visible (main figure) and NIR (inset) wavelength range. The reference intensity I_0 was taken as the intensity of light reflected by the 10 mm thick PTFE block in the absence of fabric sample. Each fabric sample was then placed in turn in front of the PTFE block and the intensity spectra recorded. SpectraSuite^{TM} was used to record all intensity levels and display the corresponding absorbance spectra. As can be seen in Figure 3.10, dyes present strong absorption characteristics in the visible wavelength range and the relevant absorption levels are characteristic of the particular dyes, most likely based on the relevant colours. For instance, a red dye appears red to the human eye because it reflects rays from 600 to 750 nm. Therefore, its absorption will be in the blue-green range, as seen in Figure 3.10.

Another important observation is that absorption amplitude in the NIR range is approximately 10 times lower than that in the visible range, and does not depend to any significant degree on the colour of the sample (the four curves are plotted on top of each other in the NIR region). This latter characteristic is one of the reasons why the NIR

wavelength range is considered to be a good choice for spectroscopy of materials hidden behind clothing.
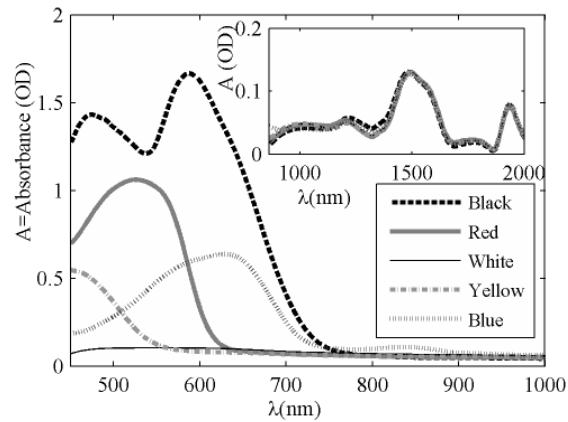
Figure 3.10 – Absorbance spectra of cotton no. 2 samples (ref. Table 3.2 and Figure 3.8) in both visible (main window) and NIR (inset) wavelength range. Diffuse reflectance measurements were made with reference to 10 mm thick PTFE block. Data were filtered and 1ˢᵗ-degree de-trended.

The NIR absorbance spectra of various clothing materials were next measured using the same procedure, with the results shown in Figure 3.11. Based on the spectral features observed, the samples can broadly be classified as either synthetic (Figure 3.11(a)) or natural (Figure 3.11(b)) fabrics. The absorption peaks of cotton, a natural fabric, occur at 1,210, 1,488 and 1,935 nm, which is commensurate with the results reported in literature (1,216, 1,490 and 1,930 nm [12]). Additionally, the spectra of wool, another natural material, contain peaks similar to cotton at 1,490 and 1,935 nm. However, wool seems to have very distinct spectral features at lower wavelengths as well, where a high absorption peak in the 860 – 1,000 nm range sets it apart from the relatively flatter profiles of all other materials at these wavelengths. With regards to synthetic materials, the spectra of polyester are seen to contain peaks at 1,135, 1,389 and 1,665 nm, which compares favorably with the results reported in literature with peaks at 1,128, 1,368 – 1,412 and 1,660 nm [12]. Moreover, the spectra of acrylic, also synthetic in nature, exhibit similar features with a slight shift towards longer wavelengths.

As seen above, the differences between the results reported in literature and those obtained here are relatively small, and attributable to the limited sampling resolution (6.9 nm) of the spectrometer model used here. The average amplitude of recorded spectra of clothing is around 0.1 optical density (O.D), which is a few orders of

magnitude lower than the spectra of chemicals alone, as shown in the next section. This is deemed to be a favorable outcome, as it points towards stronger absorption by the chemical species than the concealing fabrics. Furthermore, absorption in fabrics is seen to generally increase at longer wavelengths, and thus a stronger influence of clothing on the spectra of hidden chemicals would be expected at wavelengths greater than 1,400 nm or so. Finally, it is seen that comparing the spectra of an unknown fabric sample (such as 'Check shirt' in Figure 3.11(a)) with a known fabric's spectrum allows an inference to be drawn about the composition of such a sample. In this case, the said sample might contain cotton and polyester in equal measure, as peaks of both these fabrics are seen in the spectrum of the sample.

(a)   (b)
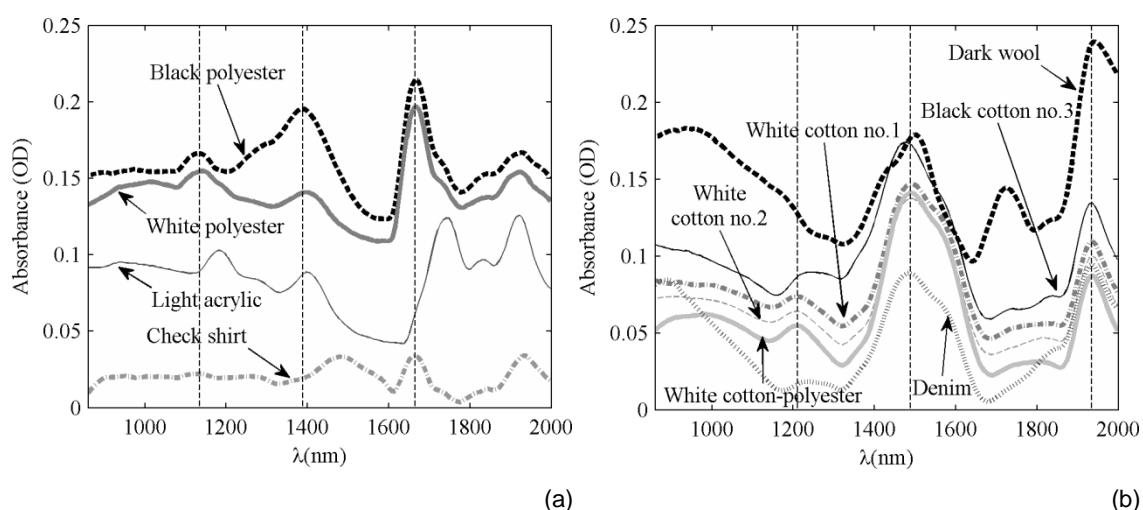
Figure 3.11 – NIR spectra of fabrics: (a) Synthetic materials including polyester and acrylic, and (b) natural materials including cotton, cotton-polyester, wool and denim. Diffuse reflectance measurements were made with 10 mm thick PTFE block as reference. Data were filtered and 1st-degree de-trended. DC offsets were introduced in the displayed spectra for visual clarity.

Interestingly, the spectra of cotton are seen to have features in common with the spectra of table sugar (saccharose or sucrose) as shown in Figure 3.12. This is borne out of the fact that both cellulose (the main constituent of cotton) and sucrose (a disaccharide of glucose and fructose) are polysaccharide polymers that have similar arrangements of C, O and H atoms.

The above results demonstrate that NIR spectra can be recorded at stand-off distances of 3 m, and that the absorption in different types of clothing materials is relatively low over the 0.9 – 2 µm NIR range. Thus, detection of certain chemicals behind clothing

materials might be possible due to the significant transmission of NIR signals through such barriers. The next set of measurements was thus designed to investigate this for common chemicals in granular form.
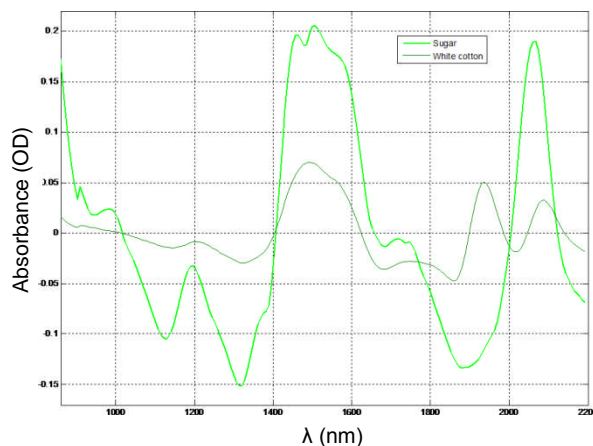
Figure 3.12 – Absorption spectra of table sugar (sucrose) and white cotton.
Data were collected in diffuse reflectance, filtered and de-trended.

3.4.2 Solid chemicals (ammonium salts) and clothing materials

As explained previously, only molecules with high anharmonicity would be expected to be strong absorbers in the NIR range. Hence, ammonium salts would be expected to have similar spectral content due to N-H bonds in the NH_4^+ ion, but each would be slightly different. To demonstrate that NIR spectroscopy is a viable technique for detecting such chemicals concealed behind clothing, granular ammonium nitrate and other ammonium salts were investigated as below.

3.4.2.1 Granular ammonium salts alone

Figure 3.13 shows the spectra of ammonium nitrate (NH_4NO_3), ammonium chloride (NH_4Cl) and ammonium sulphate (NH_4SO_3) with no clothing material present, using PTFE as the reference reflector to record I_0. It can be seen that ammonium nitrate from two different commercial suppliers (ref. Table 3.3) had the same three absorption peaks at 1,059, 1,272 and 1,568 nm, as indicated by the vertical dashed lines. The fine-grained and coarse-grained forms of the salt might have had an influence on the baseline shift (removed in Figure 3.13), but the physical form does not seem to affect the spectral content. The 1,568 nm band corresponds to the 1st overtone stretch of N-H bonds, whereas the 1,059 nm band corresponds to the 2nd overtone stretch. The 1,272 nm band

is attributed to a combination of N-H stretching and N-H bending. This peak is also related to a 2,012 nm peak which is well-documented in the literature [13].
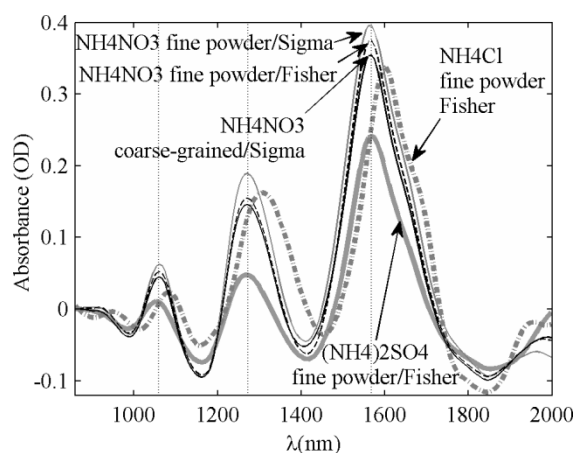
Figure 3.13 – NIR absorbance spectra of ammonium salts containing nitrate, sulphate and chloride ions (reference: 10 mm thick PTFE block). The measurements were made in diffuse reflectance, filtered and 1ˢᵗ degree de-trended.

As explained in Section 3.3.3.3, the range of wavelengths over which the spectra were collected was restricted to 860 – 2,000 nm for solid granules (and less for liquids – see above), because the sensitivity of the spectrometer fell sharply at wavelengths above 2,100 nm. In this way, the overall signal-to-noise ratio (SNR) was increased. The measurements indicted that ammonium sulphate had exactly the same absorption peaks as ammonium nitrate, while the peaks of ammonium chloride were shifted by about 30 nm towards higher wavelength. This shift was attributed to the difference in electro-negativity between nitrate and chloride ions.

3.4.2.2 Ammonium salts behind fabric layers

The data in Figure 3.14 is for ammonium nitrate and ammonium chloride when positioned behind a checked cloth sample. Reference I_0 in this case was taken as the diffuse-reflected signal from the fabric sample, before the chemical cell was positioned behind it. This served to enhance chemical detection as most of the spectral content of the fabric sample was removed from the absorbance spectra collected. It may be noted that the PTFE block was not used in this set of measurements in order to allow closer approximation to a real-life application.

The resulting spectra demonstrate that even with clothing present, the expected NIR absorption peaks of ammonium nitrate and ammonium chloride remained intact, with

the 30 nm shift in ammonium chloride spectra as mentioned above still present. It can also be seen that the amplitude of these spectra is about 0.08 O.D, which is on the same order of magnitude as the spectra of fabric samples in Figure 3.11, and approximately 6 times lower than the spectra of the chemicals alone in Figure 3.13.
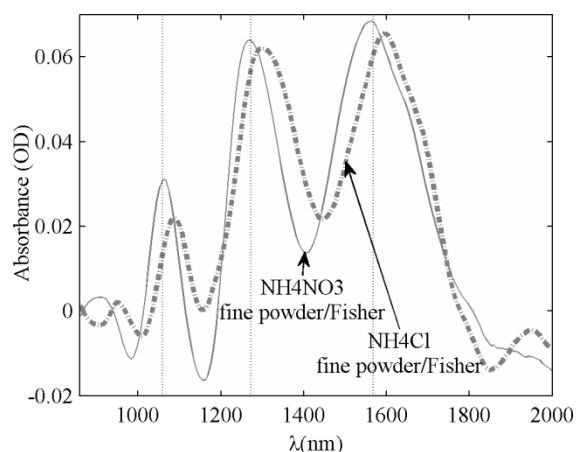
Figure 3.14 – NIR absorbance spectra of ammonium nitrate and ammonium chloride behind a synthetic check shirt (reference: fabric sample). The measurements were made in diffuse reflectance, filtered and 1ˢᵗ degree de-trended.

A further study was carried out to test ammonium nitrate concealed behind different clothing materials. The results, divided between the spectra collected with synthetic fabrics and natural fabrics, are shown in Figure 3.15. The amplitude of the recorded spectra in each case depended on the NIR signal transmitted through individual fabric samples. Hence, all spectra were normalized to an amplitude range of 0 to 1 in order to facilitate comparisons.

The results show that, although the spectral features of ammonium nitrate (peaks marked by dashed vertical lines) remained well-preserved behind synthetic fabrics, they became relatively less distinct behind natural fabrics. However, even for the worst case of denim, which had exceptionally low transmission coefficient as shown in Figure 3.8, the three expected peaks were still present with very little shift in wavelength. As previously discussed, this increased attenuation of the signal through the fabric sample was a consequence of increased scattering by the fibers resulting from a lack of air pores.
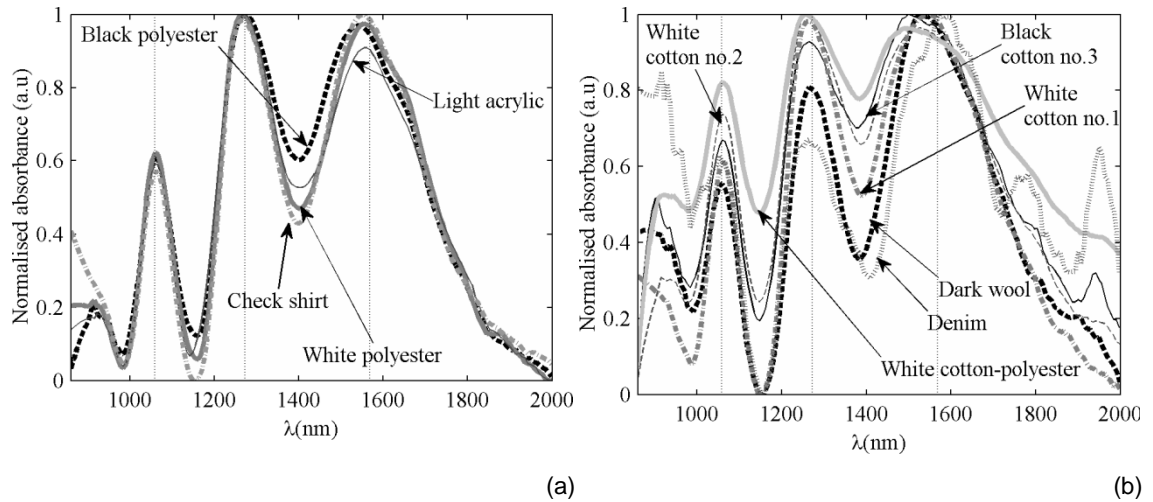
Figure 3.15 – Absorbance spectra of coarse-grained ammonium nitrate granules (provided by Sigma-Aldrich Ltd) (a) behind synthetic fabrics, and (b) behind natural fabrics. The measurements were made in diffuse reflectance, with reference to the fabric samples. Spectra were filtered, de-trended and normalized.

3.4.2.3 Varying separation between fabric sample and chemical cell

The effect of an air gap between the fabric sample and chemical cell was also investigated by varying this gap from 0 to 20 mm. The results are shown in Figure 3.16. Although the spectral amplitude was seen to decay exponentially with increasing air gap behind most fabrics, it was still possible to measure spectra with amplitudes greater than 0.01 O.D with the largest air gap between the cloth and the chemical cell.
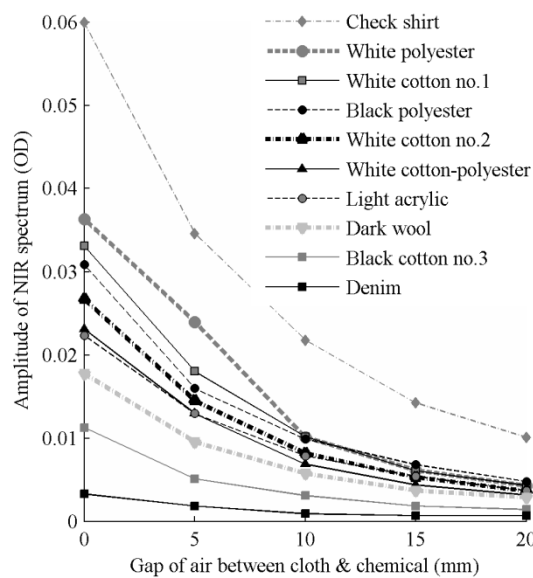
Figure 3.16 – Spectral amplitudes of coarse-grained ammonium nitrate (provided by Sigma-Aldrich Ltd) behind different fabrics for varying air gap between the sample and the clothing material. The peak-to-peak amplitude is plotted between the 1 169 nm minimum and the 1 279 nm maximum. This was obtained from filtered and de-trended spectra measured in diffuse-reflectance with reference to the fabric samples.

The curve for denim appeared almost flat as the amplitude of the signal reached the level of noise after a few millimeters. This meant that the modulation of denim's spectra by ammonium nitrate was on the same order of magnitude as the natural variations in those spectra (due to surface roughness, temperature etc.). However, as already mentioned, denim in this context presented the worst case scenario. Improvements in the quality of illumination of samples would increase the SNR, which would be especially beneficial in the case of fabrics with such dense weave structures.

3.4.3 Liquid chemicals and clothing materials

In the following sections, spectra of liquid chemicals are presented in solution concentrations given in Table 3.3, followed by spectra of the same chemicals placed behind different clothing fabrics. Distinctive spectral features recorded in each case are discussed alongside.

3.4.3.1 Liquid chemicals alone

Absorbance spectra of ethanol, hydrogen peroxide and ammonium nitrate in various concentration solutions are shown in Figures 3.17, 3.18 and 3.19 respectively. All these measurements were made in diffuse reflectance with total path length 20 mm, and the spectra were pre-processed through filtering and amplitude translation. Absorbance values were recorded with reference to signal I_0 from the PTFE block placed behind (a) an empty cell; (b) a cell containing water. The spectra collected in the former case (Figures 3.17(a), 3.18(a) and 3.19(a)) demonstrate the influence of water content in each case, where the characteristic features of water tend to dominate the spectral profile. However, measuring absorption with reference to water established water as the baseline (the zero-amplitude axes in Figures 3.17(b), 3.18(b) and 3.19(b)), so the resultant spectral amplitudes were proportional to the magnitude of their departure from the spectra of water. It is worth noting that spectra measured in this manner i.e. with reference to water exhibit higher amplitude resolution amongst different concentrations, while emphasizing features that are unique to the constituent chemicals.

The spectral peaks marked in graphs (a) at 977 nm and 1,182 nm are characteristic peaks of water. Similarly, the peaks and valleys marked in Figure 3.17(b) at 970 and 1,155 nm, in Figure 3.18(b) at 1,066 and 1,203 nm, and in Figure 3.19(b) at 960, 1,149

and 1,196 nm are amongst the characteristic features of ethanol, hydrogen peroxide and ammonium nitrate solutions respectively.
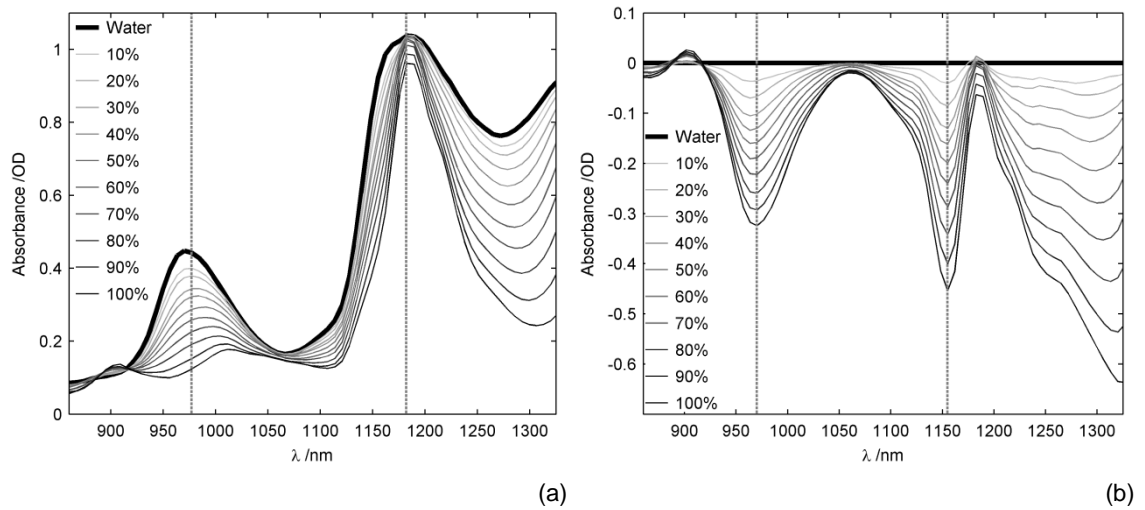
Figure 3.17 – Absorbance spectra of water and ethanol in various concentrations, measured with reference to a block of PTFE placed behind (a) an empty cell; (b) a cell containing water.

In Figure 3.17(a), the apparent decrease in the amplitude of the peak at 1,182 nm with increasing concentration of ethanol samples is an anomaly introduced by the filtering step, as the relevant peak of ethanol is too sharp to be accurately preserved.
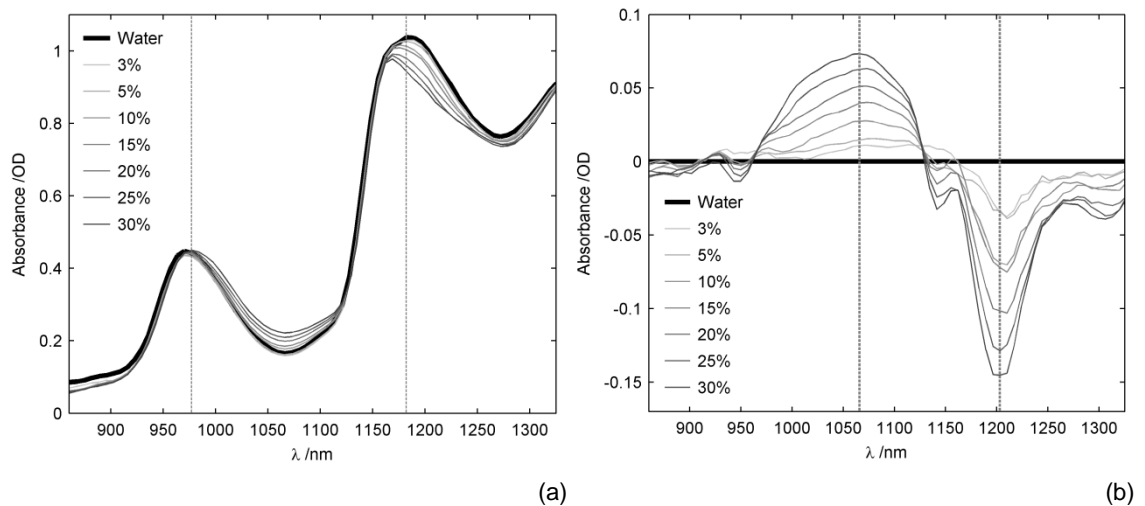
Figure 3.18 – Absorbance spectra of water and hydrogen peroxide in various concentrations, measured with reference to a block of PTFE placed behind
(a) an empty cell; (b) a cell containing water.

It may be noted that while the influence of water is apparent in all cases, the spectra of hydrogen peroxide in Figure 3.18(a) are especially close to the spectra of water. This is deemed to be a consequence of the relatively low concentrations of hydrogen peroxide

Chapter 3: NIR spectroscopy through clothing

used in measurements as compared with either of the other two chemicals, as well as similarities in the chemical structure of water and hydrogen peroxide. Further, the amplitudes of peaks and valleys in all spectra measured with reference to water are seen to vary linearly with concentration, with the possible exception of the valley of hydrogen peroxide at 1,203 nm (Figure 3.18(b)). The loss of definition in the latter case is again an outcome of the relatively less distinctive features in the spectra of hydrogen peroxide, especially at the available concentrations.
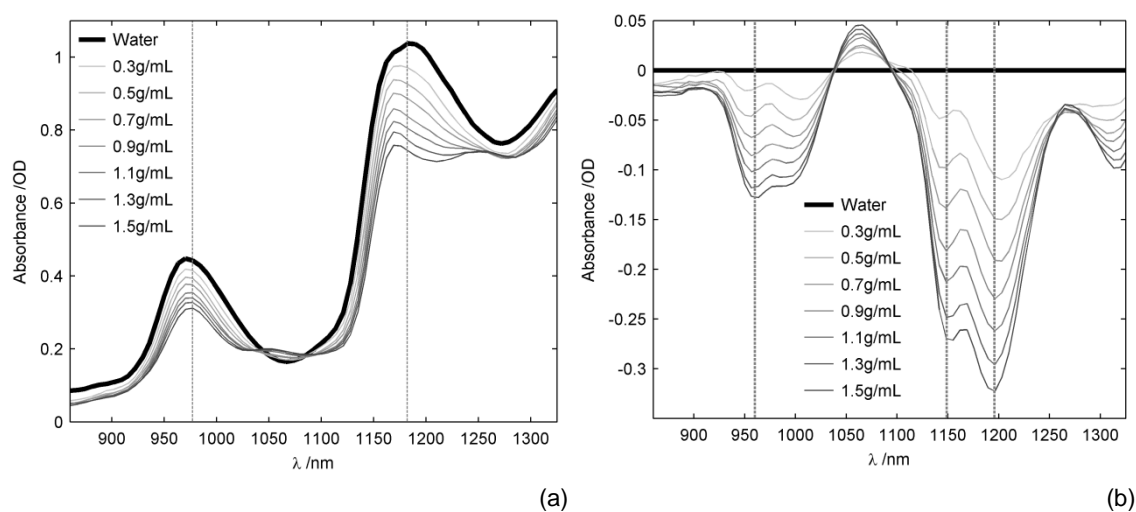
Figure 3.19 – Absorbance spectra of water and solutions of ammonium nitrate in various concentrations, measured with reference to a block of PTFE placed behind (a) an empty cell; (b) a cell containing water.

3.4.3.2 Liquid chemicals behind fabric layers

Spectra were collected for all liquid samples placed behind specific fabric layers. The fabrics used in these measurements included samples of polyester, cotton, acrylic and wool (samples no. 3, 4, 5 and 12 in Table 3.2). The spectra of ethanol, hydrogen peroxide and ammonium nitrate solutions placed behind these fabric samples are shown in Figures 3.20, 3.21 and 3.22 respectively. All these spectra were recorded in diffuse reflectance with the samples arranged as shown in Figure 3.2. The total optical path length, therefore, comprised the path traversed through the liquid (20 mm) and twice the thickness of the fabric sample (at initial incidence and after reflection). The spectra were pre-processed by filtering and amplitude translation. Reference intensity I_0 was recorded with the PTFE block placed behind (a) an empty cell, with the relevant fabric sample placed in front; (b) a cell containing water, again with the relevant fabric sample covering the front end.
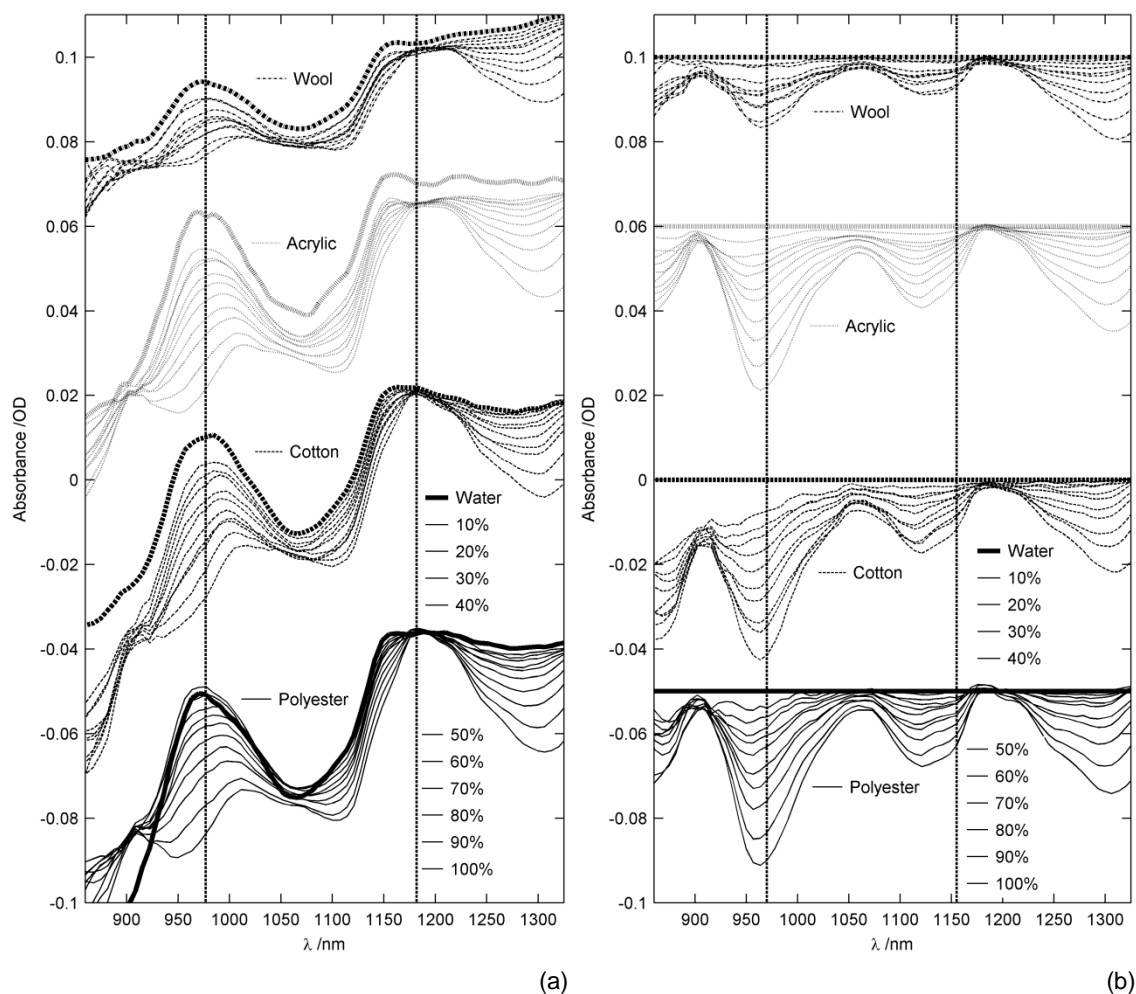
Figure 3.20 – Absorbance spectra of water and ethanol in various concentrations, placed behind different fabric layers, measured in diffuse reflectance with reference to a block of PTFE placed behind (a) an empty cell covered with the fabric sample; (b) a cell containing water, covered with the fabric sample.

In order to facilitate comparisons, the vertical dotted lines marking spectral features in all the above spectra have been drawn at the same wavelength channels as in the corresponding spectra without fabric layers in Section 3.4.3.1. Accordingly, the spectral features of ethanol may be compared between Figures 3.17 and 3.20, and so forth. In graphs (a), the peaks of water at 977 and 1,182 nm can still be seen, although the latter peak appears somewhat distorted. In general, the fabric layers appear to introduce a measure of distortion in all spectra, which is especially noticeable at wavelengths greater than 1,100 nm. This becomes more evident in graphs (b), which now reflect the extent to which spectra of hidden chemicals differ from the spectra of hidden water sample (taken as reference). As seen, the resulting features are generally different to

those recorded in graphs (b) in Figures 3.17 – 3.19, which show the differences between the chemical and water samples used alone.
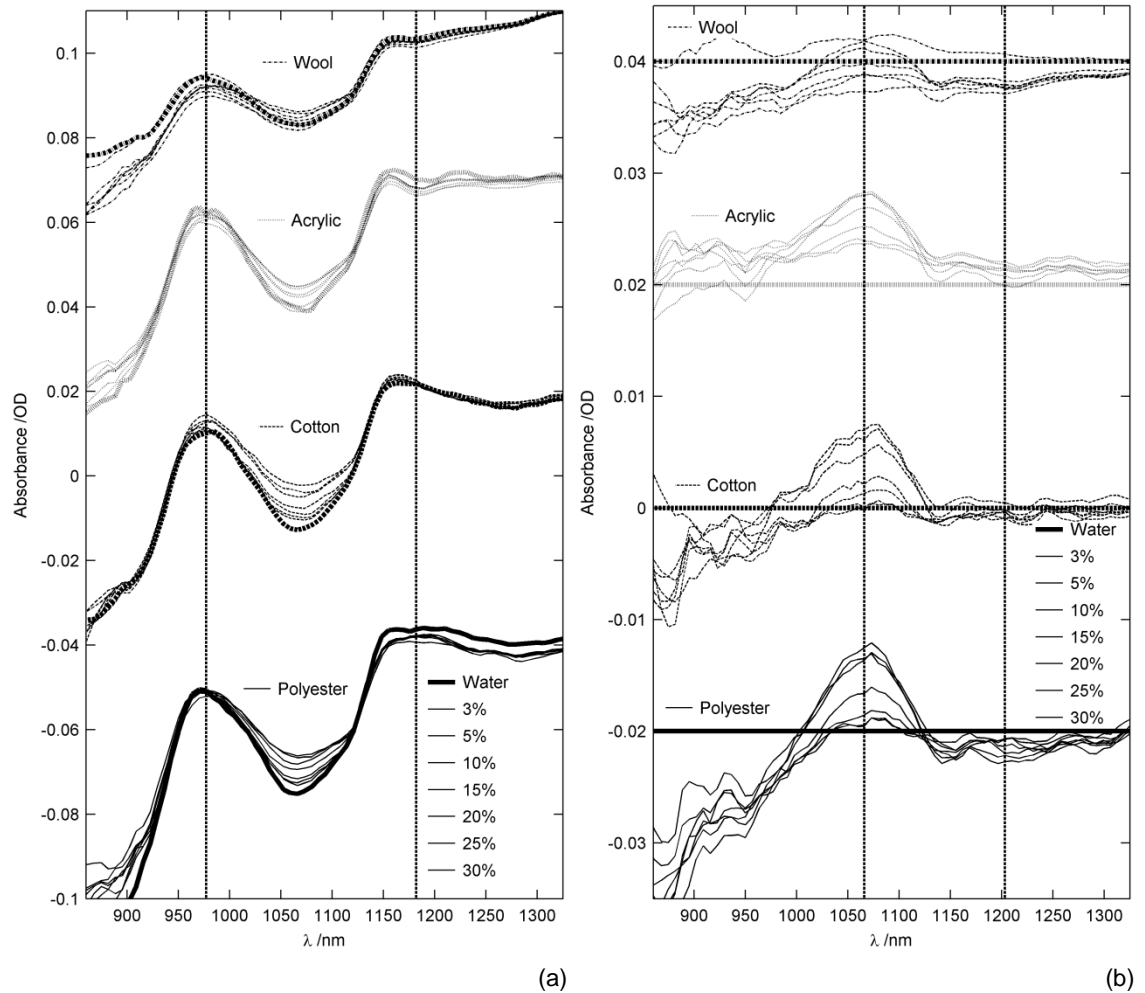
Figure 3.21 – Absorbance spectra of water and hydrogen peroxide in various concentrations, placed behind different fabric layers, measured in diffuse reflectance with reference to a block of PTFE placed behind (a) an empty cell covered with the fabric sample; (b) a cell containing water, covered with the fabric sample.

Interestingly, however, the changes introduced by the fabric samples in the spectra of each chemical appear to be quite independent of the type of fabric. This opens up the possibility of detecting such hidden chemicals using calibration models trained with the spectra of chemicals concealed behind a representative set of fabric materials, with the models able to extrapolate to detect chemicals behind fabrics not included in the training data. This is the subject of the next chapter.
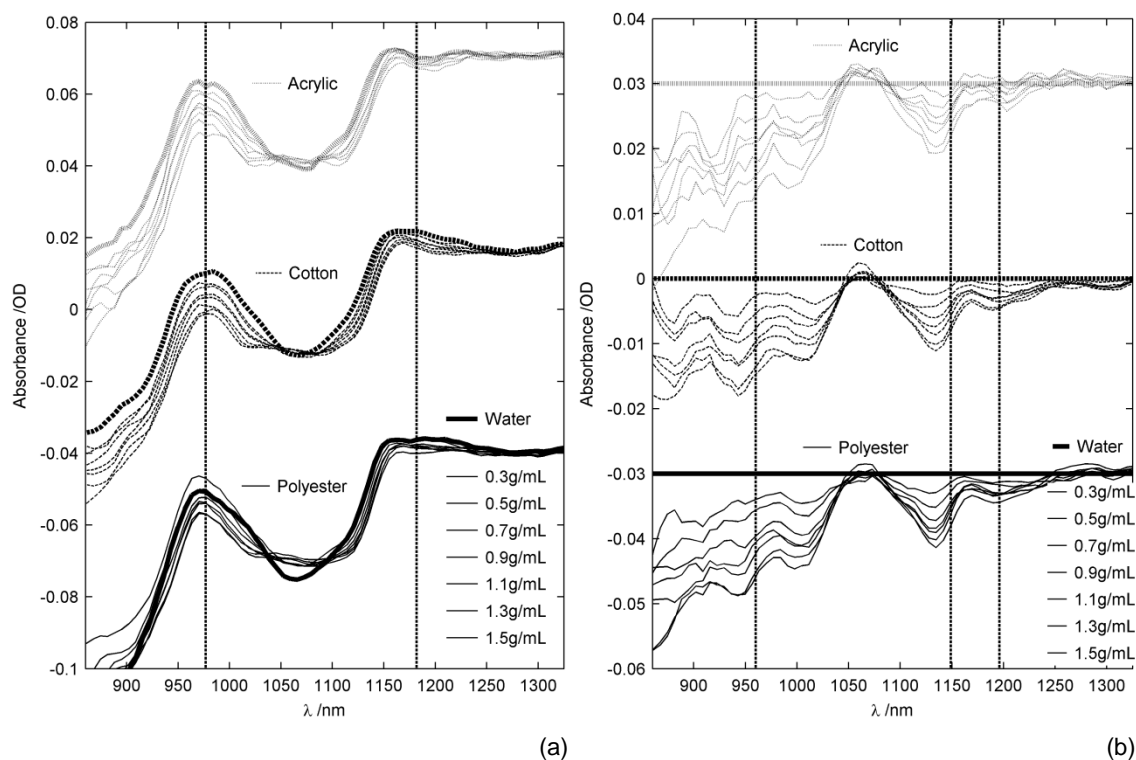
Figure 3.22 – Absorbance spectra of water and ammonium nitrate in various concentrations, placed behind different fabric layers, measured in diffuse reflectance with reference to a block of PTFE placed behind (a) an empty cell covered with the fabric sample; (b) a cell containing water, covered with the fabric sample.

3.5 Discussion and conclusions

It has been shown that NIR spectroscopy is a promising method for identification of chemicals concealed behind layers of clothing, especially if used in conjunction with appropriate chemometric analysis. In particular, it has been demonstrated that this technique could be used as a remote detection method at stand-off distances of up to 3 m. Granular solids and aqueous solutions both have a significant effect on an incident NIR signal, which then allows the detection of recognizable NIR spectra of chemicals. This includes ammonium nitrate in solid or solution form, concealed behind different clothing materials. Further experiments with other solid chemicals like nitrate salts and saccharose (sucrose) have also indicated that ammonium salts have specific well-marked peaks of absorption. Additionally, the distortion introduced by fabric layers in the spectra of liquid samples seems not to be unduly dependent on the type of fabric involved. This property might allow development of calibration models capable of extrapolation to detect chemicals hidden behind unknown fabric materials.

In a real-life application, such as personal screening at airports, the measurements would be more difficult, and enhancements to the technique would have to be considered. Thus, for example, the light source could be modulated in order to use a lock-in amplifier after the detector array. This could significantly improve the SNR of the measurement and additionally provide suppression of background-related signals. Furthermore, multivariate calibration techniques (such as PCR, PLSR, neural networks) could be used to determine the presence and concentration of a certain chemical, even in the form of mixtures and in the presence of interferents/ outliers. The use of such techniques has been studied and is the subject of the next two chapters.

3.6 References

[1] S. Singh and M. Singh, "Explosives detection systems (EDS) for aviation security," *Signal Processing,* vol. 83, pp. 31-55, 2003.

[2] M. Iovea, M. Neagu, O. G. Duliu and G. Mateiasi, "High accuracy X-ray dual-energy experiments and non-rotational tomography algorithm for explosives detection technique in luggage control," in *Proceedings of DIR 2007 - International Symposium on Digital industrial Radiology and Computer Tomography*, Lyon, France, June 25-27, 2007, pp. CD-ROM.

[3] A. G. Davies, A. D. Burnett, W. Fan, E. H. Linfield and J. E. Cunningham, "Terahertz spectroscopy of explosives and drugs," *Materials Today,* vol. 11, pp. 18-26, 2008.

[4] C. M. Canal, A. Saleem, R. J. Green and D. A. Hutchins, "Remote identification of chemicals concealed behind clothing using near infrared spectroscopy," *Analytical Methods,* vol. 3, pp. 84-91, 2011.

[5] C. M. Canal, A. Saleem, R. J. Green and D. A. Hutchins, "Near infrared spectroscopy for personal screening," in *SPIE Optics and Photonics for Counterterrorism and Crime Fighting VI and Optical Materials in Defence Systems Technology VII, September 20-23, 2010*, Toulouse, France, 2010.

[6] H. W. Siesler, Y. Ozaki, S. Kawata and H. M. Heise, *Near-infrared spectroscopy: principles, instruments, applications*: Wiley-VCH, 2006.

[7] I. Murray, "Scattered information: Philosophy and practice of near infrared spectroscopy," in *Near Infrared Spectroscopy: Proceedings of the 11th International Conference*, Córdoba, Spain, 6-11 April 2003, pp. 1-12.

[8] A. Springsteen, "Standards for the measurement of diffuse reflectance - an overview of available materials and measurement laboratories," *Analytica Chimica Acta,* vol. 380, pp. 379-390, 1999.

[9] A. Savitzky and M. J. E. Golay, "Smoothing and Differentiation of Data by Simplified Least Squares Procedures," *Analytical Chemistry,* vol. 36, pp. 1627-1639, 1964.

[10] R. J. Barnes, M. S. Dhanoa and S. J. Lister, "Standard Normal Variate Transformation and De-trending of Near-Infrared Diffuse Reflectance Spectra," *Applied Spectroscopy,* vol. 43, pp. 772-777, 1989.

[11] *NIR Fiber Optic Spectrometers,* Ocean Optics Inc. Installation and Operation Manual: Document Number 197-00000-512-02-0707, 2007.

[12] D. A. Burns and E. W. Ciurczak, *Handbook of Near-Infrared Analysis*: CRC Press, 2007.

[13] P. Patnaik, "Infrared and Raman Spectroscopy," in *Dean's Analytical Chemistry Handbook*, 2nd ed., McGraw-Hill, 2004.

Chapter 4

Multivariate calibration of spectroscopic data

4.1 Introduction

This chapter explores the chemometric multivariate analysis of NIR spectral data, and was carried out to detect specific chemicals in aqueous solutions when concealed behind a layer of clothing [1]. As described in Chapter 3, concealment modifies the spectrum of a particular chemical when recorded at stand-off ranges of 3 m in a diffuse reflection experiment. Multivariate analysis of the collected spectra has been performed with neural network-based pattern recognition/classification to identify a particular chemical, followed by partial least squares regression (PLSR) to quantify the concentration in solution of the chemical identified. The use of neural networks in this application serves to overcome nonlinearities in the calibration/ training dataset, affording more robust modelling. The work has been shown to both allow detection of specific chemicals concealed behind a single intervening layer of fabric material, and to estimate the concentration of certain liquids. It has recently been published [2].

The study falls within the general area of security screening, where the development and use of scanning techniques that allows detection of concealed chemicals has been gaining increasing importance in recent years. In particular, the need to identify certain chemicals beneath a layer of clothing is of interest [3-6]. The application considered here concerns detection of specific chemicals in aqueous solution, accomplished using calibration models developed through statistical multivariate analysis of the relevant NIR spectra [7]. The technique can be applied, for instance, to the detection of liquid compounds such as hydrogen peroxide that could be used to constitute improvised explosive devices (IEDs) [8].

In the present study, the NIR spectra of several different chemicals have been collected, and used to demonstrate their detection, even in the presence of an intervening layer of clothing. This simulates such a chemical hidden within the clothing of, for example, a terrorist, and could lead in future to a personal screening system for the identification of specific liquids. It will be realized that this introduces a number of variables into the

problem; for this reason, a study has been undertaken into the use of different methods, whereby the identification of a particular chemical, and/or an estimate of its concentration, can be made.

The structure of the spectral data in the context of this study is such that the number of regressors p (the x-variables constituting NIR wavelengths over which the spectra are recorded) is significantly larger than the total number of observations n ($p \gg n$). This is accompanied by multi-collinearity and resultant redundancy, as well as lack of selectivity, amongst the p x-variables. This leads to non-productiveness of univariate data analysis (based on a single x-variable, or spectra recorded at a single wavelength) to accurately predict the presence of the specific chemical in a given concentration y. This necessitates prediction modelling through multivariate analysis [9]. Additionally, this approach affords the ability to carry out outlier detection, *i.e.* identification of samples whose characteristics show a significant departure from those of the majority data. In the context of this study, this involves samples with constituents such as clothing types or hidden chemicals that are different from those that the model has been calibrated to detect. As mentioned, univariate calibration precludes such outlier detection.

There is a wide range of calibration methods based on multivariate analysis of spectral data, where each approach offers certain advantages in specific calibration scenarios [10]. This necessitates careful consideration and choice of a calibration method that allows best use of the information contained in the relevant NIR spectral data while overcoming any shortcomings posed by the structure of the particular datasets.

In the following, the experimental arrangement used for the collection of NIR spectral data at stand-off distances of several meters will be reviewed, followed by some examples of the types of spectra that can be recorded using this technique. It will be demonstrated that the presence of a clothing layer between the NIR instrumentation and the chemical sample leads to complications that require the use of relevant calibration models. Following on from this, a discussion is presented about the choice of calibration techniques, data pre-processing, optimization of the relevant models, and validation of

their predictive ability using test data. This would allow the presence of a particular chemical to be identified.

Having shown that detection of particular chemicals is possible, further steps are required to estimate the concentration of a particular chemical in solution concealed behind clothing fabric. While this would be of secondary interest in a security scanning application, it was felt interesting to examine whether this could be achieved. As will be seen, the signal amplitude obtained in the presence of an intervening fabric layer is seen to diminish by a significant factor, making accurate concentration estimates difficult. However, an estimate within a certain range of values is still possible. More accurate concentration estimates could be obtained using the same data collection apparatus, but with the chemical sample removed from the clothing. This would represent a situation where the unwanted chemical has been identified in a security scan and removed from the person for further testing. Subsequent sections will thus describe results of concentration estimation both in the presence and absence of an intervening clothing layer.

4.2 Experimental arrangement

4.2.1 Optical bench

The optical bench arrangement used for the collection of NIR spectra has been described in detail in Chapter 3 (Section 3.3.1). As explained, the liquid chemicals were contained within $50 \times 50 \times 10$ mm^3 glass cells which exhibited negligible absorbance of NIR frequencies relative to the chemicals tested. The amplitude of the diffuse reflected signal from the liquid cells was augmented by placing a 10 mm thick PTFE block behind the cells to provide a uniform reflective surface [11]. With this arrangement in place, the absorbance spectra became saturated at wavelengths longer than 1,400 nm, which was expected in lieu of the first overtone of water at 1,450 nm as explained in Chapter 3 (Section 3.3.3.3). The upper wavelength limit was therefore set at 1,400 nm. Additionally, all spectral readings were taken with the light-collection optics placed at a stand-off distance of 3 m from the chemical/ fabric samples (an important consideration in any future security screening application). The integration time of the spectrometer was set at 400 ms, and an average of four spectra was taken in each case to reduce noise.

4.2.2 Chemical solutions and fabric samples

The chemical samples used to collect the calibration and test NIR spectra comprised binary solutions in distilled water of ethanol, hydrogen peroxide and ammonium nitrate, prepared in varying concentrations. While the latter two chemicals were chosen for their potential use in improvised explosives, the former was chosen as an example of a substance controlled by customs. Additionally, from the standpoint of chemical composition, these three solutions had all the main XH_n functional groups, namely C-H, O-H and N-H, represented between them. As absorption in the NIR band is dominated by these groups [12], it was felt interesting to include chemicals that encompassed these features. Note, however, that the study details results for hydrogen peroxide as an example of an important chemical in solution, whose concentration is an important variable in security screening.

The results reported herein were gathered with the range of chemical concentrations and concealing fabric samples shown in Table 4.1. In general, a sample of each chemical concentration listed was used to record four spectral readings, one in the presence of each of the four concealing fabrics. In the case of hydrogen peroxide, however, twice as many readings were taken as the chemical could only be obtained at concentrations up to 30% (the highest available commercially). This chemical was obtained from two different suppliers, and separate scans were carried out with samples from each supplier to check consistency of the measurement. Note that four repeat measurements were taken with every chemical cell/ fabric combination, and averaged to obtain the final spectra.

Table 4.1 – Sample constituents used to gather calibration and test data.

Type	Constituent	Concentration/ Fabric structure *(Figure 4.2)*	# of samples
Target chemical	Ethanol	10, 20, 30, 40, 50, 60, 70, 80, 90 and 100%	50
	Hydrogen Peroxide	3, 5, 10, 15, 20, 25 and 30%	64
	Ammonium Nitrate	0.3, 0.5, 0.7, 0.9, 1.1, 1.3 and 1.5 g/ml	28
Disruptive fabric layer	Polyester	Synthetic fibre; highly regular texture	One specimen of each material used to conceal the chemicals
	Cotton	Natural fibre; relatively regular and tightly woven	
	Acrylic	Synthetic fibre; regular, with large pores	
	Wool	Natural fibre; highly chaotic texture	

In an operational context, the concentrations of ammonium nitrate solution given in Table 4.1 were deemed relevant based on the strong oxidizing property of the

compound, which allows it to potentially react violently with organic and combustible materials as well as reducing agents to cause fire and explosion [13]. The risk could not be disregarded even in its most dilute form, as a sufficiently large explosive booster would magnify its sensitivity to detonation, especially if coupled with heat/ shock, or evaporated to near-dryness [14]. Similarly, hydrogen peroxide as a strong oxidant could prove extremely dangerous especially in high concentration [15], reacting violently with reducing agents. However, its use in concentrations as low as 6% to synthesize peroxide-based explosives [16] such as hexamethylene triperoxide diamine (HMTD) rendered detection at all concentrations desirable. Finally, binary solutions of ethanol in 10-100% concentration were in conformity with the values encountered in practice. Note that the samples tested were restricted in this study to those with security or border control implications; other liquids (such as soft drinks for example) were not considered.

The particular fabric specimens used here were chosen to represent a selection of synthetic (polyester and acrylic) and natural (cotton and wool) materials commonly used in clothing. In Chapter 2 (Section 2.3), the optical transmission and scattering properties of such fabric materials were investigated in detail to establish that the overall magnitude of NIR through-transmitted or diffuse-reflected energy from a sample was the function of its porosity and thickness. However, as these latter properties were not directly linked with the material of the fabric – 100% cotton fabrics, for instance, incorporate a wide range of thicknesses and porosities – they were deemed to exert influence by restricting the number of incident photons passing through the fabric unimpeded. Of somewhat greater relevance to this application, therefore, was the observation detailed in Chapter 3 (Section 3.4.1) that the fabrics produced NIR absorption spectra that were characteristic of the particular fabric material [17]. This latter phenomenon has been reviewed here using the spectra of the four specimens used in this study. These spectra, measured with reference to the source intensity signal reflected by the PTFE block, are shown in Figure 4.1.

The spectral features of cotton (absorption peaks at 1,210, 1,490 and 1,935 nm), and polyester (peaks at 1,135, 1,389 and 1,665 nm) are similar to the results reported in literature [18]. Moreover, the spectra of polyester and acrylic have very similar features,

with the latter shifted slightly towards longer wavelengths. This might be a consequence of both these being synthetic materials. Finally, wool seems to have very distinct spectral features at lower wavelengths, where a high absorption peak in the 860-1,000 nm range sets it apart from the relatively flatter profiles of all other specimens. As high absorption below 1,400 nm was understood to make detection of chemicals across a layer of wool more challenging, this specimen was chosen to test the robustness of the relevant calibration models.
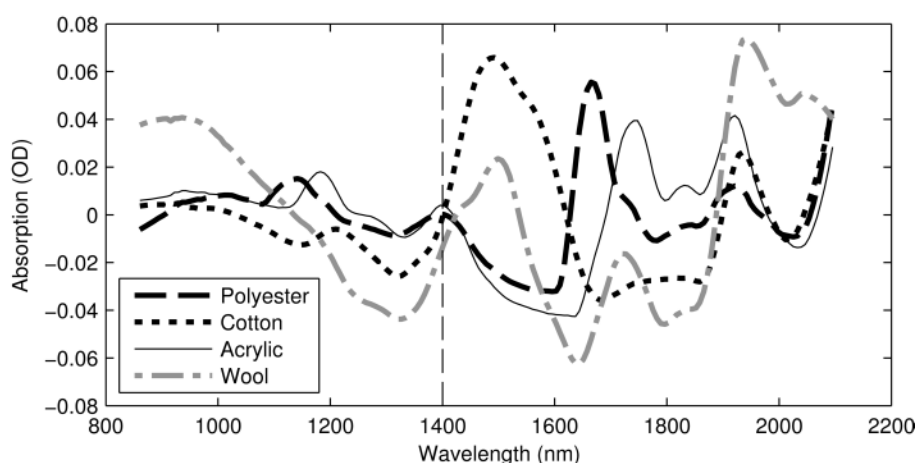
Figure 4.1 – Absorbance spectra (with reference to incident source intensity)
of the four fabric specimens used to conceal the chemical samples.

The surface structure and weaving pattern of fabric samples used is shown in Figure 4.2.
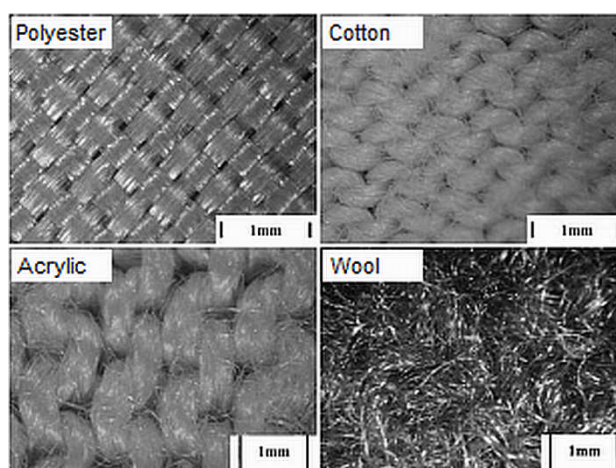
Figure 4.2 – Fabric samples as seen through optical microscope.

These images show polyester with the most regular surface texture, while acrylic is seen to have relatively large pores. These characteristics are deemed to aid in higher through-

transmission as compared to the chaotic texture of wool and the tighter weave of cotton. As higher overall through-transmission would serve to reduce the amplitude of all spectral features seen in Figure 4.1, this might be a factor influencing the relatively lower amplitudes of absorption peaks in the spectra of polyester and acrylic.

4.2.3 Reference level for absorbance spectra

Target spectra were obtained with single chemical cells either placed behind one of the fabric layers or kept unconcealed. All absorbance spectra used for subsequent calibration modelling/ testing were measured with reference to the spectrum of water:

$$A = -\log_{10} \frac{I_S - I_D}{I_R - I_D} \qquad (4.1)$$

where A is the absorbance in optical density units, while I_S, I_D and I_R are respectively the optical intensity levels measured with the sample, without the source of illumination (dark spectrum/ noise floor) and with the reference sample (in this case, distilled water plus any intervening fabric layer). Thus, the baseline is defined as the case where $I_S = I_R$ (or $A = 0$). Taking the spectrum of water as the reference level in this way enables the focus of subsequent calibration steps to be separated from the influence of the spectrum of water; otherwise, characteristic peaks of the latter tend to overshadow the spectral features of the particular analytes. Accordingly, while the pertinent chemical species represent targets of interest to be detected through calibration modelling, the intervening fabric layers essentially pose as disruptive scatterers whose influence must be overcome to enable such modelling.

In order to illustrate the extent to which the spectra are influenced and modified by intervening fabric layers, the spectra of water obtained before and after the liquid cell is concealed behind a layer of fabric (cotton) are shown in Figure 4.3(a) and (b) respectively. In the latter case, the spectral content is seen to be radically different to that of water, with the absorption peaks of cotton (shown in Figure 4.3(c) and detailed in Figure 4.1) clearly dominant. This shows that spectra recorded with an intervening fabric layer are dominated by the reflection from the surface of the fabric layer. By taking the spectrum of the fabric as baseline reference I_R in (4.1), we obtain the spectrum shown in Figure 4.3(d) which, as expected, is a close match to that of water, albeit with a diminished amplitude (reduced 97% from Figure 4.3(a) in this case). This

highlights the need to develop robust calibration models if any of the chosen liquids is to be identified when concealed behind clothing.

4.3 Identifying chemicals: Classification and quantification

Chemical identification was performed by processing recorded spectra in Matlab® as follows: First, a classification process was used to determine whether the sample contained a chemical of interest. This was accomplished through a pattern recognition/ classification step, using a feed-forward/ back-propagation neural network (NN). Secondly, in case of an affirmative outcome from this procedure, a second calibration model was used to quantitatively measure the concentration of the relevant chemical in aqueous solution. This was accomplished through a model developed using PLS regression. These two aspects are now considered separately.
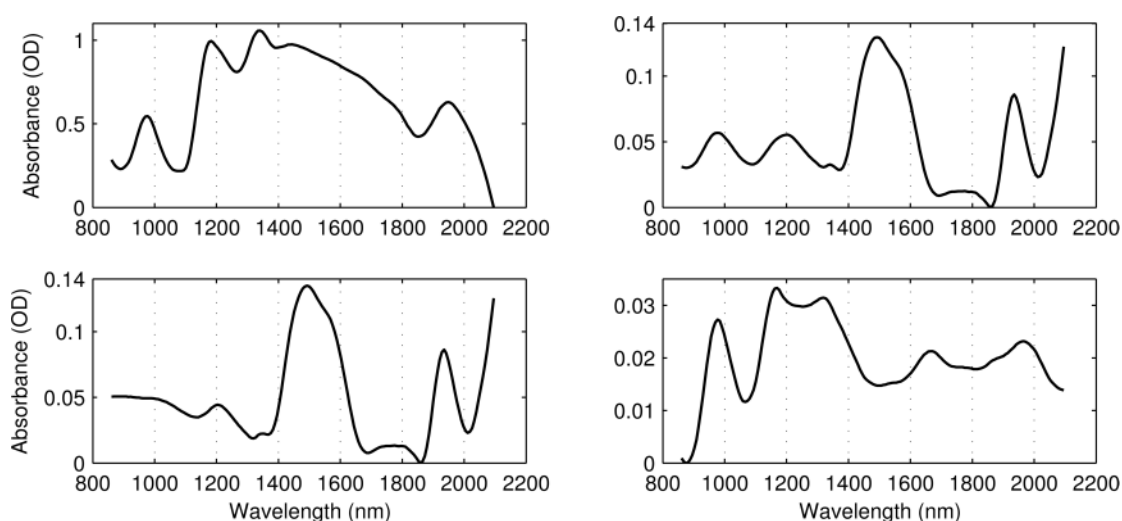
Figure 4.3 – Effects of intervening cotton fabric layer on the spectrum of a liquid. Shown are spectra recorded for (a) water only, (b) water concealed behind a fabric layer (cotton), (c) fabric sample placed on its own, and (d) water concealed behind a fabric layer, with the fabric material taken as reference.

4.3.1 Classification using NN

4.3.1.1 Choice of NN

The choice of NN as the calibration technique was based on the nonlinear characteristic of the sample data given in Table 4.1, as well as the capability of NNs to overcome some of the inherent limitations of competing parametric and non-parametric classification methods such as Soft Independent Modelling of Class Analogy (SIMCA) and K-nearest-neighbours (KNN) respectively [19, 20]. Additionally, the versatility of NNs in modelling data with unknown/ nonlinear functional relationships [21-25] as well

as linear data [6] was deemed to be well-suited to this case. The choice of NNs as a primary calibration technique in all cases has been advocated in literature [10], provided test samples remain within the calibration space and a sufficiently large number of calibration samples is available. In the context of this study, however, test samples were understood to possibly include outliers not covered by the calibration domain defined by the available calibration data: This was addressed by subsequent PLSR-based outlier detection to increase confidence in the initial NN-based detection. Additionally, the relative paucity of calibration samples was addressed by adopting a particular NN variant as explained below.

The usual technique used to control NN training in a way that ensures the trained network is capable of generalization and is not over-fitted on the training data, involves splitting the training dataset to designate part of it as a validation set, and carrying out training epochs with the leftover training data. At the end of each epoch, the NN is simulated with the validation set to monitor network error. Training is continued while the magnitude of this validation error registers a decrease after each epoch, and ceased at the onset of overfitting signified by an increase in validation error.

However, in lieu of the relatively small training dataset in this study – out of a total of 142 samples detailed in Table 4.1, around half were included in the training dataset, and the remaining half were reserved as an independent test set – it was felt desirable to train the NN in a manner that precluded this need to split the training data, while adequate safeguards were put in place through alternate means to prevent overfitting and ensure requisite generalization capability of the trained network. This was accomplished by training the NN with a Bayesian learning algorithm [26] used in conjunction with Levenberg-Marquardt optimization [27]. Here, the modified performance function P which was minimized through successive training epochs, was a linear combination of MSE and MSW, the mean-squared errors and mean-squared weights of the network respectively:

$$P = \alpha MSE + (1 - \alpha)MSW \tag{4.2}$$

where α was the performance ratio explained below, and

$$MSE = \frac{1}{m}\sum_{i=1}^{m} e_i^2 \tag{4.3}$$

Chapter 4: Multivariate calibration of spectroscopic data

$$MSW = \frac{1}{n}\sum_{j=1}^{n} w_j^2 \qquad\qquad (4.4)$$

where m was the number of samples in the training set, e_i the network error *i.e.* difference between the true (desired) and actual network response to ith training sample, n the number of synaptic weights and biases in the hidden and output layers of the network, and w_j the jth weight/ bias. Both *MSE* and *MSW* were evaluated at the end of each training epoch, and the network was error-adjusted accordingly. The performance ratio α in (4.2) was determined statistically based on the variance of network weights and biases, which were treated as random variables with specific distributions.

As shown above, the performance function P was designed to reduce network weights/ biases in addition to network errors as training progressed, which provided for smoother network convergence while preventing overfitting. Additionally, a pre-processing step was used as explained below to compress input spectra to their first few principal components (PCs) so as to restrict the size of the hidden layer to the smallest practicable level. This served to reduce the effective number of network parameters used by the trained network to a minimum, thereby limiting the relevant degrees of freedom as a further measure to prevent overfitting and enhance generalization. As mentioned above, these measures were felt necessary in view of the relatively small training dataset. With their inclusion in the training algorithm, additional measures such as the optimal brain surgeon (OBS) algorithm [28] were deemed superfluous for this application.

4.3.1.2 Data pre-processing

The first pre-processing step involved filtering the spectra with a Savitzky-Golay finite impulse response (FIR) filter [29], which comprised local 2nd degree polynomial regression on a moving block of 15 values to determine the smoothed value at each point of the spectrum. A number of further processing steps were considered [30-32] to pre-process the training and test data, and the following were adopted based on direct relevance and performance.

First, the standard normal variate of individual spectra was taken [33], which involved mean-centring each observation thus eliminating baseline shift, followed by normalizing the observations so the standard deviation of each was set to 1, thus cancelling spectral drift. Although the latter resulted in loss of amplitude information in

the absorbance spectra, this was of little consequence as the objective of the neural processing step was based solely around classifying the analyte as a member of one of the target classes. Quantification of analyte concentrations using the amplitude information involved further steps.

Next, the number of nodes in the input, and consequently hidden, layer of the NN was minimized by reducing the dimensions of the input spectra [34] from the original 80 wavelength channels to their first 10 PC scores [35]. This was necessitated by the need to optimize NN topology by cutting down the degrees of freedom available to the network to guard against the problem getting over-determined [36]. Subsequent to completion of training, test spectra were projected onto the pertinent PC space using loadings that had been obtained with the calibration samples.

4.3.1.3 Training & testing

A plot of the scores of first three PCs of the dataset (Table 4.1) is given in Figure 4.4. This shows the clustering effect of the different chemical bonding (mainly the N-H, O-H and C-H bonds) in constituent chemicals that gives rise to characteristic spectral features [37].
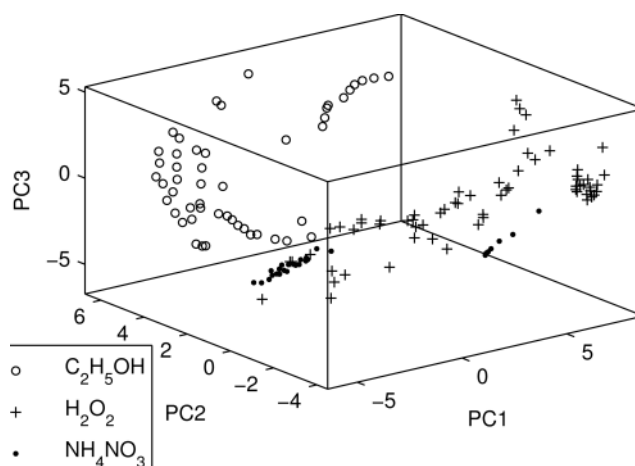
Figure 4.4 – Scores of the first three principal components of the data,
which exhibits clustering.

Of the samples shown in Figure 4.4, around half (72 of the total 142) were used for training the NN while the remaining half were used as an independent test set. In order to split the data between training and test sets, the implications of the relevant ASTM guidelines [38] were considered, and different data splitting algorithms such as the

---

Chapter 4: Multivariate calibration of spectroscopic data

duplex [39] and KS [40] algorithms were tried; however, this approach did not make adequate allowance for testing the model's ability to extrapolate training data [41] to account for new test spectra collected, for instance, with the chemicals concealed behind a fabric sample not used in training. Therefore, the samples were principally divided to include the spectra collected with two types of fabrics each in the training and test sets. However, a few sample spectra of hydrogen peroxide (uncovered and with polyester layer), collected in addition to the training data, were also included in the test data set. The resultant makeup of the two sets is shown in Table 4.2, with sample distribution in terms of the first three PC scores shown in Figure 4.5.

Table 4.2 – Datasets used to train and test NN to classify chemical constituents.

Data type	Chemical	Concealing layer	# samples
Training data	Ethanol (10% – 100% solutions)	Uncovered	10
		Polyester	10
		Cotton	10
	Hydrogen Peroxide (3% - 30% solutions)	Uncovered	7
		Polyester	7
		Cotton	7
	Ammonium Nitrate (0.3 – 1.5 g/ml solutions)	Uncovered	7
		Polyester	7
		Cotton	7
Test data	Ethanol (10% – 100% solutions)	Acrylic	10
		Wool	10
	Hydrogen Peroxide (3% - 30% solutions)	Uncovered	13
		Polyester	9
		Acrylic	14
		Wool	7
	Ammonium Nitrate (0.3 – 1.5 g/ml solutions)	Acrylic	7

The hidden and output layers were assigned 2 and 3 nodes respectively, with hyperbolic tangent sigmoid transfer functions to adapt to the non-linear data [25]. Classification was implemented using three 3-element binary target vectors, where a single element of each vector was set to 1 to signify one of the three possible chemical solutions. Starting from a number of initial conditions, the network was seen to converge onto constant values of MSE, MSW and effective number of parameters after 20-25 training epochs, at which stage the training was stopped. Moreover, the effective number of parameters in the trained network was observed to remain approximately constant (around 31)

when the number of hidden nodes was increased, which confirmed proper convergence of the *MSW* parameter at the end of training.
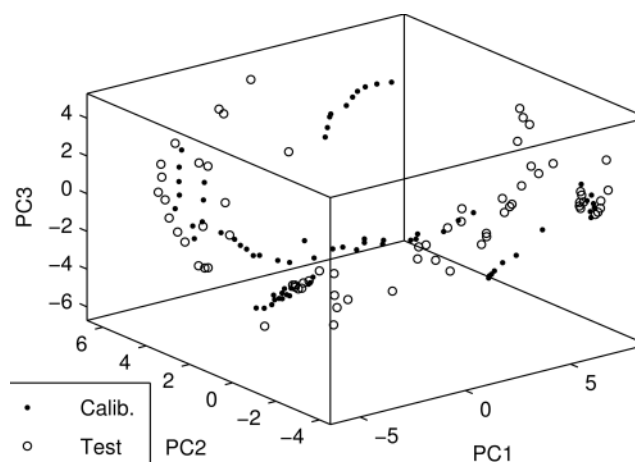
Figure 4.5 – First three PC scores showing the distribution of training and test sets.

4.3.1.4 Results

The classification of test data carried out by the trained NN is shown in Figure 4.6. The majority of samples were classified correctly, and this included all of the samples at higher concentrations. Not surprisingly, the task was more difficult at lower concentrations. As seen, out of the 70 test samples given in Table 4.2, six were misclassified. Four of these were samples of hydrogen peroxide concealed behind acrylic (3% – 15% concentration), while two were hydrogen peroxide concealed behind wool (5% and 10% concentration). The relatively low concentrations of these samples meant that the pertinent absorption spectra had few particularly distinct features with reference to water, which rendered their categorization less definitive than higher concentration samples.

As seen, ethanol and ammonium nitrate samples of all concentrations, concealed behind fabrics not included in the training data, were correctly classified. The characteristic N-H and C-H bonds in these samples allowed relevant absorption spectra to retain a relatively higher proportion of characteristic features to enable recognition even at lower concentrations.

Based on these results, a safe detection limit for hydrogen peroxide concealed behind a fabric layer could be set at 15% concentration, while the limit in the case of ammonium nitrate and ethanol would be below the lowest concentrations used here, *i.e.* 10%

ethanol and 0.3 g/ml ammonium nitrate solution. No variation in these detection limits is expected within the purview of the current experimental arrangement, as simulating the trained network with spectra from fresh samples in previously used concentrations elicited the same network response in each case.
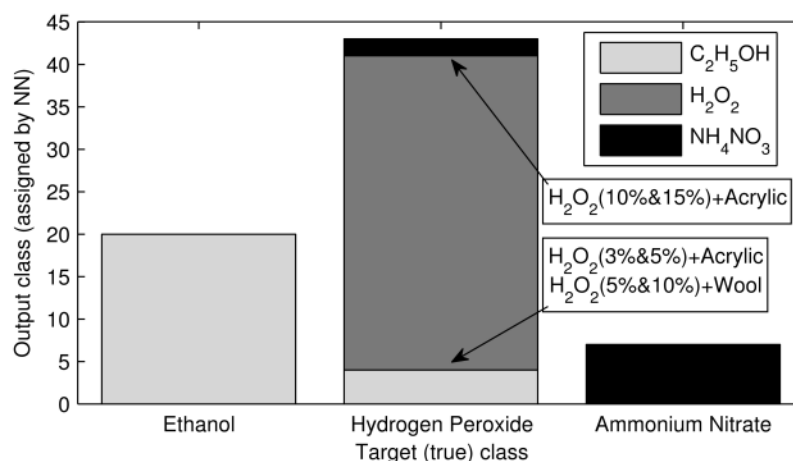
Figure 4.6 – Classification of test data by NN trained with Bayesian regularization algorithm.

4.3.2 Quantifying concentration using PLS regression

With the chemical species identified, a second step was implemented to quantify the concentration of the chemical samples, using a calibration model developed with full-spectrum PLS regression.

Note that hydrogen peroxide solutions are of potentially greater relevance to security screening in terms of concentration than substances such as ethanol. Thus, hydrogen peroxide data were used to develop the PLSR models illustrated here. They comprised absorbance spectra of seven hydrogen peroxide samples with concentrations ranging from 3% to 30%. While these samples met the afore-mentioned calibration guidelines [38] to encompass the extremes of available data and uniformly cover the interlaying test domain, a greater number of calibration samples would be required to produce a more robust model. This set, however, produced an adequately descriptive model to illustrate the underlying principle.

4.3.2.1 Data pre-processing

As before, the first preprocessing step involved filtering the spectra with a Savitzky-Golay FIR smoothing filter to remove high-frequency noise. An offset-correction was then performed on the filtered data. This involved calculating the average of the last 10

x-variables (wavelength channels) of each calibration object, and subtracting that average from each element of the corresponding object. This served to eliminate the baseline shift while preserving the relative amplitudes of the absorbance spectra. The preprocessed calibration spectra of hydrogen peroxide samples without any fabric layer are shown in Figure 4.7. It may be noted that while these spectra would yield well to univariate analysis, the multivariate approach was nevertheless preferred in order to develop a robust modelling algorithm applicable in less favourable situations such as, for instance, cases where ambient noise affected a range of wavelength channels to make univariate analysis less productive.
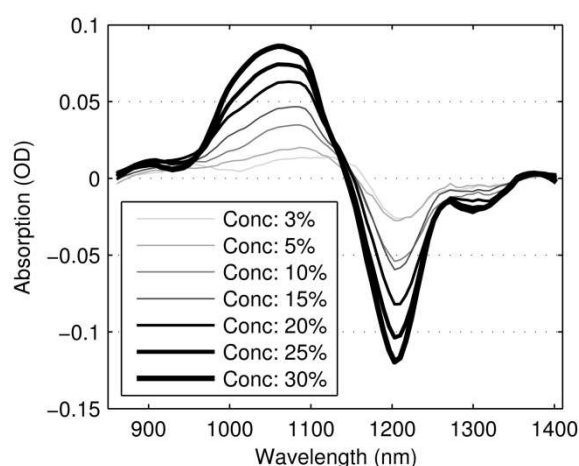
Figure 4.7 – Pre-processed spectra of hydrogen peroxide with reference to water, used to calibrate the PLSR model; 80 wavelength channels between 850-1,400nm wavelength range.

4.3.2.2 Model validation

Model validation was next performed to determine the optimal complexity of the calibration model *i.e.* the number of PLS regression factors to include in the model in order to cover as much variance in the calibration data as possible while preventing overfitting. This was implemented with a two-pronged approach:

The first measure of the optimal complexity was based on the global minimum of mean-squared error of cross-validation (MSECV) obtained with the calibration data when model complexity was varied between 1 and 15 PLS factors. At each of these complexity levels, the MSECV was calculated by leaving out each of the seven calibration samples in turn, deriving the calibration model from the remaining six samples, and testing it with the sample that was left out to record the prediction error as the difference between the actual concentration of the test sample and the one predicted

by the model. The resulting seven prediction error values were then processed to determine M_j, the MSECV with model complexity of j PLS factors ($1 \leq j \leq 15$):

$$M_j = \frac{1}{n}\sum_{i=1}^{n}\left(y_i - \hat{y}_{ij}\right)^2 \qquad (4.5)$$

where n is the number of calibration samples (7 in this case), y_i the actual or true concentration of ith calibration sample, and $\hat{y}_{ij}$ the concentration of the ith sample predicted by a calibration model derived from the other six samples based on j PLS factors. The results are plotted in Figure 4.8 alongside mean-squared error of estimation (MSEE), and listed in Table 4.3. MSEE for a particular complexity level was calculated using prediction errors of calibration data with a calibration model derived from the entire calibration dataset. As seen, while MSEE continued to decrease with increasing model complexity, the smallest value of MSECV was obtained with 5 PLS factors. This was therefore taken as an initial estimate of optimal complexity.
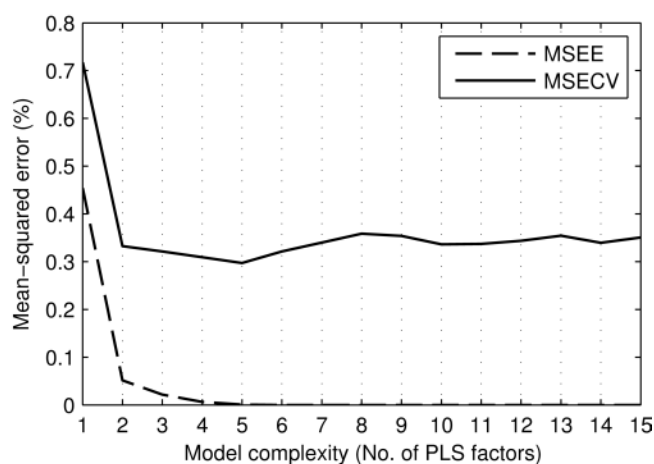
Figure 4.8 – PLSR model validation: MSEE and MSECV as functions of model complexity (number of PLS factors). Global minimum of MSECV (5 factors) was taken as an initial estimate of optimal model complexity.

A second statistical measure was next adopted in the form of a randomization t-test [42] as a safeguard against overfitting. This method tests the predictive accuracy of two competing calibration models by assuming that they are equally accurate, and then tests this hypothesis statistically to form a quantitative measure of comparison called the significance level. In this case, the initial estimate *i.e.* the 5-factor model was used as reference, and each of the other models was sequentially compared with it. The resulting significance level values are shown in Table 4.3. As seen, the local maximum of these values for models with fewer factors than the first estimate of 5 was obtained

with the 2-factor model (which in this case represented the global maximum as well). As this demonstrated that the predictive ability of the 2-factor model was closest in strength to the initial estimate while providing a more parsimonious solution to the problem, this model was adopted as the optimal one for processing the spectra to make requisite concentration estimations.

Table 4.3 – Determination of optimal model complexity: Global minimum of MSECV i.e. 5-factor model was taken as the first estimate, followed by local minimum of significance level (randomization t-test) for a more parsimonious solution.
The 2-factor model was thus chosen as optimal.

	Model complexity (Number of PLS factors)							
	1	2	3	4	5	6	7	8
MSECV	0.72	0.33	0.32	0.31	0.30	0.32	0.34	0.36
Significance Level	0.215	0.91	0.555	0.645	–	0.200	0.130	0.280
	9	10	11	12	13	14	15	
MSECV	0.35	0.34	0.34	0.34	0.35	0.34	0.35	
Significance Level	0.360	0.365	0.265	0.175	0.205	0.405	0.380	

4.3.2.3 Tests with chemicals without fabric layer

To simplify the data, so as to provide spectra unmodified by the clothing layer, this method was first tested with the clothing layer removed from the problem. The approach then approximated to a linear calibration problem, so that the standard bilinear regression approach could be used, whereby the model developed to predict the concentration y was based on the first few PLS regression factors covering all essential variance in the x variables (NIR spectra) while, as opposed to principal component regression (PCR), minimizing the impact of any significant variations in x which were uncorrelated with y. Note that Section 4.3.2.4 will extend the approach to liquids hidden behind clothing layers (the application area of interest here).

The optimal 2-factor model was tested with fresh solutions of hydrogen peroxide to verify the reliability of predictions, as well as outlying solutions (containing ammonium nitrate and ethanol) to test the model's resilience in the presence of outliers. The makeup of the calibration and test datasets is given in Table 4.4. It may be noted that while ethanol and ammonium nitrate solutions would ideally be identified as outliers during the initial NN-based classification stage, further outlier testing was considered

here to increase confidence in the results in view of the reasons outlined in Section 4.3.1.1.

Table 4.4: List of chemical samples used to collect spectral data to calibrate and test 2-factor PLS calibration model for quantifying chemical concentration.

Type of data	Constituent	# of samples	Concentration
Calibration	Hydrogen Peroxide	07	3, 5, 10, 15, 20, 25, 30%
Test	Ethanol	10	10, 20, 30, 40, 50, 60, 70, 80, 90, 100%
Test	Ammonium Nitrate	07	0.3, 0.5, 0.7, 0.9, 1.1, 1.3, 1.5 g/ml
Test	Hydrogen Peroxide	13	3, 5, 10(x3), 15, 20(x3), 25, 30(x3)%

The prediction results obtained with the 2-factor PLS model are shown in Figure 4.9.
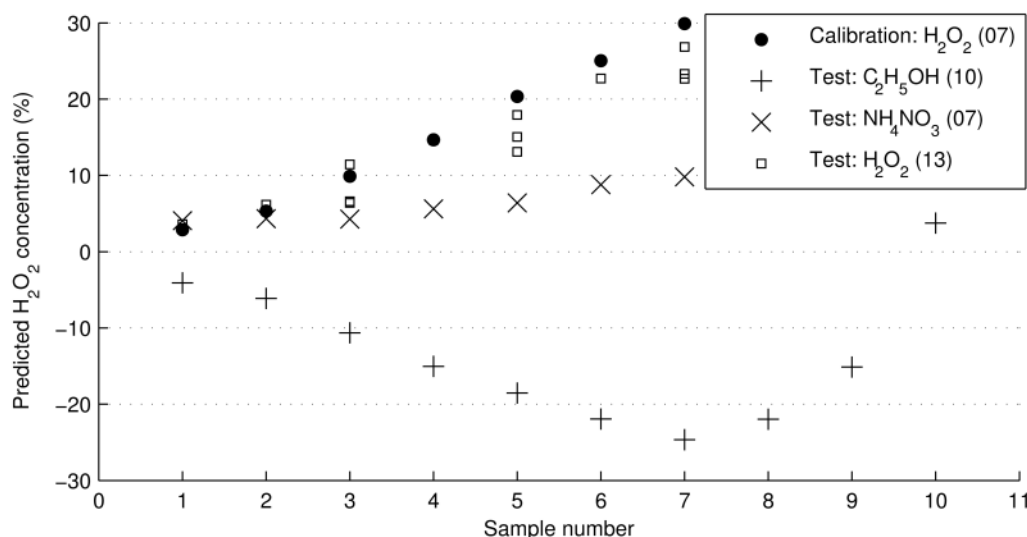
Figure 4.9 – Concentration of hydrogen peroxide predicted by 2-factor PLS calibration model. Test data comprised samples of hydrogen peroxide and outlying chemicals including ethanol and ammonium nitrate. Note that sample numbers (x-axis) reflect sample concentrations in the sequence given in Table 4.4.

The model predicted the concentration of hydrogen peroxide test samples with an RMS error of prediction of ±4.1% (derived from the differences between the true and predicted concentration values), and clearly differentiated these from the test results for ammonium nitrate and ethanol. The values shown for ethanol samples are negative, although some sensitivity to ammonium nitrate was noted, especially at low concentration values below 10%. While this value effectively sets the low threshold limit in this case on the concentration of hydrogen peroxide that could be detected reliably in the presence of these chemicals, an additional outlier detection mechanism

explained below enables separation of hydrogen peroxide at all concentrations from such outliers.

The algorithm used to systematically evaluate all test spectra to detect outliers involved two further steps [9, 43]: First, the residual variance in the spectra of the samples was tested after the calibration model had been applied. A threshold was set, based on the average residual variance in the calibration data, and a test sample was deemed to be an outlier if its residual variance exceeds this threshold. Second, the leverage of the test samples was tested. The leverage of a sample is based on the position of its x-variables relative to those of the other samples. As above, a threshold was set based on the average leverage of the calibration data, and a test sample was declared an outlier if its leverage exceeding this threshold.

Figure 4.10 shows a plot of residual variance against leverage (termed prediction influence plot) for the data in Table 4.4. As seen, threshold levels of 100 times average residual variance and 20 times average leverage of calibration data excluded all but one of the outlying ammonium nitrate and ethanol test samples. This single outlier residing within the acceptance limits was ethanol in 10% concentration, and illustrated the necessary compromise between probabilities of detection and false alarm.
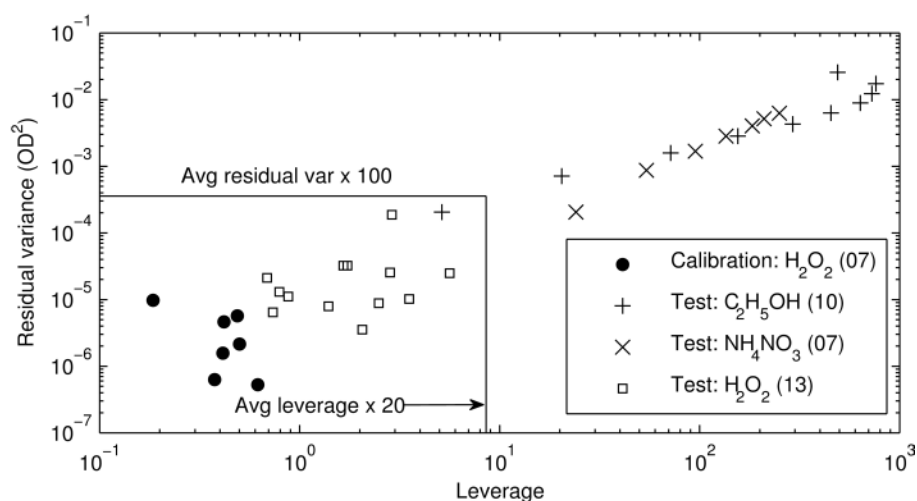
Figure 4.10 – Prediction influence plot using 2-factor PLSR calibration model for hydrogen peroxide. Residual spectral variance vs. leverage for 7 calibration objects and 30 test objects.

4.3.2.4 Tests with chemicals hidden behind clothing

The above has demonstrated the use of a PLSR model to quantify liquid concentrations in binary aqueous solution, when the liquid cell is directly exposed to the NIR signal. However, a real personal security screening application would ideally require such quantification to take place when the chemical is hidden behind a layer of clothing. Figure 4.3 indicated that modifications to the recorded spectra of liquid samples under test would be expected when a clothing layer was present. In this case, the spectra were seen to be dominated by diffuse-reflected signal from the surface of the fabric. It would be expected that this would make the estimation of liquid concentration more difficult, even with the spectrum of the fabric layer used as reference.

Tests were thus conducted on chemicals hidden behind clothing, and the same procedure as above was followed. A sample of polyester was used as the concealing fabric layer, and the calibration model was constructed with absorbance spectra of hydrogen peroxide measured with reference to water and the fabric layer. In this case, it was found that the optimum calibration model was composed of 4 PLS factors. The model was tested with fresh spectra of the three chemicals hidden behind the same fabric layer. The composition of calibration and test datasets is given in Table 4.5.

Table 4.5: Samples of chemicals hidden behind a layer of polyester fabric, used for spectral analysis to calibrate and test 4-factor PLS calibration model for quantifying chemical concentration.

Type of data	Constituent	# of samples	Concentration
Calibration	Hydrogen Peroxide	07	3, 5, 10, 15, 20, 25, 30%
Test	Ethanol	10	10, 20, 30, 40, 50, 60, 70, 80, 90, 100%
Test	Ammonium Nitrate	07	0.3, 0.5, 0.7, 0.9, 1.1, 1.3, 1.5 g/ml
Test	Hydrogen Peroxide	09	10(x3), 20(x3), 30(x3)%

The concentration estimates provided by the model are given in Figure 4.11. The RMS error of prediction for hydrogen peroxide test samples was estimated to be ±5.1% in this case. This was deemed to be acceptable, if the approach is to provide an estimate of concentration in a security screening application. More accurate values could subsequently be obtained by off-line testing, if an initial reading is deemed to be worthy of further investigation. Again, concentrations above 10% show good discrimination from the results with outlying ammonium nitrate and ethanol test samples.

An interesting point to note is that for hydrogen peroxide test samples, the spread of points is lesser for a given concentration in the presence of a clothing layer (Figure 4.11) than without (Figure 4.9). This is a consequence of the less accurate results obtained with *all* samples when clothing is present. While this may seem counter-intuitive, the result is that the values tend to cluster together, as they have the same error for a given concentration. Thus, the variation in predicted value is less, but the RMS error of prediction is greater.
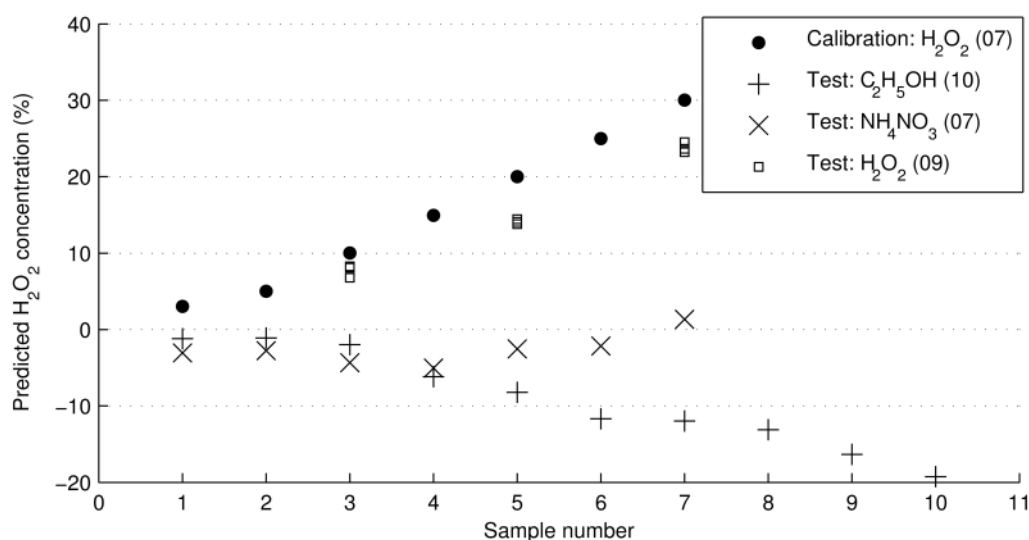
Figure 4.11 – Concentration of hydrogen peroxide predicted by a 4-factor PLS calibration model, in samples hidden behind a layer of polyester fabric. Test data comprised samples of hydrogen peroxide and outlying chemicals including ethanol and ammonium nitrate. Note that sample numbers (x-axis) reflect sample concentrations in the sequence given in Table 4.5.

Further tests were performed on the spectra for outlier detection. The relevant prediction influence plot is shown in Figure 4.12. As seen, the spectra did not to yield as well to the tests in this case, with the leverage of a number of outlying test samples falling well below that of hydrogen peroxide test samples. This was deemed to result from a lack of clear distinctive features in the spectra of different chemicals collected in the presence of the dominant intervening fabric layer.

An interesting feature, however, is the tightly clustered layout of the results for hydrogen peroxide test samples. If such features are observed to persist in repeat measurements, they might allow subsequent analyses to be drawn using measures such as Mahalanobis distance amongst plotted results to deduce with a given degree of confidence the underlying nature (outlier or otherwise) of the samples.

Chapter 4: Multivariate calibration of spectroscopic data
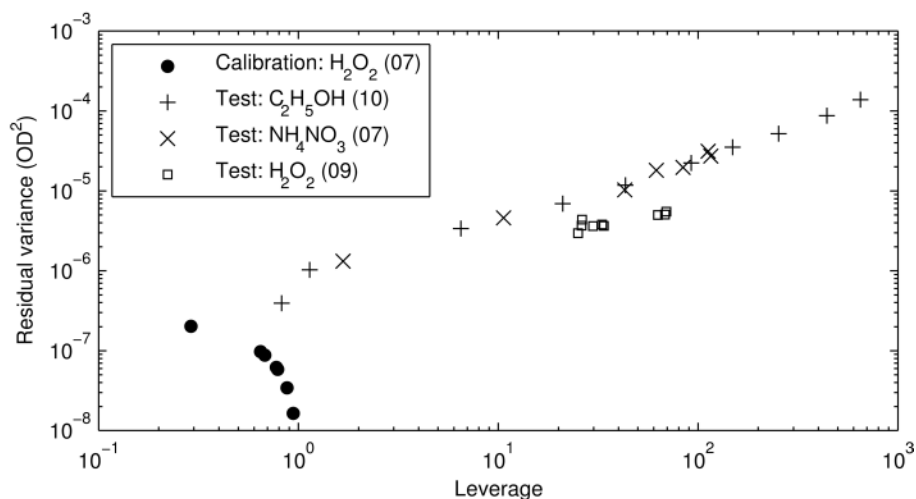
Figure 4.12 – Prediction influence plot using 4-factor PLSR calibration model for hydrogen peroxide, with samples concealed behind a fabric (polyester) layer. Residual spectral variance vs. leverage for 7 calibration objects and 26 test objects

4.4 Conclusions

This work sought to establish a basis for using NIR spectroscopy to identify certain chemicals hidden behind a layer of clothing. This was followed by quantifying chemical concentration both with and without the clothing layer in place. The work has demonstrated the feasibility of the technique, which would help to enable its eventual deployment in practical security screening applications. While the fabrics did make the detection process more challenging, as shown in the neural network (NN) detection results in Figure 4.6, only 6 out of 70 test samples were wrongly classified. In general, all hydrogen peroxide samples above 15% concentration, and all ethanol and ammonium nitrate samples were correctly detected by the NN approach. It may be noted that these results were obtained when 68% (48 out of 70) test samples contained fabrics that the NN had not been trained on; they were thus real test results from unknown samples and demonstrated the ability of the NN to extrapolate from the calibration space.

Estimation of concentration also showed some interesting results. The method was first tried on sample with no clothing present, and subsequently on samples hidden behind a single fabric (polyester) layer. It was found that concentrations above 10% hydrogen peroxide were needed to determine the concentration within an error of approximately ±5% unambiguously. This may seem a large error, but in fact is acceptable in a screening situation, where higher concentrations are generally of more concern.

Chapter 4: Multivariate calibration of spectroscopic data

Additionally, outlier detection based on prediction influence plot allowed separation of hydrogen peroxide samples at concentrations as low as 3% in the absence of clothing layer.

Throughout this work, the same flat-surfaced glass cells were used to contain the chemicals, with the optical illumination being similar in all cases. In practice, this will not be the case in a real security screening situation; however, keeping these parameters constant allowed the performance to be established in the laboratory under controlled conditions, without introducing too many variables. Real use would require more work on variability in the illumination and different containers. Further work would also need to be done to establish the baseline spectra of clothing in a real test, when the chemicals are concealed by fabric layers. This is recommended for further research.

The primary objective in this work has been to detect the presence of a liquid chemical; however, as concentration estimates have been made using the same equipment and set of readings as used for detection, this could be used as an add-on module in a practical application to obtain an approximate estimate of concentration. This would then need to be followed by more detailed testing off-line.

It is also appreciated that only binary solutions in glass cells have been used in this study, and that mixtures of compounds in containers such as PET bottles, and other substances commonly encountered in practical screening applications such as soft drinks, should be tested as well. Additionally, it is felt that signal enhancement techniques such as lock-in amplification of the spectral data could be used to allow operation in noisy environments. As this latter aspect is deemed to be especially important in establishing the feasibility of the technique in an operational context, it has been the focus of recent research as explained in Chapter 5.

4.5 References

[1] A. Saleem, C. Canal, D. A. Hutchins and R. J. Green, "NIR spectroscopy with multivariate calibration and lock-in amplification to detect chemicals concealed behind fabrics," in *Chemical, Biological, Radiological, Nuclear, and Explosives (CBRNE)*

Sensing XII, part of SPIE Defense, Security, and Sensing, Orlando, Florida, USA, 2011, pp. 8018 I 1-18.

[2] A. Saleem, C. Canal, D. A. Hutchins, L. A. J. Davis and R. J. Green, "Techniques for quantifying chemicals concealed behind clothing using near infrared spectroscopy," *Anal. Methods, DOI:10.1039/C1AY05301A,* 2011.

[3] G. M. Stone, "Application and limitations of advanced technologies in explosives detection," in *Proceedings of the 1990 International Carnahan Conference on Security Technology: Crime Countermeasures, October 10, 1990 - October 12, 1990*, Lexington, KY, USA, 1990, pp. 81-87.

[4] S. Singh and M. Singh, "Explosives detection systems (EDS) for aviation security," *Signal Processing,* vol. 83, pp. 31-55, 2003.

[5] S. Kumar, W. C. McMichael, Y. W. Kim, A. G. Sheldon, E. E. Magnuson, L. Ficke, T. K. Chhoa, C. R. Moeller, G. A. Barrall, L. J. Burnett, P. V. Czipott, J. S. Pence and D. C. Skvoretz, "Screening sealed bottles for liquid explosives," in *Security Systems and Nonlethal Technologies for Law Enforcement, November 19, 1996 - November 19, 1996*, Boston, MA, United states, 1997, pp. 126-137.

[6] L. J. Burnett, "Liquid explosives detection," *Proceedings of SPIE - The International Society for Optical Engineering,* vol. 2092, pp. 208-217, 1994.

[7] W. F. McClue, "Near-infrared spectroscopy. The giant is running strong," *Analytical Chemistry,* vol. 66, pp. 43A-53A, 1994.

[8] H. Itozaki and Y. Yamauchi, "Liquid explosive detection from outside of the bottle by IR," in *Proceedings of SPIE - The International Society for Optical Engineering - Infrared Technology and Applications XXXV, April 13, 2009 - April 17, 2009*, Orlando, FL, United states, 2009.

[9] H. Martens and T. Næs, *Multivariate calibration*. Chichester [England]; New York: Wiley, 1989.

[10] V. Centner, J. Verdu-Andres, B. Walczak, D. Jouan-Rimbaud, F. Despagne, L. Pasti, R. Poppi, D. L. Massart and O. E. De Noord, "Comparison of multivariate calibration techniques applied to experimental NIR data sets," *Applied Spectroscopy,* vol. 54, pp. 608-23, 2000.

[11] A. Springsteen, "Standards for the measurement of diffuse reflectance - an overview of available materials and measurement laboratories," *Analytica Chimica Acta,* vol. 380, pp. 379-390, 1999.

[12] L. Bokobza, *Origin of Near-Infrared Absorption Bands*: Wiley-VCH Verlag GmbH, 2007.

[13] A. Dubovik, A. Apolenis, V. Annikov and E. Aleshkina, "Sensitivity and detonability of water-containing explosive compositions," *Combustion, Explosion, and Shock Waves,* vol. 44, pp. 360-364, 2008.

[14] J. E. Hay. (http://www.fas.org/irp/congress/1995_hr/h950612-3h.htm).

[15] A. Schreck, A. Knorr, K. D. Wehrstedt, P. A. Wandrey, T. Gmeinwieser and J. Steinbach, "Investigation of the explosive hazard of mixtures containing hydrogen peroxide and different alcohols," *J. Hazard. Mater.,* vol. 108, pp. 1-7, 2004.

[16] F. Dubnikova, R. Kosloff, J. Almog, Y. Zeiri, R. Boese, H. Itzhaky, A. Alt and E. Keinan, "Decomposition of Triacetone Triperoxide Is an Entropic Explosion," *Journal of the American Chemical Society,* vol. 127, pp. 1146-1159, 2005.

[17] C. M. Canal, A. Saleem, R. J. Green and D. A. Hutchins, "Remote identification of chemicals concealed behind clothing using near infrared spectroscopy," *Analytical Methods,* vol. 3, pp. 84-91, 2011.

[18] D. A. Burns and E. W. Ciurczak, *Handbook of near-infrared analysis*: CRC Press, 2008.

[19] J. R. M. Smits, L. W. Breedveld, M. W. J. Derksen, G. Kateman, H. W. Balfoort, J. Snoek and J. W. Hofstraat, "Pattern classification with artificial neural networks: classification of algae, based upon flow cytometer data," *Analytica Chimica Acta,* vol. 258, pp. 11-25, 1992.

[20] D. L. Massart, *Chemometrics : a textbook*. Amsterdam; New York; New York, NY, U.S.A.: Elsevier ; Distributors for the U.S. and Canada, Elsevier Science Pub. Co., 1988.

[21] P. J. Gemperline, J. R. Long and V. G. Gregoriou, "Nonlinear multivariate calibration using principal components regression and artificial neural networks," *Analytical Chemistry,* vol. 63, pp. 2313-2323, 1991.

[22] C. Borggaard and H. H. Thodberg, "Optimal minimal neural interpretation of spectra," *Analytical Chemistry,* vol. 64, pp. 545-551, 1992.

[23] M. Bos, A. Bos and W. E. van der Linden, "Tutorial review-Data processing by neural networks in quantitative chemical analysis," *Analyst,* vol. 118, pp. 323-328, 1993.

[24] T. B. Blank and S. D. Brown, "Nonlinear multivariate mapping of chemical data using feed-forward neural networks," *Analytical Chemistry,* vol. 65, pp. 3081-3089, 1993.

[25] J. R. Long, V. G. Gregoriou and P. J. Gemperline, "Spectroscopic calibration and quantitation using artificial neural networks," *Analytical Chemistry,* vol. 62, pp. 1791-1797, 1990.

[26] D. J. C. MacKay, "Bayesian interpolation," *Neural Computation,* vol. 4, pp. 415-47, 1992.

[27] F. Dan Foresee and M. T. Hagan, "Gauss-Newton approximation to Bayesian learning," in *Proceedings of International Conference on Neural Networks (ICNN'97), 9-12 June 1997*, New York, NY, USA, 1997, pp. 1930-5.

[28] R. J. Poppi and D. L. Massart, "The optimal brain surgeon for pruning neural network architecture applied to multivariate calibration," *Analytica Chimica Acta,* vol. 375, pp. 187-195, 1998.

[29] A. Savitzky and M. J. E. Golay, "Smoothing and Differentiation of Data by Simplified Least Squares Procedures," *Analytical Chemistry,* vol. 36, pp. 1627-1639, 1964.

[30] A. Candolfi, R. De Maesschalck, D. Jouan-Rimbaud, P. A. Hailey and D. L. Massart, "The influence of data pre-processing in the pattern recognition of excipients near-infrared spectra," *Journal of Pharmaceutical and Biomedical Analysis,* vol. 21, pp. 115-132, 1999.

[31] S. N. Thennadil, H. Martens and A. Kohler, "Physics-based multiplicative scatter correction approaches for improving the performance of calibration models," *Applied Spectroscopy,* vol. 60, pp. 315-321, 2006.

[32] D. K. Pedersen, H. Martens, J. P. Nielsen and S. B. Engelsen, "Near-infrared absorption and scattering separated by extended inverted signal correction (EISC): Analysis of near-infrared transmittance spectra of single wheat seeds," *Applied Spectroscopy,* vol. 56, pp. 1206-1214, 2002.

[33] M. Daszykowski, S. Serneels, K. Kaczmarek, P. Van Espen, C. Croux and B. Walczak, "TOMCAT: A MATLAB toolbox for multivariate calibration techniques," *Chemometrics and Intelligent Laboratory Systems,* vol. 85, pp. 269-277, 2007.

[34] J. R. M. Smits, W. J. Melssen, L. M. C. Buydens and G. Kateman, "Using artificial neural networks for solving chemical problems: Part I. Multi-layer feed-forward

networks," *Chemometrics and Intelligent Laboratory Systems,* vol. 22, pp. 165-189, 1994.

[35] S. Verboven and M. Hubert, "LIBRA: a MATLAB library for robust analysis," *Chemometrics and Intelligent Laboratory Systems,* vol. 75, pp. 127-136, 2005.

[36] F. Despagne and D.-L. Massart, "Variable selection for neural networks in multivariate calibration," *Chemometrics and Intelligent Laboratory Systems,* vol. 40, pp. 145-163, 1998.

[37] J. R. M. Smits, P. Schoenmakers, A. Stehmann, F. Sijstermans and G. Kateman, "Interpretation of infrared spectra with modular neural-network systems," *Chemometrics and Intelligent Laboratory Systems,* vol. 18, pp. 27-39, 1993.

[38] ASTM, "Standard Practices for Infrared Multivariate Quantitative Analysis," vol. ASTM E1655 - 05, ed. ASTM International Technical Committee E13 on Molecular Spectroscopy and Separation Science: American Society for Testing and Materials, 2005.

[39] R. D. Snee, "Validation of Regression Models: Methods and Examples," *Technometrics,* vol. 19, pp. 415-428, 1977.

[40] R. W. Kennard and L. A. Stone, "Computer Aided Design of Experiments," *Technometrics,* vol. 11, pp. 137-148, 1969.

[41] F. Estienne, L. Pasti, V. Centner, B. Walczak, F. Despagne, D. J. Rimbaud, O. E. de Noord and D. L. Massart, "A comparison of multivariate calibration techniques applied to experimental NIR data sets. II. Predictive ability under extrapolation conditions," *Chemometrics and Intelligent Laboratory Systems,* vol. 58, pp. 195-211, 2001.

[42] H. van der Voet, "Comparing the predictive accuracy of models using a simple randomization test," *Chemometrics and Intelligent Laboratory Systems,* vol. 25, pp. 313-323, 1994.

[43] K. R. Beebe, R. J. Pell and M. B. Seasholtz, *Chemometrics : a practical guide.* New York: Wiley, 1998.

Chapter 5

Lock-in amplification and 2D spectroscopic imaging

5.1 Introduction

The work presented in the preceding chapters established the feasibility of using NIR spectroscopy as a technique to detect specific chemicals across single intervening layers of clothing fabrics. The eventual deployment of this technique in a practical security screening application would depend on establishing performance benchmarks in situations that resemble a practical screening environment, coupled with the ability to efficiently process and present the detection results to the operator in a user-friendly format. If the technique were to be utilized in a portable security screening system, it would need to be capable of operating in the presence of high levels of ambient noise affecting the relevant frequency band (for instance in the presence of direct sunlight). Provision would need to be made to enhance the signal-to-noise ratios (SNRs) adequately within the collected spectral data, so these could be used to drive the relevant calibration models that would be trained to detect the chemicals of interest.

To help deal with this problem, the use of lock-in amplification has been investigated by the author and others as a technique to provide such enhancement in SNR [1, 2]. Here, this approach is used to enhance the detection and identification of spectra in one set of measurements. Additionally, a scanning system has been designed using a two-dimensional software-controlled scan-stage to perform cross-sectional imaging of selected chemicals in containers. The results are then displayed by means of colour-coded contoured intensity images, based on the output of neural network-based multivariate calibration models. The following sections contain a description of the experimental arrangement used, including the scanning software developed for the purpose, followed by the results of scans performed with a selection of chemicals relevant to security screening.

5.2 Experiment

The experiment was based on collecting NIR spectra of glass cells containing chemicals of interest hidden behind fabric layers as a 2D scan, using a software-based lock-in

amplifier to process the recorded spectra. The resulting spectra were then used offline in Matlab for training and testing neural networks designed for pattern-recognition/classification, in order to detect the presence of the chemicals. Each of these steps is now considered separately.

5.2.1 Experimental arrangement

The equipment layout used for these experiments is shown schematically in Figure 5.1.
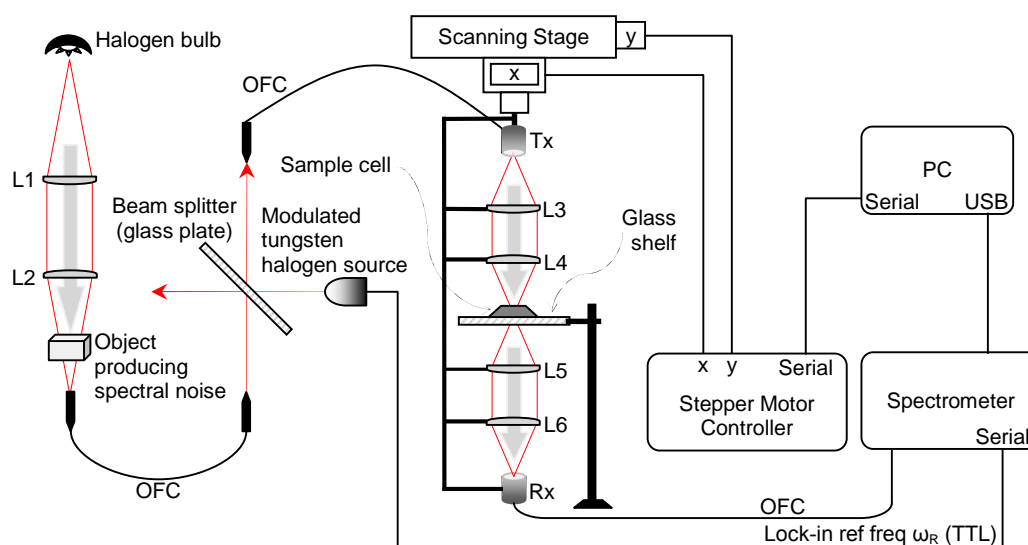
Figure 5.1 – Schematic diagram of experimental arrangement used for collection and lock-in amplification of NIR spectral data.

The target chemical sample was held within a glass cell with a 1 mm wall thickness, and placed on top of a glass shelf attached to a 2D scan stage. The incident NIR signal was generated by means of a tungsten halogen light source, and was modulated at the lock-in amplifier reference frequencyω_R. This frequency was software-generated on the PC as a 1-5 Hz square wave, and routed to the source via the spectrometer as a TTL signal switching the source on/off at the frequency ω_R. A second component could also be added to this signal as a source of spectral noise in order to test the ability of the lock-in process to recover the original signal from such noise. This component was generated by a broadband halogen source, and transmitted through a test object such as a clear PET bottle so as to acquire the spectral profile of that object. The two components were combined together using a beam splitter arrangement [3], and delivered to the scanning stage via a low-OH content optical fibre cable (OFC). The NIR beams were conditioned throughout the process by means of an arrangement of optical lenses comprising

collimating lenses L1, L3 and L5, and focusing lenses L2, L4 and L6. The signal transmitted through the sample in the scan stage was routed via an OFC to the spectrometer, and the spectrometer output was processed with optional lock-in amplification on the PC. The specifications of all the optical components used in the arrangement are given in Table 5.1. All absorption spectra were recorded with reference to the uninterrupted signal intensity (with no target present) from the tungsten halogen source, with the exception of scans performed in the presence of fabric layers, in which case intensity across the relevant fabric layers was taken as reference.

Table 5.1 – Specifications of components used in the optical bench.

Component	Qty	Vendor/ Model	Specifications
Halogen lamp	01	Ikea	Power: 50 W.
Tungsten halogen light source	01	Ocean Optics HL-2000-FHSA	WL range: 360 nm–2 µm (visible-NIR) Power: 7 W; manual & TTL shutter.
Lens L1	01	Thorlabs LA1979	Plano-convex; BK7; uncoated; f' = 200 mm; ϕ = 50.8 mm.
Lens L2	01	Melles Griot LPX-60.0-51.9-C	Plano-convex; BK7; uncoated; f' = 100 mm; ϕ = 60 mm.
Lens L3	01	Thorlabs	Plano-convex; uncoated; f' = 10 mm; ϕ = 6 mm.
Lens L4	01	Thorlabs	Plano-convex; coated; f' = 25 mm; ϕ = 12.7 mm.
Lens L5	01	Thorlabs	Plano-convex; coated; f' = 25 mm; ϕ = 12.7 mm.
Lens L6	01	Thorlabs	Plano-convex; coated; f' = 25 mm; ϕ = 12.7 mm.
Optical fibre cable	03	Ocean Optics VIS-NIR low OH fibre	Core = 600 µm; numerical aperture = 0.22.
NIR spectrometer	01	Ocean Optics NIR256-2.1	Sensor: InGaAs linear array (256 pixels); sensitivity range = 860 – 2 200 nm.

5.2.2 Chemicals and clothing fabric imaged

The chemicals used in this case are listed in Table 5.2.

Table 5.2 – Chemicals used to investigate lock-in amplification and spectroscopic imaging.

SN	Chemical	Formula	Supplier	Physical state	Concentration
1	Ammonium nitrate	NH_4NO_3	Fisher scientific	Aqueous solution	1.5 g.ml^{-1}
2	Ethanol	C_2H_5OH	Fisher scientific	Liquid	100 % v/v
3	Hydrogen peroxide	H_2O_2	Fisher scientific	Aqueous solution	30 % v/v
4	Distilled water	H_2O	Warwick Chemistry Dept	Liquid	99 % v/v

Scans were carried out to image these chemicals both separately and simultaneously in sets of two. In the latter case, the two cells containing the chemicals were placed alongside each other on the glass shelf, and the scan dimensions adjusted to cover both the cells. Further scans were carried out with the chemical/s covered by a layer of white polyester fabric, to investigate the possibility of lock-in amplification and detection across such layers.

5.2.3 Lock-in amplification

5.2.3.1 Theoretical model

It may be appreciated that the purpose of lock-in amplification is to enable more effective measurement of AC signals that might be buried in noise that is many orders of magnitude higher than the signal amplitude [4]. This is accomplished by modulating the source of the AC signal with a specific reference frequency ω_R, and then using an analogue instrument, or alternatively demodulating the signal at the receiving end by taking a Fourier transform of the received signal to extract the component at ω_R. Thereby, the process equates to band-pass filtering the received signal with centre frequency ω_R and a narrow bandwidth (on the mHz scale). The process is shown in the form of a block diagram in Figure 5.2 [5].
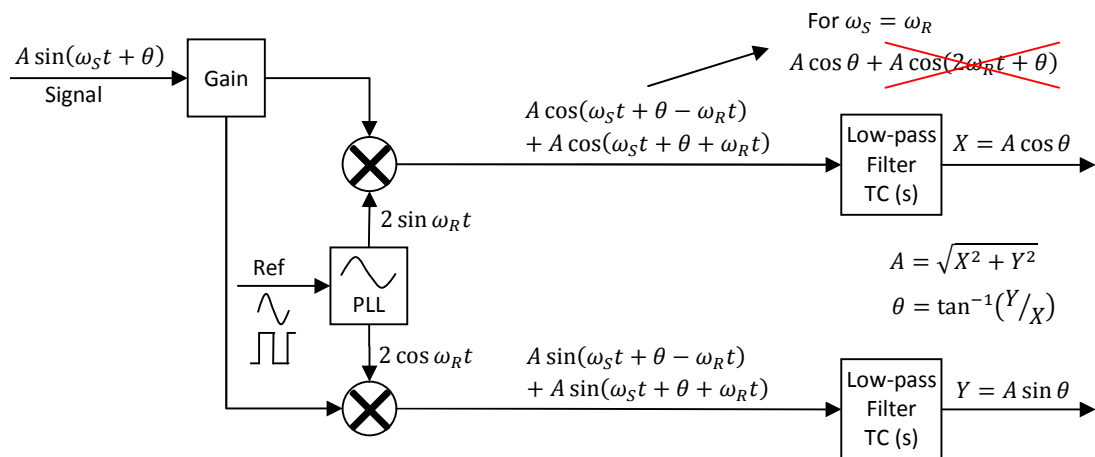
Figure 5.2 – Block diagram of lock-in amplifier used to process spectral data.

The reference signal at ω_R is fed to a frequency synthesizer based on phase-locked loop (PLL), which generates a pure sine wave at ω_R. This is mixed with the received signal, which was modulated at the point of origin with ω_R, and has now been contaminated by a spectrum of frequency components based in noise. For each of the frequency

components in the received signal, the mixer generates two components at the output: one with frequency equal to the difference between the signal frequency and the reference frequency ($\omega_S - \omega_R$), and the other with frequency that is the sum of these two frequencies ($\omega_S + \omega_R$). Then, in the case of the received signal component modulated with ω_R, *i.e.* where $\omega_S = \omega_R$, the first of these components has frequency equal to zero, *i.e.* a DC signal, while the second component has frequency equal to twice the reference frequency, *i.e.* $2\omega_R$. The subsequent low-pass filtering rejects all frequencies except this DC component, which has amplitude X that is proportional to the amplitude A of the received signal component at ω_R, and the cosine of the phase difference θ of this component with respect to the reference signal ($X = A\cos\theta$). Similarly, if the above process is replicated in parallel with a reference frequency component that is a cosine wave, the corresponding output Y of the low-pass filter is comprised of the product of amplitude A and the sine of phase difference θ ($Y = A\sin\theta$). Using X and Y, the amplitude A and relative phase θ of the requisite AC signal can then be determined.

In a practical implementation, the segregation of the DC component at the low-pass filter stage is not ideal, and is limited by the filter cutoff frequency (f_c). Hence, while the filter provides necessary suppression of frequencies outside the bandwidth $\omega_R \pm f_c$, all components within this band end up in the output, which tends to degrade the results. The design of this output filter stage is therefore crucially important in making precise measurements, and represents a necessary compromise between the speed and precision of the measurements, as explained below.

The conventional expression of filter bandwidth in the case of lock-in amplifiers is *not* in terms of frequency in Hz, but in terms of filter time-constant τ, measured in seconds. This is in view of, and emphasizes, the fact that τ is directly proportional to filter settling time (which is in turn inversely proportional to the bandwidth in Hz). For instance, filter cutoff frequency (taken as the frequency at which the signal is 3 dB down with a 1st order filter) of an FIR filter implemented in this case was equal to $0.35/\tau$ Hz, while the cutoff frequency of an IIR filter was $1/(2\pi\tau)$ Hz. Therefore, faster rates of measurement, with corresponding shorter τ values, would lead to wider bandwidths with the associated cost in terms of reduced precision. Similarly, longer

settling time would provide more precise measurements, albeit with reduced data throughput rate.

For the application at hand, a τ value of 1 sec with 1st order FIR filter was seen to provide the best combination of precision and data throughput rate.

5.2.3.2 Implementation in scanning software

A software version of a lock-in amplifier was programmed in LabVIEW [6]. The basic code to implement a phase-locked loop, demodulator and low-pass filter was obtained from an open source [5], and adapted to process spectroscopic data. In essence, this meant that the spectral data generated by the spectrometer in each of the wavelength channels was seen by the software as a distinct AC signal to be assessed by the lock-in amplifier.

Raw spectral data from the scan stage were routed to the PC (ref. Figure 5.1) and fed to the lock-in amplifier in real time. The algorithms were designed to parallel-process as many of the data channels as possible to comprise the lock-in amplified spectral output, which was saved and processed offline for chemical detection in Matlab. While the software was rigorously optimized for efficient execution and to minimize processing overheads, the maximum number of channels that could be processed at any given time was limited by the processing power of the host computer: On a mid-range Windows-based PC, up to 40 channels (out of a total of 256) could be processed in parallel without incurring timing conflicts.

A range-selection mechanism was, therefore, included in the graphical user interface (GUI) to allow the user to specify an initial wavelength, channel spacing (or the number of channels to skip between adjacent selected channels), and the total number of channels to process. On the one hand, this allowed coverage of the entire wavelength range with 40 channels spaced 5 channels apart (albeit with the associated cost in terms of reduced resolution), while on the other hand, it provided the means to examine a particular spectral feature in greater detail by setting channel spacing to 1 *i.e.* using all consecutive channels, and starting with a channel at the beginning of the particular feature.

Chapter 5: Spectral imaging in 2D and lock-in amplification

The scan stage control routines were integrated with the lock-in amplifier to allow the amplifier to work in tandem with the scanning software. Thus, lock-in amplified spectral data, collected for each test sample, comprised point-scans made in a raster-scan profile covering a predefined cross-sectional area, with a specific step size along the surface of the sample. This was enabled in part by switching the tungsten halogen source at the lock-in reference frequency ω_R to generate the modulated interrogation signal, and feeding the spectral data collected as a result to the lock-in amplifier. This was done only during the intervals when the stage came to rest at new points along the scan path. Source-switching and feeding the data collected during the preceding stationary interval to the lock-in amplifier was then achieved when the stage moved. Thus, an uninterrupted stream of reference and signal data fed to the lock-in amplifier was maintained, while ensuring the source-switching, data-recording and stage-moving operations remained synchronized. The lock-in PLL algorithm was thus able to maintain the 'lock' on the reference frequency, and the demodulator and LPF algorithms were saved from exposure to any sudden adjustments in the signal data when the stage moved.

The GUI of the scanning software is shown in Figure 5.3, with the wavelength selection panel, the activation switch for the lock-in amplifier, and the two panels used to control and monitor amplifier operation (labeled PLL and DEMODULATOR/ LPF) identified.

A brief description of the main controls and indicators in these amplifier panels is as follows. The panel used to apply PLL on the reference signal is shown separately in Figure 5.4. The indicators labeled Ref Freq (Hz) and Ref Phase (deg) are used to display the frequency and phase information in respect of the reference signal as measured by the PLL algorithm. The amount of reference signal data used to make these measurements is determined by the PLL filter time constant shown in the Filter TC(s) indicator. Note that the larger the amount of data used, the more precise the measurements. As a minimum, the algorithm uses three periods of data to make these measurements. However, if the size of the data blocks passed to the algorithm exceeded three cycles, the whole block was utilized for the purpose irrespective of the number of cycles it took.
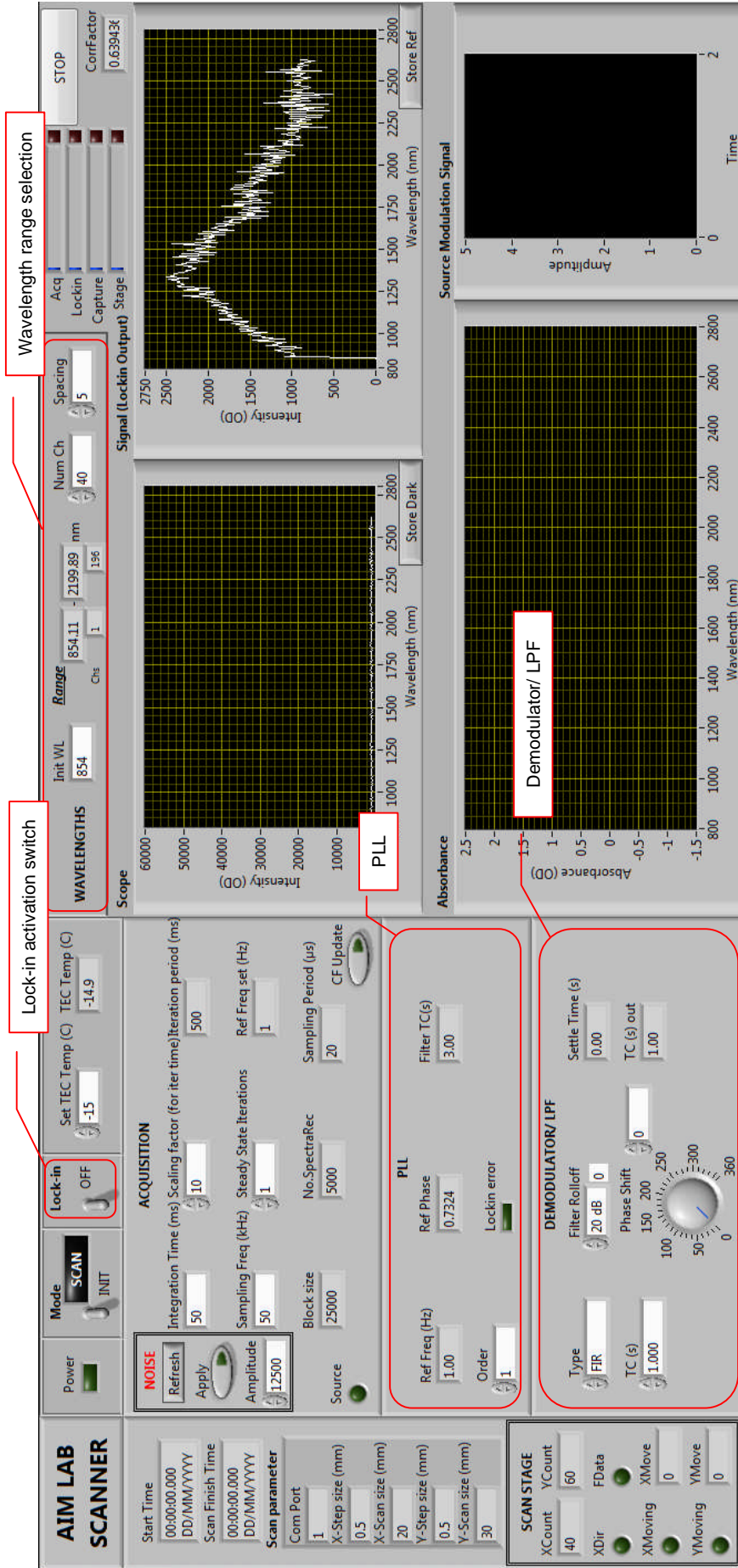
Figure 5.3 – Front panel GUI of scanning software used for collection and lock-in amplification of spectral data over specified target cross-sections. Marked are the panels used to control and indicate the operation of the lock-in amplifier.

For instance, the reference frequency used for most of the measurements in this case was 1 Hz, alongside a sampling frequency of 50 kHz (the lowest permissible value in the relevant algorithm) and data block size of 25,000 (based mainly on the integration time of the spectrometer). This meant that a single block of data was passed to the PLL algorithm in 0.5 seconds, *i.e.* over half a cycle. The algorithm therefore utilized three cycles worth of data, or six consecutive blocks of data, to make these measurements, with the corresponding filter TC value set to 3 seconds.
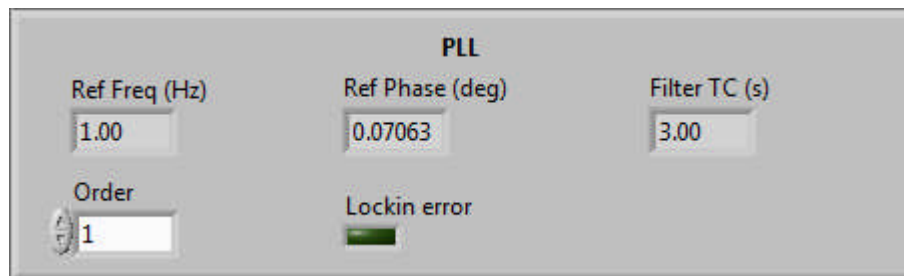
Figure 5.4 – The lock-in amplifier PLL control/ indication panel in the scanning software.

The Order control is used to coerce the algorithm to lock onto a given harmonic of the reference frequency. The precaution that needs to be exercised in this case is to use a value that does not cause the resultant reference frequency to exceed one half of the sampling frequency. During these experiments, this value was kept at 1, as the original reference frequency was used to modulate the light source (ref. Figure 5.1). Finally, the Lockin error indicator provide a warning if, for any reason, the algorithm fails to achieve or maintain a lock on the reference frequency.

The second lock-in amplifier panel, shown in Figure 5.5, is used to set and display the parameters used in the demodulator and low-pass filter sections.
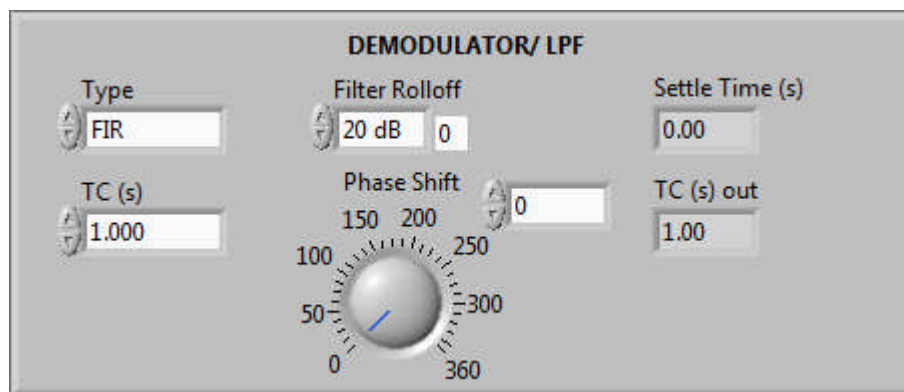
Figure 5.5 – The lock-in amplifier demodulator and low-pass filter panel.

Chapter 5: Spectral imaging in 2D and lock-in amplification

The controls labelled Type, TC (s) and Filter Rolloff define the core parameters of the low-pass filter used to eliminate the $2\omega_R$ frequency component in the mixer output (ref. Figure 5.2). Of these, the Type control provides a selectable range of five filter types, which are all variation of 10th order IIR and FIR filters. These are described below:

- IIR (2-dig)

  This selects an IIR filter, with the Settle Time (s) indicator updated to reflect the time it would take the filter to settle to 99% of the target value. This filter would provide the preferable option over an FIR filter in this application if small time constant values are required relative to the sampling (or conversion) interval [7]. This is borne out by the relatively less numerically intensive processing required in this case, which speeds up the overall operation. Thereby, the criterion that might be employed in deciding whether this filter would prove to be a better choice is if the required filter time constant were less than 10,000 times the conversion interval. For instance, in this study the conversion interval at a sampling frequency of 50 kHz came to 20 µs. As the desired time constant of 1 sec was more than $10,000 \times 20$ µs $= 0.2$ sec, the use of this filter was not deemed necessary. It would, however, be the preferred type if, for example, a time constant of 20 ms was desired.

- IIR (5-dig)

  This applies the same filter as above; however, in this case, the Settle Time (s) indicator displays the time taken by the filter to settle the output to 99.999% of its final value.

- FIR

  This represents a standard FIR filter. As explained above, the relatively more numerically intensive nature of this choice might not provide the best solution when the desired time constant value is less than 10,000 times the conversion interval. However, such an issue would prove to be a more pressing concern if the processing is being done on a slow-running computer.

- FIR (ENBW)

  This selects the same FIR filter as above, except with the difference that the time constant set alongside in the TC (s) control now represents the time constant of an IIR filter. This FIR filter is then implemented so that its equivalent noise bandwidth (ENBW) [8] matches that of the IIR filter with the given time constant. Thus, in order to match the lower ENBW of the IIR filter, this FIR filter is applied with a

Chapter 5: Spectral imaging in 2D and lock-in amplification

higher time constant than the one displayed. While this inevitably leads to longer settling time, this time is still shorter than that obtained with IIR (5-dig).

- FIR (Sync)

  This is an FIR filter which is applied with a time constant equal to a value closest to the displayed time constant that is an integer multiple of the inverse of twice the reference frequency $(1/2\omega_R)$. This is useful in cases where the reference frequencies are small, on the order of tenths of Hz. Recalling the purpose of the low-pass filter to effectively eliminate the $2\omega_R$ frequency component (ref. Figure 5.2), such small reference frequencies result in $2\omega_R$ signals that are very close to the required DC component. Filtering out the former with a 3rd or 4th order IIR filter then leads to considerably longer settling time than, for instance, a 3rd order FIR filter designed as above. This owes to the fact that the frequency response of FIR filters incorporates poles at integer multiples of $1/TC$ Hz. Note that during the course of these experiments, a reference frequency of 1 Hz was generally used, while an FIR filter was applied with a time constant of 1 sec. Hence, although filter type FIR was selected, this was equivalent to FIR (Sync).

As is evident, the TC (s) control in Figure 5.5 is used to specify the time constant τ of the low-pass filter. As explained above, if either of the filter types FIR (ENBW) or FIR (Sync) is selected, this value gets amended internally as necessary by the algorithm to design the selected filter. In all cases, the actual value of the time constant used in the specified filter is displayed in the TC (s) out indicator. As explained in Section 5.2.3.1, this value defines the cutoff frequency of the filter, equaling $0.35/\tau$ Hz for FIR filters, and $1/(2\pi\tau)$ Hz for IIR filters (assuming cutoff frequency is defined as the frequency at which the signal has been attenuated by 3 dB by a 1st order filter).

The Filter Rolloff control is used to select the order of the filter, ranging from 20 dB/ decade for the 1st order, to 200 dB/ decade for the 10th order filter. Note that the algorithm continuously evaluates the output of the selected FIR or IIR filter up to the 10th order, and provides the output corresponding to the order selected in this control. Further, as the output of higher order filters takes longer to settle and vice versa, the Settle Time (s) indicator is updated alongside to reflect the same.

Chapter 5: Spectral imaging in 2D and lock-in amplification

The Phase Shift control provides the means to introduce a lag in the reference signal used in the demodulator. This can affect an increase in the amplitude of X and Y signals at LPF outputs (ref. Figure 5.2) in cases where the signal arriving at the input of the lock-in amplifier has a substantial phase-shift θ relative to the reference signal. The phase shifts recorded during the current set of measurements, however, were negligible, as the spectra were collected at close range in a through-transmission arrangement as shown in Figure 5.1. It is felt that this control would prove more useful when the lock-in amplifier is adapted to record measurements in diffuse reflection at standoff distances as described in Chapters 3 and 4.

5.2.4 Chemical detection using neural networks

The lock-in amplified spectral data collected as above were used in neural network-based multivariate calibration models [9] trained for pattern recognition/ classification to identify chemicals of interest in the target samples. The considerations involved in the choice and design of neural networks, and the data pre-processing techniques used, were the same as those introduced in Chapter 4, Sections 4.3.1.1 and 4.3.1.2 respectively. The only exception in this case was the availability of a wider range of wavelength channels to process. This emanated from the fact that the glass cells used to contain the chemicals in this case had one-tenth the thickness of those used previously. Hence, the path length through the sample was reduced to 1 mm, compared with 20 mm (double the 10 mm cell thickness due to measurements in diffuse reflection) set previously. This prevented the strong absorption in 1,400 – 1,600 nm range from saturating the spectra [10]. The wavelength range included in the measurements, therefore, spanned 40 channels (with spacing = 5) from 850 nm to 2,200 nm.

5.2.5 Spectroscopic imaging

In order to investigate the feasibility of the technique in a two-dimensional spectroscopic imaging application, the optical apparatus held in the scanning stage (including transmitter, receiver and associated lenses labelled L3-L6 in Figure 5.1) was scanned in the horizontal plane following a raster scan profile to obtain spectral data at pre-defined intervals along the surface of the chemical cell, while the cell was kept stationary on the glass shelf. The resultant lock-in amplified spectral data were saved alongside the corresponding spatial scan coordinates, so that the scan profile could be

reconstructed later. Three scans were performed with each target set to cover the following scenarios:

1. No spectral noise added; no lock-in amplification performed.
2. Spectral noise introduced in all wavelength channels; no lock-in amplification.
3. Spectral noise maintained; all channels with lock-in amplification.

Test spectra collected as above were used to simulate trained neural networks to obtain the final classification data, which were plotted in the form of two-dimensional intensity images portraying the predicted location of the chemicals on grids defined by the pertinent scan coordinates.

5.3 Results

5.3.1 Scans with distilled water

5.3.1.1 Addition of spectral noise from a PET bottle

In an initial set of measurements, a cell containing distilled water was used as the target, while the signal transmitted through a PET bottle represented a source of unwanted additive spectral noise. As depicted in Figure 5.1, the signal impinging on the target water sample was comprised of i) a broadband signal modulated with the lock-in reference frequency, and ii) the interfering signal containing the spectra of the PET bottle. The spectra recorded with this arrangement in a point-scan are shown in Figure 5.6.

Figure 5.6 – Spectra collected with point-scans across a cell containing distilled water; (a) Water without additive spectral noise; (b) Spectral noise from a PET bottle introduced in (a); (c) Result of lock-in amplification of spectra in (b).

Figure 5.6(a) shows the spectrum of water recorded with the interfering signal from the PET bottle switched off. This profile was modified as seen in Figure 5.6(b) with the introduction of the PET signal, which gave rise to a characteristic peak at 1,675 nm [11]. As expected, the influence of the PET spectrum was effectively eliminated with the activation of the lock-in amplifier, as the signal carrying these spectra was not modulated with lock-in reference frequency. As seen in Figure 5.6(c), the resulting spectrum closely resembled the original, thus proving the effectiveness of lock-in amplification in cancelling out any spurious spectral content introduced by unwanted sources.

While the above measurements served to illustrate the usefulness of lock-in amplification in countering the effects of spectral noise, the relatively insignificant spectral distortion seen in Figure 5.6(b) was easily dealt with by the generalization capability of the neural network-based detection model, so that the distorted spectra were correctly classified as those of water. This is seen in Figure 5.7, where the results of the scan in the presence of noise without lock-in amplification (Figure 5.7(b)) are seen to be similar to those where no noise was introduced in the spectra (Figure 5.7(a)). While this precluded the need for lock-in amplification, the results obtained with same are shown in Figure 5.7(c). The edges of the cell are seen to be less well-defined in this case; however, the general shape, size and location of the detected cell remain the same.

(a)   (b)   (c)

Figure 5.7 – Neural network-based spectral pattern classification of 2D scans across a cell containing distilled water. Classification results with (a) original spectra (no additive noise), (b) spectra collected in the presence of noise (PET bottle), and (c) noisy spectra with lock-in amplification.

5.3.1.2 Software-generated spectral noise

Scans were performed to simulate the case where the spectral data collected were completely buried in noise, which was deemed to be a highly probable scenario in practical screening applications where measurements are often performed in

environments with high ambient noise. It was expected that the detection might fail in such a case in the absence of lock-in amplification.

The simulation was carried out by infusing the raw intensity spectra received from the spectrometer with high-amplitude software-generated uniform white noise in all wavelength channels. The provision for this was made in the scanning software by including a sub-panel for the purpose, labelled NOISE in Figure 5.3, which allowed addition of the noise signal with the specified RMS amplitude to the received spectra. Lock-in amplification of the resulting spectra was performed in the presence of increasing noise amplitudes, and the criterion for successful extraction of the signal from noise was based on the result of neural network-based classification. It was seen that the classification algorithm remained completely resilient to reduction in SNR of up to -40 dB (SNR = 1:100). Although appreciable detection results were obtained at SNR as low as -100 dB, the repeatability of the measurements was seen to get adversely affected with such noise levels. Figure 5.8 shows the results of point scans with SNR set at -60dB. As seen in Figure 5.8(b), all distinctive spectral features were lost in the noisy spectra. With the activation of the lock-in amplifier, however, spectral distortion was significantly diminished, and the spectral profile was recovered to a state close to the original form, as seen in Figure 5.8(c).
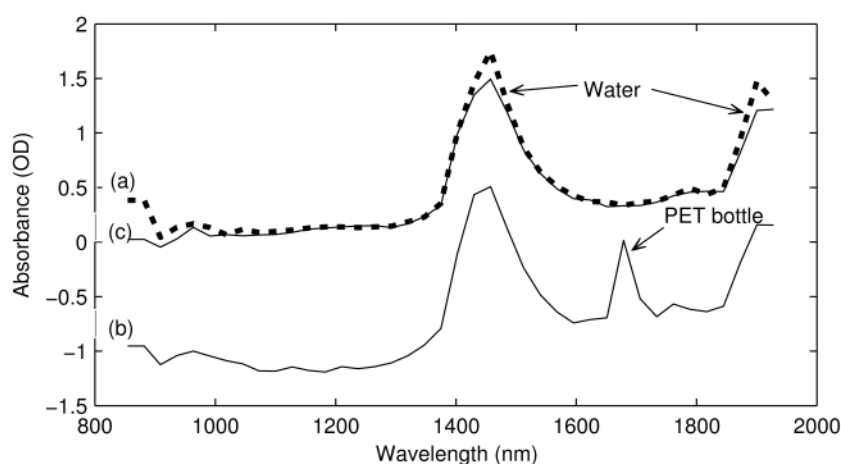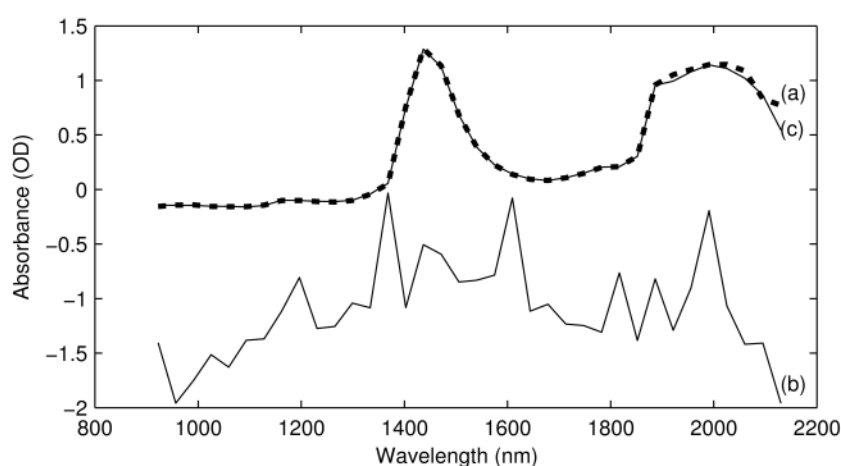

Figure 5.8 – Spectra collected with point-scans across a cell containing distilled water; (a) Water without additive spectral noise; (b) Software-generated uniform white noise introduced in (a) (SNR = -60 dB); (c) Result of lock-in amplification of spectra in (b).

Figure 5.9 shows intensity images depicting the outcome of the classification process for the three scenarios given in Figure 5.8. It is seen that in the absence of lock-in

amplification, the introduction of noise at an SNR of -60dB completely forestalled the detection process (Figure 5.9(b)), while lock-in amplification allowed recovery of the spectral data from the noise, and the detection to proceed with results closely matching those obtained in the absence of noise.
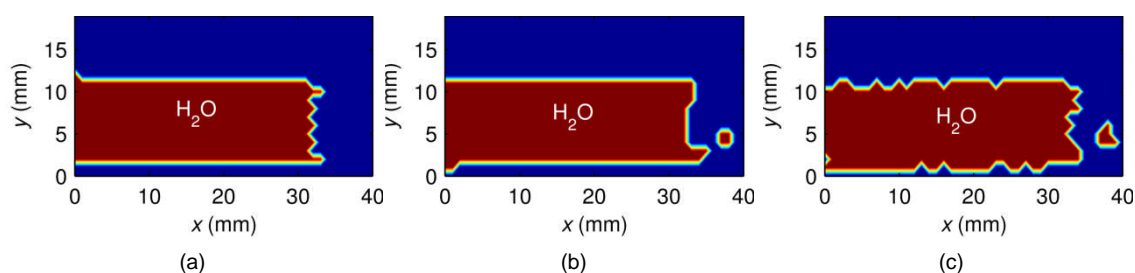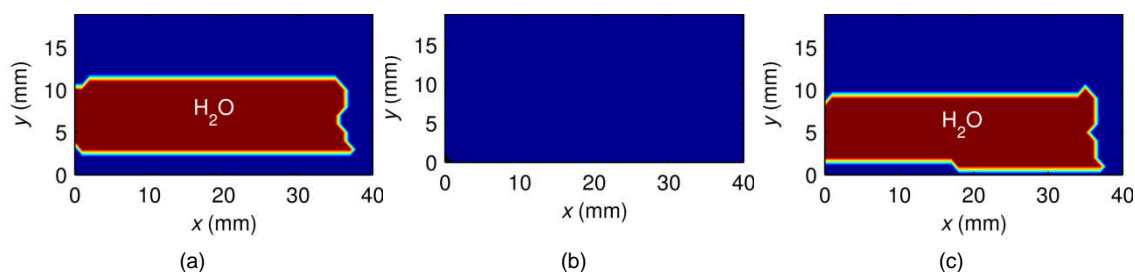

Figure 5.9 – Neural network-based spectral pattern classification of 2D scans across a cell containing distilled water. Classification results with (a) original spectra (no additive noise), (b) spectra collected in the presence of uniform white noise (SNR = -60 dB), and (c) noisy spectra with lock-in amplification.

5.3.2 Scans with combinations of different chemicals

The technique was used to scan and image target sets comprising two cells in each case, where each cell contained a different chemical. The test spectra collected were buried in software-generated spectral noise so as to maintain an SNR of -60dB. The same processing methodology as above was employed, including lock-in amplification followed by neural network-based classification, to identify the chemicals in the cells. Note that although the neural network was trained to classify all the pertinent chemicals, no more than two chemicals could be imaged simultaneously as only two cells were available in the required size for the tests. However, this arrangement was deemed to provide an adequate illustration of the feasibility of detecting multiple substances in a single scan.

The three chemicals used in the scans included solutions of ethanol, hydrogen peroxide and ammonium nitrate in the concentrations given in Table 5.2. As an initial step, point measurements were performed on each of these chemicals in turn to test the impact of noise on the respective spectral profiles, and the effectiveness of lock-in amplification in reducing such impact. The results of these scans with samples of ethanol, hydrogen peroxide and ammonium nitrate are given in Figures 5.10, 5.11 and 5.12 respectively.
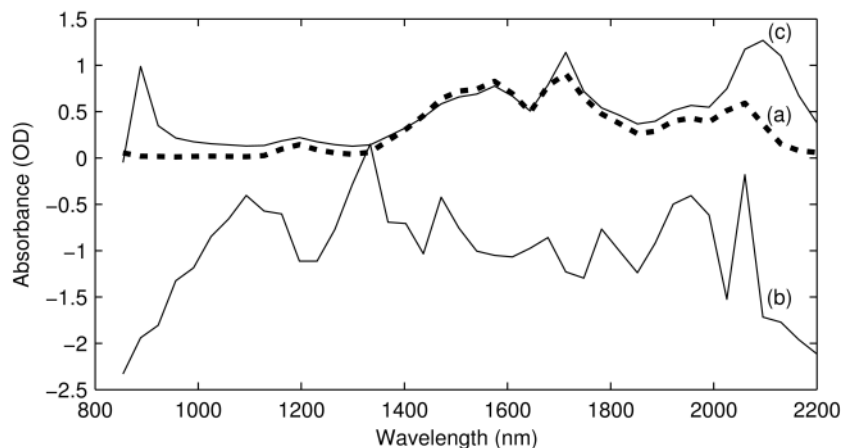
Figure 5.10 – Spectra collected with point-scans across a cell containing ethanol; (a) Ethanol without additive spectral noise; (b) Software-generated uniform white noise introduced in (a) (SNR = -60 dB); (c) Result of lock-in amplification of spectra in (b).
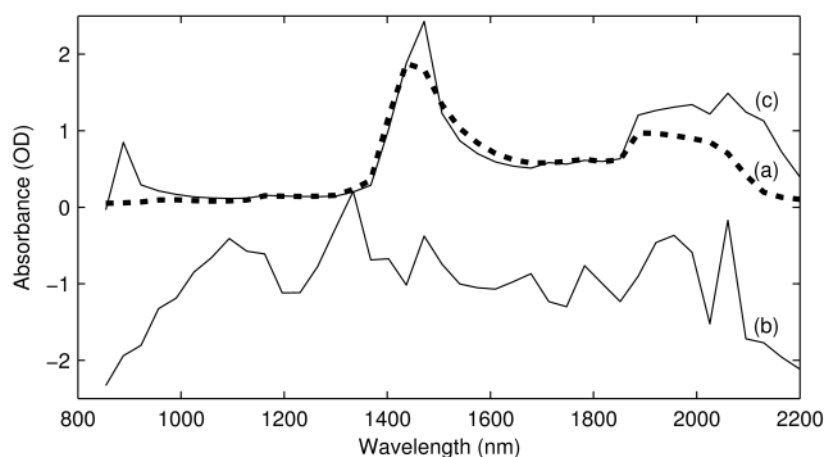
Figure 5.11 – Spectra collected with point-scans across a cell containing hydrogen peroxide; (a) Hydrogen peroxide without additive spectral noise; (b) Software-generated uniform white noise introduced in (a) (SNR = -60 dB); (c) Result of lock-in amplification of spectra in (b).

Figure 5.12 – Spectra collected with point-scans across a cell containing ammonium nitrate; (a) Ammonium nitrate without additive spectral noise; (b) Software-generated uniform white noise introduced in (a) (SNR = -60 dB); (c) Result of lock-in amplification of spectra in (b).

As seen, no recognizable spectral features from the chemical were present in any of the noisy spectra, while the original characteristic features were recovered from noise with lock-in amplification in each case. Note that all the spectra shown in Figures 5.10 – 5.12 are in the raw unfiltered form, which accounts for the sharp peaks seen in some of the cases. The spectra used in the classification algorithm, however, did not contain such anomalies, as these were filtered out at the pre-processing stage.

In the scans reported below, hydrogen peroxide was scanned in turn with each of the other chemicals. The greater emphasis placed on scanning/detecting hydrogen peroxide was in view of the popularity of this chemical as an ingredient in the manufacture of small but powerful improvised explosive devices [12, 13].

5.3.2.1 Hydrogen peroxide and ethanol

In the first instance, cells containing hydrogen peroxide and ethanol were scanned simultaneously. Intensity images depicting classification results obtained with the spectra collected in each of the three scanned scenarios are shown in Figure 5.13.
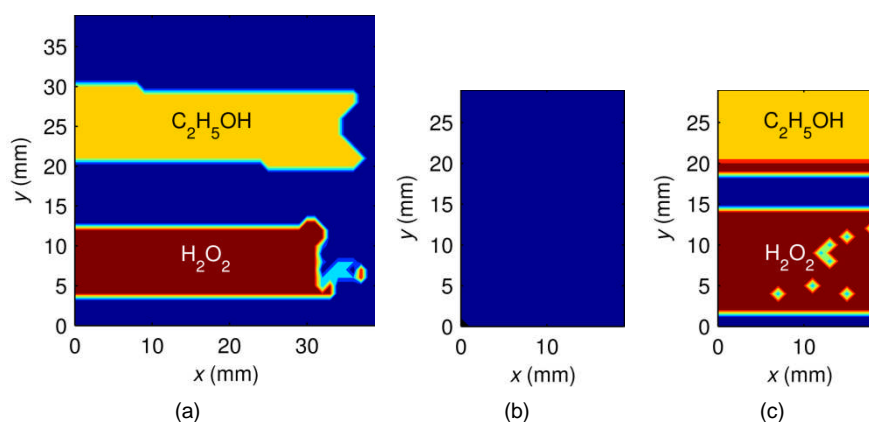
Figure 5.13 – Neural network-based spectral pattern classification of 2D scans across two cells containing hydrogen peroxide and ethanol. Classification results with (a) original spectra (no additive noise), (b) spectra collected in the presence of uniform white noise (SNR = -60 dB), and (c) noisy spectra with lock-in amplification.

As seen, the scan dimensions were reduced after the first scan (Figure 5.13(a)), while still covering parts of both the cells. This was prompted by the need to reduce the time taken to complete each scan. The time consumed in the first scan, with a grid size of 40 mm $\times$ 40 mm, step size of 1 mm, and scan rate of 2 sec/ point, was approximately one hour, which was reduced to 20 mins with the reduced grid size of 20 mm $\times$ 30 mm.

It is seen that a small number of spectra in Figure 5.13(a) and (c) were misclassified as ammonium nitrate (coloured cyan), while the spectra along the edge of the ethanol cell in Figure 5.13(c) were misclassified as hydrogen peroxide. However, the proportion misclassified was deemed to be within acceptable margin of error, as more than 90% of the spectra were correctly classified in both these cases. Finally, none of the spectra buried in noise were correctly classified in the absence of lock-in amplification (Figure 5.13(b)), which was consistent with the previous findings.

5.3.2.2 Hydrogen peroxide and ammonium nitrate

This scan was similar to the previous one, albeit with ammonium nitrate replacing ethanol alongside hydrogen peroxide. The corresponding intensity images depicting classification results are shown in Figure 5.14.

Figure 5.14 – Neural network-based spectral pattern classification of 2D scans across two cells containing hydrogen peroxide and ammonium nitrate. Classification results with (a) original spectra (no additive noise), (b) spectra collected in the presence of uniform white noise (SNR = -60 dB), and (c) noisy spectra with lock-in amplification.

It is seen that, as in the previous case, a small number of spectra were misclassified. The most noticeable of these were along the border of the ammonium nitrate cell in Figure 5.14(c), which were misclassified as ethanol (coloured yellow). However, the overwhelming majority of spectra were correctly classified, except those collected in the presence of high amplitude noise (SNR = -60 dB) without lock-in amplification (Figure 5.14(b)).

5.3.3 Scans in the presence of concealing fabric layer

A series of scans was recorded where the target sets were comprised of one or two chemical cells covered with a layer of polyester fabric. As explained in Chapter 3

(Section 3.4.1) and Chapter 4 (Section 4.2.2), fabric layers have characteristic spectra in the wavelength range of interest, which in this case comprised peaks of polyester at 1,135, 1,389 and 1,665 nm [14]. These spectral features tend to dominate the spectra of the chemicals recorded in the presence of such fabrics. Therefore, absorbance spectra were collected in this case with reference to the intensity signal recorded across the polyester layer, so as to base subsequent classification on the spectral features characteristic of the chemicals scanned. While this was understood to mitigate to some extent the distortive effect of the fabric layer, the measurements were still deemed to be less stable due to the expected diminishment of spectral amplitude when recorded with reference to the fabric layer. Additionally, any residual noise in the channels left unaccounted for by the lock-in algorithm presented another variable that could potentially affect the classification process.

With the above considerations in view, scans were recorded across solutions of hydrogen peroxide and ammonium nitrate (concentrations given in Table 5.2), with the cells hidden behind the fabric layer. With the tungsten halogen source operated at maximum power, the recorded intensity levels were reduced by a factor of 20 on average due to the fabric layer. Therefore, in order to maintain the SNR at -60dB, the amplitude of spectral noise introduced in the wavelength channels was reduced by the same factor. The point-scan spectra of hydrogen peroxide and ammonium nitrate collected with this arrangement are shown in Figures 5.15 and 5.16 respectively. As seen, the spectral profiles recorded in the initial scans (without noise) in (a), were well-preserved in the lock-in amplified spectra in (c).

Next, two-dimensional scans were performed with the two chemical cells first placed separately and then simultaneously on the glass shelf, covered in each case with the polyester layer. Note that ethanol was not scanned in this set of measurements, as the scans were confined to the other two chemicals with relevance in the manufacture of improvised explosives [15]. Accordingly, the neural network used for classification was trained to identify only the two scanned chemicals, and the colour map in the intensity images updated to use a different colour for ammonium nitrate. The results are presented below.

Chapter 5: Spectral imaging in 2D and lock-in amplification
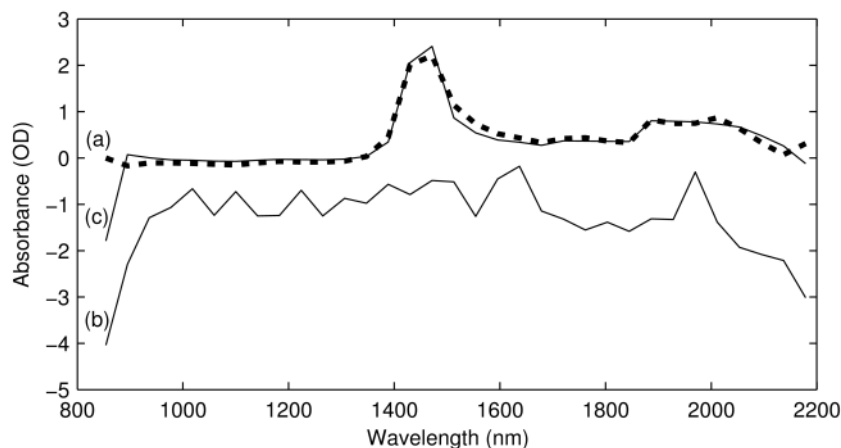
Figure 5.15 – Spectra collected with point-scans across a cell containing hydrogen peroxide hidden behind a layer of polyester; (a) Hydrogen peroxide behind polyester, without additive spectral noise; (b) Software-generated uniform white noise introduced in (a) (SNR = -60 dB); (c) Result of lock-in amplification of spectra in (b).
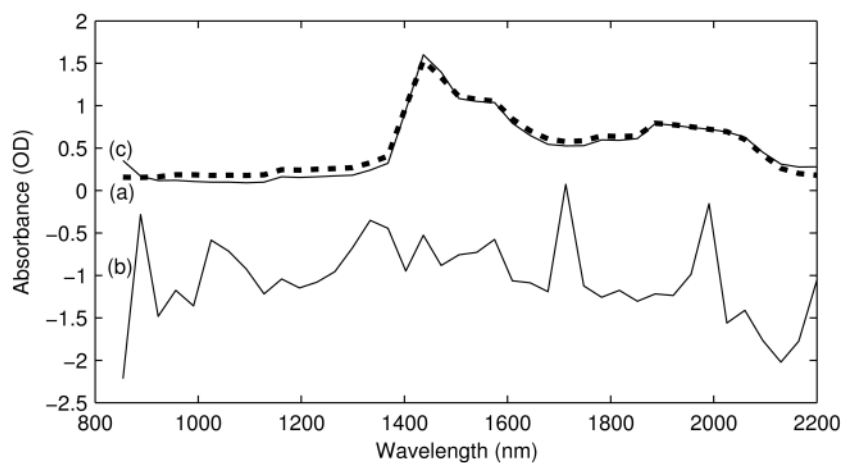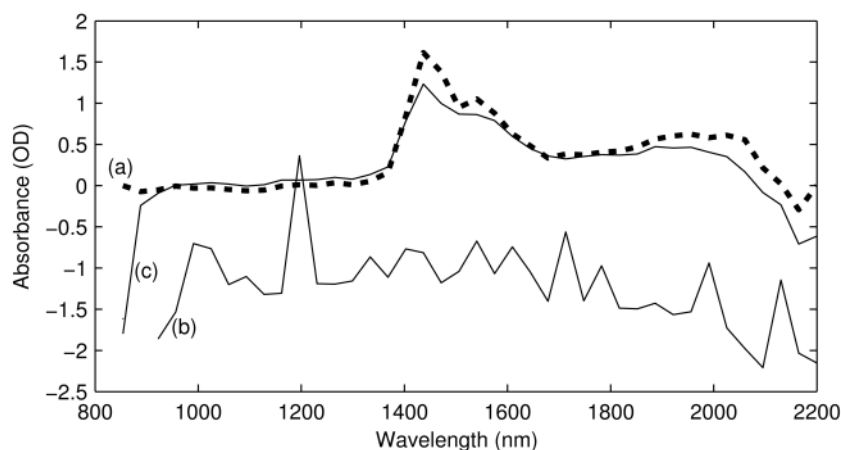

Figure 5.16 – Spectra collected with point-scans across a cell containing ammonium nitrate hidden behind a layer of polyester; (a) Ammonium nitrate behind polyester, without additive spectral noise; (b) Software-generated uniform white noise introduced in (a) (SNR = -60 dB); (c) Result of lock-in amplification of spectra in (b).

5.3.3.1 Hydrogen peroxide behind polyester layer

In the first instance, hydrogen peroxide was scanned while concealed behind polyester, with the collected spectra lock-in amplified and classified with a trained neural network. The results are shown in Figure 5.17. As seen, the results of classifying lock-in amplified spectra are very similar to those obtained with the original noise-free spectra. This demonstrates the usefulness of the technique in identifying chemicals hidden behind a layer of clothing.

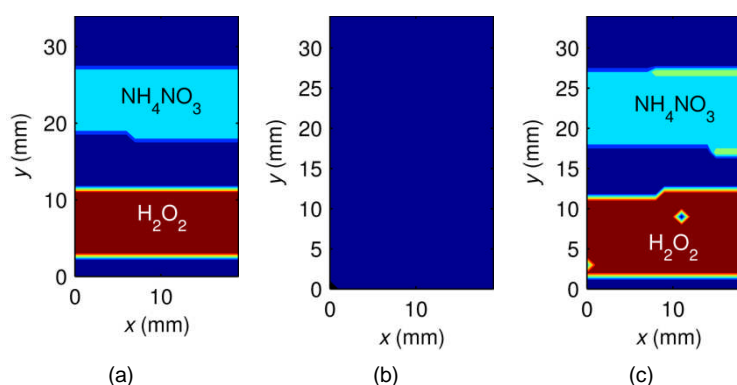*Figure 5.17 – Neural network-based spectral pattern classification of 2D scans across a cell containing hydrogen peroxide hidden behind a layer of polyester. Classification results with (a) original spectra (no additive noise), (b) spectra collected in the presence of uniform white noise (SNR = -60 dB), and (c) noisy spectra with lock-in amplification.*

5.3.3.2 Ammonium nitrate solution behind polyester layer

Next, scans were recorded with a cell containing aqueous ammonium nitrate solution, covered with the polyester layer. The results of spectral classification in the three imaged scenarios are given in Figure 5.18. It is seen that the outcome of classification based on lock-in amplified spectra (Figure 5.18(c)) was not entirely synonymous with that based on the original noise-free spectra (Figure 5.18(a)), with a substantial proportion of ammonium nitrate spectra in the former case misclassified as hydrogen peroxide.
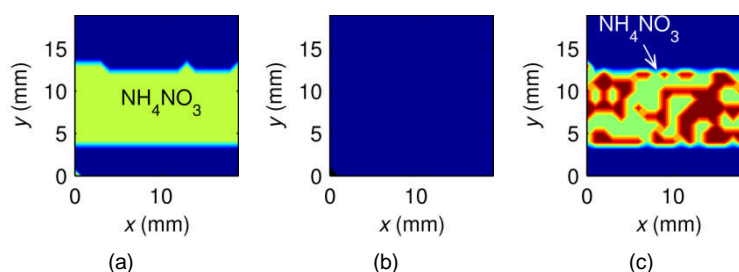
Figure 5.18 – Neural network-based spectral pattern classification of 2D scans across a cell containing ammonium nitrate hidden behind a layer of polyester. Classification results with (a) original spectra (no additive noise), (b) spectra collected in the presence of uniform white noise (SNR = -60 dB), and (c) noisy spectra with lock-in amplification.

As discussed at the beginning of this section, a possible source of this problem was residual noise in the channels after lock-in amplification. Although selection of a higher-order low-pass filter in the final stage of the lock-in algorithm (ref. Figure 5.2) would alleviate such a problem by affecting higher attenuation of noise in the amplifier output, this option was not feasible in this case as the higher settling time required with higher order filters introduced timing conflicts in the scanning process. Further, it was felt that the inherently precarious nature of measurements made in the presence of fabric layers might have led to such anomalous results, where the classification was not

consistent with the presence of one particular chemical. This necessitated the need for a post-processing mechanism to resolve such conflicts in the data.

5.3.3.3 The 'majority poll' method

Using an image-processing approach, a simple measure devised to identify the presence of a particular chemical was based on a 'majority poll' method. This was defined as the classification value present at a majority, *i.e.* more than 50%, of locations (pixels) within an area delineated exclusively by the borders of the image and/or the background (coloured dark blue) within the image. In order to mark out the area/s fulfilling this definition, an edge detection algorithm based on Canny's method [16-18] was used. After such an area had been marked, the percentage of pixels within that area belonging to each of the contending chemicals was calculated, and the chemical occupying more than 50% of the space, *i.e.* winning the majority poll, was deemed to be present throughout that area.

An illustration of the majority poll method is given in Figure 5.19, where it is applied on the image seen earlier in Figure 5.18(c).

(a)   (b)   (c)   (d)
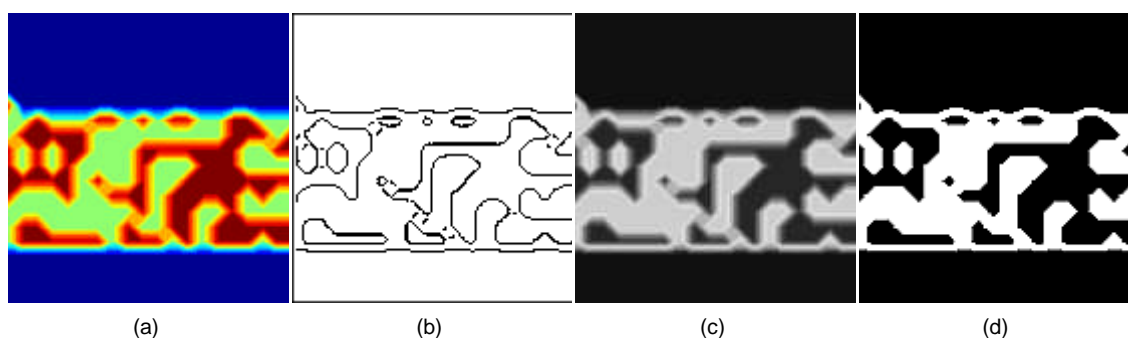
Figure 5.19 – Illustration of the 'majority poll' method applied to classification data shown in Figure 5.18(c). (a) Original classification results, predicting both ammonium nitrate and hydrogen peroxide. (b) Outcome of edge detection with Canny's method [16]. (c) Grayscale version of the original image. (d) Binary image, obtained by setting a threshold at 50% gray level in (c).

The original image is shown again for comparison in Figure 5.19(a), with the outcome of the edge-detection algorithm given in (b). It is seen that the only area defined by the detected edges that is delineate on all sides exclusively by the background and the borders of the image, is described by the rectangular band enclosing all the other edge contours. The data within this area are therefore deemed to belong to a single chemical, and tested to determine the identity of that chemical. The image is first converted to

greyscale as shown in (c). The midpoint of the greyscale colour map (128, with the conventional 256-value gray map) is set as a threshold in this image to convert it to the binary image shown in (d). Note that the 'high' pixels in the latter image correspond to ammonium nitrate as predicted in (a). The proportion of these pixels, as a percentage of the total number of pixels in the area, is used as a measure of the said chemical. In this case, this was calculated to be 59.4%, which was deemed to indicate the presence of ammonium nitrate in the given area. Note that if the calculated percentage were less than 50%, detection would have been announced in favour of the other contender *i.e.* hydrogen peroxide.

5.3.3.4 Chemicals placed simultaneously behind polyester layer

These scans were recorded with cells of the two chemicals (hydrogen peroxide and ammonium nitrate) placed simultaneously on the shelf, hidden behind the polyester layer. The relevant classification results obtained with spectra collected in the three scans are shown in Figure 5.20.

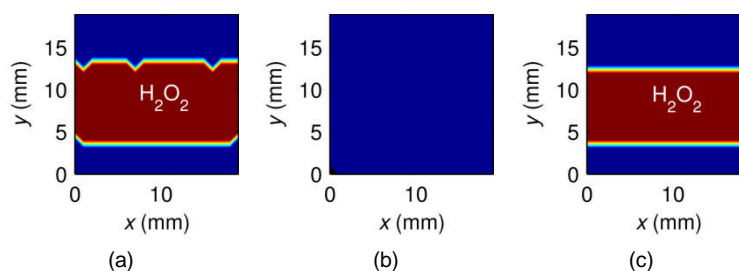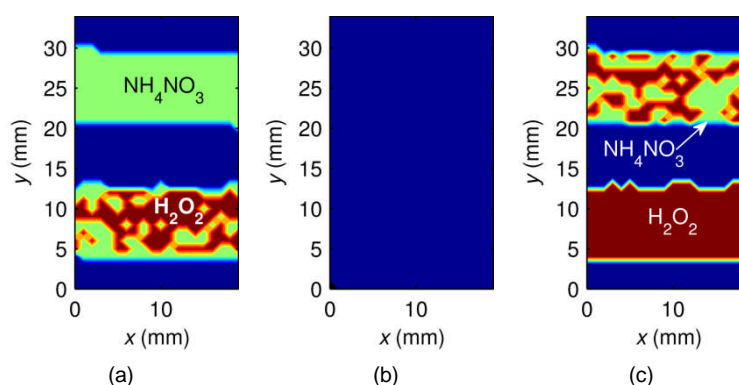*Figure 5.20 – Neural network-based spectral pattern classification of 2D scans across cells containing hydrogen peroxide and ammonium nitrate, hidden behind a layer of polyester. Classification results with (a) original spectra (no additive noise), (b) spectra collected in the presence of uniform white noise (SNR = -60 dB), and (c) noisy spectra with lock-in amplification.*

It is seen that two of the scans, one each in Figures 5.20(a) and (c), produced anomalous classification results in a manner similar to that seen earlier in the preceding set of measurements (Figure 5.18(c)). These images were therefore tested with the 'majority poll' method described earlier.

The resultant measured proportion of ammonium nitrate in the anomalous scan in Figure 5.20(a) was 49.2%, and hence, the proportion of hydrogen peroxide was 50.8%.

Although this result was used to announce the detection of hydrogen peroxide based on the majority poll criterion, this was understood to be within the margin of error. Note that in a practical screening application, such a result might prompt more detailed analysis of the pertinent sample, in the first instance with the fabric layer removed, and followed by lab-based testing.

The majority poll result obtained with the anomalous scan in Figure 5.20(c) was more definitive, with the proportion of ammonium nitrate measured at 62.2%. As in the previous cases, the lock-in process was seen to be crucially important in recovering the spectra from noise.

5.4 Conclusions

This work was aimed at introducing enhancements in the detection capability offered by NIR spectroscopy as reported in the previous chapters, in order to perform such detection in the presence of high-amplitude noise, carry out two-dimensional scans covering pre-determined cross-sectional areas on sample surfaces, and present the classification results obtained with the collected chemical spectra in the form of colour-coded intensity images depicting the presence of the relevant chemicals as predicted by the classifying neural network models.

The signal-enhancement technique adapted to work with spectroscopic data so as to aid detection in the presence of spectral noise was lock-in amplification. This was implemented as an initial processing step within the scanning software designed for the purpose, before the spectra were pre-processed and used to simulate the pattern-recognition/ classification model. The scans performed with solutions of ethanol, hydrogen peroxide and ammonium nitrate showed accurate detection of these chemicals in through-transmission measurements at close range with signal-to-noise ratio set as low as -60dB. The same classification results were used to construct 2-dimensional contour images of the chemical cells to illustrate a possible application of the technique.

Some of the classification results obtained at -60 dB SNR with ammonium nitrate and hydrogen peroxide solutions hidden behind a layer of polyester fabric were shown to contain certain anomalies, where a sizable proportion of the spectral data within the

scanned area were misclassified. An image processing technique, termed 'majority poll', was devised to use the contents of the pertinent intensity images to determine which particular chemical was shown to occupy more than 50% of a certain area within an image, and to announce detection of that chemical in the said area.

5.5 References

[1] A. Saleem, C. Canal, D. A. Hutchins and R. J. Green, "NIR spectroscopy with multivariate calibration and lock-in amplification to detect chemicals concealed behind fabrics," in *Chemical, Biological, Radiological, Nuclear, and Explosives (CBRNE) Sensing XII, part of SPIE Defense, Security, and Sensing*, Orlando, Florida, USA, 2011, pp. 8018 I 1-18.

[2] M. J. Holcomb and W. A. Little, "Cascading lock-in amplification: application to wavelength modulation spectroscopy," *Review of Scientific Instruments,* vol. 63, pp. 5570-5, 1992.

[3] E. Hecht, *Optics*. Reading, Mass.: Addison-Wesley, 2002.

[4] A. R. Hambley, *Electronics*. Upper Saddle River, N.J.: Prentice Hall, 2000.

[5] National-Instruments. (2003). *NI Lock-In Amplifier Start-Up Kit*. Available: http://digital.ni.com/express.nsf/bycode/lockin?opendocument&lang=en&node=seminar _US

[6] G. W. Johnson and R. Jennings, *LabVIEW graphical programming*. New York: McGraw-Hill, 2006.

[7] L. Litwin, "FIR and IIR digital filters," *IEEE Potentials,* vol. 19, pp. 28-31, 2000.

[8] D. L. Schilling and C. Belove, *Electronic circuits discrete and integrated*. New York: Mc Graw-Hill, 1989.

[9] S. Sharma, *Applied multivariate techniques*. New York: J. Wiley, 1996.

[10] Y. Ozaki, *Applications in Chemistry*: Wiley-VCH Verlag GmbH, 2007.

[11] J. Rodgers and K. Beck, "NIR Characterization and Measurement of the Cotton Content of Dyed Blend Fabrics," *Textile Research Journal,* vol. 79, pp. 675-686, May 1, 2009.

[12] "Peroxide explosive detection improves," *Jane's Airport Review,* 2005.

[13] A. Schreck, A. Knorr, K. D. Wehrstedt, P. A. Wandrey, T. Gmeinwieser and J. Steinbach, "Investigation of the explosive hazard of mixtures containing hydrogen

peroxide and different alcohols," *Journal of Hazardous Materials,* vol. 108, pp. 1-7, 2004.

[14] D. A. Burns and E. W. Ciurczak, *Handbook of near-infrared analysis*: CRC Press, 2008.

[15] R. Lindley, E. Normand, M. McCulloch, P. Black, I. Howieson, C. Lewis and B. Foulger, "Bulk and trace detection of ammonia and hydrogen peroxide using quantum cascade laser technology: A tool for identifying improvised explosive devices," in *Optics and Photonics for Counterterrorism and Crime Fighting IV, September 15, 2008 - September 16, 2008*, Cardiff, Wales, United kingdom, 2008, p. SPIE Europe.

[16] J. Canny, "A Computational Approach to Edge Detection," *IEEE Transactions on Pattern Analysis and Machine Intelligence,* vol. PAMI-8, pp. 679-698, 1986.

[17] J. S. Lim, *Two-dimensional signal and image processing*. Englewood Cliffs, NJ: Prentice-Hall, 1990, pp. 478-488.

[18] J. R. Parker, *Algorithms for Image Processing and Computer Vision*. New York: John Wiley & Sons, Inc., 1997, pp. 23-29.

Chapter 6

Summation, conclusions and further work

6.1 General summary and conclusions

6.1.1 The use of NIRS

In view of the emergent threat of terrorist activities, and the increasing importance of robust and effective scanning mechanisms to detect and categorize harmful and dangerous substances that might be used in improvised explosive device, several scanning technologies have been investigated and tested in scanning systems at vulnerable locations such as airports. It is, however, felt that these current scanning techniques have certain inherent limitations, which might be overcome with the use of NIR spectroscopy in such an application. In this context, this work presents an investigation into the interaction of NIR wavelengths with a range of clothing fabrics, and the use of NIRS to detect and image specific chemical compounds alone and hidden behind such fabrics.

The use of near infrared spectroscopy in various industrial applications has grown in popularity in recent decades, and it has been adopted as the technique of choice for multifarious process monitoring and quality control tasks. This has been due in part to the breadth of compositional and structural information available in the NIR overtone and combination spectra of pertinent test samples, the inexpensive and portable instrumentation available to perform NIRS, and the high data throughput rates achievable with this technique.

NIRS falls under the purview of vibrational spectroscopy, with the origin of spectra that appear in this region traceable to the anharmonic vibrations that take place in the molecular bonds of test samples: as NIR energy at specific characteristic wavelengths is absorbed in these bonds, it prompts overtone and combination transitions that excite vibrations at higher energy levels. The lack of specificity and redundancy encountered in the resultant absorbance spectra, however, necessitate a chemometrics-based approach to glean useful information about the qualitative and quantitative structure of the pertinent test samples.

6.1.2 Experiments on NIR transmission

In a preliminary set of investigations, the mechanism of interaction between NIR energy and materials such as sheets of paper, polystyrene foam and various types of clothing fabrics was studied. The results of through-transmission experiments with an 850 nm NIR laser diode across a range of material samples revealed that the magnitude and spatial distribution of through-transmitted energy was dependent on factors such as thickness of the material, porosity of fabric samples, spatial distribution of the pores, and surface texture of the samples. Particular attention was paid to investigating the effect of varying these parameters in fabric samples on the spatial distribution and intensity of resulting signal energy. It was concluded that, while the magnitude of through-transmitted signal was directly proportional to the overall porosity of the fabric sample, the layout of the radiation pattern as it emerged on the far side of the sample was determined by the distribution and size of individual pores. This was further investigated by using a special type of test samples, comprising different varieties of metallic TEM grids. These had a uniform thickness (~9 µm) and diameter (~3.05 mm), while the pore sizes varied from around 6 µm to 100 µm. The radiation pattern recorded with the largest pores did not show any evidence of scattering, while the one recorded with the smallest pore sizes had clear effects of scatter manifested in the form of diffraction patterns with side lobes etc.

Additional experiments were performed with wet fabric samples, and samples dyed in various colours. It was revealed that an increase in the moisture content of the sample resulted in increased through-transmitted signal levels, which was attributed to the reduced optical impedance of the sample due to the water content, as well as greater optical homogeneity of the surface texture with the water filling in the pores. The different coloured dyes, however, had minimal impact on the resulting signal levels. It was, therefore, concluded that fabric materials with larger pores and a more uniform, even and less chaotic surface texture would allow higher signal magnitudes to be transmitted, while the colour of the fabric would not impact NIR through-transmission in any significant manner.

Following on from the above investigations at a single NIR wavelength, instrumentation was designed to perform spectroscopic measurements utilizing the entire range of

wavelengths (850 nm – 2,200 nm) in the NIR region. The optical bench, which was comprised of commercial off-the-shelf components, was designed to record measurements at a standoff distance of 3 m to test the operability of such an arrangement in a practical security screening environment. Measurements were made in diffuse reflectance mode with solids, and in transflectance mode with liquids, using a diffuse PTFE reflector in the latter case.

The nature of the interaction between NIR energy and fabrics, followed by solid chemical powders comprising different ammonium salts, and aqueous solutions of ethanol, hydrogen peroxide and ammonium nitrate was investigated. The results with fabrics showed characteristic absorbance spectra with features specific to each fabric type. The amplitude of these features was found to be relatively low at wavelengths up to 1,400 nm, which facilitated the use of the range between 850 nm – 1,400 nm for locating the characteristic spectra of chemicals and, if found to be present, announce detection of the relevant samples hidden behind such fabrics.

It was observed that collecting absorbance spectra of chemicals, with reference to the intensity spectra of the intervening fabric layers, allowed improved discernment of spectral features characteristic of the chemicals. The spectra collected in this manner for different ammonium salts in powdered form had remarkably similar features owing to the presence of the ammonium ion in each case, while the spectra of aqueous solutions of different chemicals also contained features specific to the chemicals. An interesting feature that emerged in the spectra of solid chemicals as well as aqueous solutions collected in the presence of different fabric layers including polyester, cotton, acrylic and wool, was the similarity in the recorded spectral profiles with features characteristic of the relevant chemicals, irrespective of the type of fabric used. This was deemed to be a significant finding, as it allowed for the possibility of detecting chemicals based on a standardized set of features for each chemical, applicable to all types of concealing fabrics.

6.1.3 The need for chemometrics-based approach
The fabric layers were found to introduce certain distortive effects in the spectra, which mainly manifested in the form of a significant reduction in spectral amplitudes: the

amplitudes recorded in the presence of, and with reference to, fabric layers were around 20 times less than those recorded with the chemicals alone. Additionally, certain characteristic features observed in the spectra of the chemicals alone were either absent or largely diminished in the presence of fabric layers, especially at wavelengths where such features coincided with those of the fabrics. On account of such inconsistencies, a chemometrics-based approach to prediction modelling was deemed to be essential, in order to base the requisite calibration models on multivariate data rather than relying on a univariate approach.

Prediction modelling was thus undertaken to detect the presence of hidden chemicals through pattern recognition/ classification, using neural network-based calibration models. Specific data pre-processing routines and training algorithms were instituted to ensure optimal training of the neural networks, while preventing overfitting and ensuring adequate generalization capability to allow the model to extrapolate beyond the training domain. This extrapolation capability was specifically tested by presenting test data to the model that were largely comprised of the spectra of chemicals hidden behind such fabric layers as had not been included in the training data. With 68% of the test data comprised of such spectra, the trained model correctly classified 91% of the samples.

Following neural network-based detection, a second PLSR-based model was used to quantify the detected chemical in terms of its concentration in aqueous solution. Using test spectra collected at the same standoff distance in a PLSR model calibrated to quantify hydrogen peroxide, it was concluded that concentrations above 10% in the presence of a fabric layer could be predicted within a margin of error of ±5%. Further, an outlier detection algorithm based on prediction influence plots was used to enable segregation of hydrogen peroxide samples with concentration as low as 3% (in the absence of fabric layer) from other chemical samples that might have been wrongly classified as hydrogen peroxide in the initial step.

As the quantification and outlier detection measures were obtained within the same arrangement as that used in the initial detection step, these were deemed to provide a useful add-on module to the main detection step.

Chapter 6: Conclusions and recommendations for further work

A preliminary processing step was next introduced in the form of lock-in amplification of raw spectral data, with the aim to sufficiently enhance the SNR to enable recovery of spectral data buried in background noise in a practical screening environment. A through-transmission arrangement was used for this set of experiments, with a software-based lock-in amplifier designed to process multi-channel spectral data, using an optical source modulated with the reference frequency of the amplifier. The results demonstrated adequate suppression of noise when SNR was set as low as -60 dB, to enable subsequent chemical detection using neural network-based calibration models.

Additionally, two-dimensional spectroscopic imaging was performed by carrying out cross-sectional scans of test samples, and plotting the corresponding results of chemical detection in the form of intensity images colour-coded to depict the presence of specific chemicals at the scanned coordinates.

Based on all the experimental evidence gathered in the course of this work, it has been concluded that NIRS allows the functionality to detect specific chemicals from a standoff distance, when such chemicals are hidden from view underneath a layer of clothing. Furthermore, detection can be performed in the presence of relatively high levels of noise in the relevant wavelength channels, by performing lock-in amplification of the spectra to enhance the pertinent SNR.

6.2 Recommendations for further work

It is felt that, before the technique could be utilized in a security screening system, some further investigations as proposed below may be performed in order to cover additional ground regarding the practical implications involved in such an application.

Additional studies should be carried out to investigate the applicability of the technique in the detection of chemicals contained in commonly used bottles made of PET (polyethylene terephthalate) or coloured glass [1]. This would lead to the introduction of additional details in the spectra, such as the spectral features of PET [2], which would need to be factored in during subsequent processing/ detection process.

In a practical screening application, the active optical illumination irradiating the

chemical might be affected by the opacity of the container and other ambient factors such as passive optical signatures of devices introduced in the vicinity of the system. Such factors would introduce additional variables in the calculations, and could have a significant impact on the accuracy of calculations based on small variations in spectral amplitudes, such as the estimation of analyte concentration. While measures such as lock-in amplification serve to mitigate these adverse effects, the related issues need to be investigated and understood in greater detail, and if necessary, modelled and incorporated in the relevant processing algorithms.

Further variability in the results could be expected on account of the tested chemicals containing mixtures of compounds. This is an important consideration in practical screening, and needs further investigation. In order to calibrate the models to detect dangerous chemicals in mixtures [3], calibration methods such as stepwise multiple linear regression [4] might prove useful, and could be used in conjunction with the existing methods [5].

In the context of detection across layers of fabrics, a baseline/ standardized fabric model based on the prominent spectral features of a representative set of clothing fabrics could be established, and used as the reference level for recording all absorbance spectra in such an application.

With regards to the choice of a reflective surface when screening for liquid samples, a skin substitute could be used in place of PTFE to investigate and model the impact of such a surface on the resulting NIR spectra, allowing a closer approximation to personal screening applications.

Finally, in order to perform spectroscopic imaging in a practical screening system on the pattern introduced in Chapter 5, a much higher scan rate than that achieved during this work would be required. A possible solution would comprise a detection system incorporating an array of collecting lenses feeding fibre optic cables, with the outputs of the fibres connected to an optical time-division multiplexer, suitably designed to digitize and multiplex the optical signals [6-10]. The output of the multiplexer would be connected to the spectrometer, and the operation of the spectrometer controlled via an

external trigger based on the multiplexer clock. As the resulting scan rate would be limited only by the integration time of the spectrometer and the size of the collecting array, such a system would allow specific areas to be imaged in a matter of seconds, if not milliseconds. The system could then be adapted to image specific spatial cross-sections with the collecting lenses/ fibres installed around the periphery, for instance, of a walking channel for passengers in an airport.

Another possible practical implementation could be in the form of a portable hand-held scanner [11] incorporating a detector array of the type described above, and an NIR spectrometer with miniaturized form factor.

6.3 References

[1] H. Itozaki and Y. Yamauchi, "Liquid explosive detection from outside of the bottle by IR," in *Proceedings of SPIE - The International Society for Optical Engineering - Infrared Technology and Applications XXXV, April 13, 2009 - April 17, 2009*, Orlando, FL, United states, 2009.

[2] J. Rodgers and K. Beck, "NIR Characterization and Measurement of the Cotton Content of Dyed Blend Fabrics," *Textile Research Journal,* vol. 79, pp. 675-686, May 1, 2009.

[3] G. M. Stone, "Application and limitations of advanced technologies in explosives detection," in *Proceedings of the 1990 International Carnahan Conference on Security Technology: Crime Countermeasures, October 10, 1990 - October 12, 1990*, Lexington, KY, USA, 1990, pp. 81-87.

[4] H. Martens and T. Næs, *Multivariate calibration*. Chichester [England]; New York: Wiley, 1989.

[5] F. Estienne, L. Pasti, V. Centner, B. Walczak, F. Despagne, D. J. Rimbaud, O. E. de Noord and D. L. Massart, "A comparison of multivariate calibration techniques applied to experimental NIR data sets. II. Predictive ability under extrapolation conditions," *Chemometrics and Intelligent Laboratory Systems,* vol. 58, pp. 195-211, 2001.

[6] H.-G. Weber, R. Ludwig, S. Ferber, C. Schmidt-Langhorst, M. Kroh, V. Marembert, C. Boerner and C. Schubert, "Ultrahigh-speed OTDM-transmission technology," *Journal of Lightwave Technology,* vol. 24, pp. 4616-4627, 2006.

[7] S. Kawanishi, "Ultrahigh-speed optical time-division-multiplexed transmission technology based on optical signal processing," *IEEE Journal of Quantum Electronics,* vol. 34, pp. 2064-2079, 1998.

[8] A. A. Aboketaf, A. W. Elshaari and S. F. Preble, "Optical time division multiplexer on silicon chip," *Optics Express,* vol. 18, pp. 13529-13535, 2010.

[9] M. Saruwatari, "All-optical signal processing for terabit/second optical transmission," *IEEE Journal on Selected Topics in Quantum Electronics,* vol. 6, pp. 1363-1374, 2000.

[10] M. Pu, H. Ji, L. H. Frandsen, M. Galili, L. K. Oxenlwe and J. M. Hvam, "High-Q microring resonator with narrow free spectral range for pulse repetition rate multiplication," in *2009 Conference on Lasers and Electro-Optics and 2009 Conference on Quantum Electronics and Laser Science Conference, CLEO/QELS 2009, June 2, 2009 - June 4, 2009*, Baltimore, MD, United states, 2009.

[11] T. Hyvärinen, E. Herrala, J. Malinen and P. Niemelä, "NIR analyzers can be miniature, rugged and handheld," in *Near Infra-red Spectroscopy*, K. I. Hildrum, T. Isaksson, T. Næs, and A. Tandberg, Eds., Chichester, England, Ellis Horwood Limited, 1992, pp. 135-140.

Publications

Journal papers

A. Saleem, C. Canal, D. A. Hutchins, L. A. J. Davis and R. J. Green, "Techniques for quantifying chemicals concealed behind clothing using near infrared spectroscopy," *Anal. Methods, DOI:10.1039/C1AY05301A,* 2011.

C. M. Canal, A. Saleem, R. J. Green and D. A. Hutchins, "Remote identification of chemicals concealed behind clothing using near infrared spectroscopy," *Analytical Methods,* vol. 3, pp. 84-91, 2011.

Conference papers

A. Saleem, C. Canal, D. A. Hutchins and R. J. Green, "NIR spectroscopy with multivariate calibration and lock-in amplification to detect chemicals concealed behind fabrics," in *Chemical, Biological, Radiological, Nuclear, and Explosives (CBRNE) Sensing XII, part of SPIE Defense, Security, and Sensing*, Orlando, Florida, USA, 2011, pp. 8018 I 1-18.

D.A. Hutchins, C.M. Canal, A. Saleem, L.A.J. Davis and R.J. Green, " Remote identification of chemicals concealed behind clothing using near infrared imaging and spectroscopy," in *1ˢᵗ EU Conference on the Detection of Explosives (EUCDE)*, Avignon, la belle France, 2011.

C. M. Canal, A. Saleem, R. J. Green and D. A. Hutchins, "Near infrared spectroscopy for personal screening," in *SPIE Optics and Photonics for Counterterrorism and Crime Fighting VI and Optical Materials in Defence Systems Technology VII, September 20-23, 2010*, Toulouse, France, 2010.

```matlab
% File: nnip.m ****************************************************
% Created: 13/01/2011
% Last modified: 01/02/2011
% Created by: Aamer Saleem
% ******************************************************************
% Loads and processes 2D NIR spectra of water & no object (zero
% absorbance) for NN training.
% Spectra recorded with reference: Incident light intensity
% Pre-processing: Filtering, followed by SNV and PCA
% The spectra were recorded with distilled water
% ******************************************************************


clear;


NV=40;       % No. of WL channels taken for processing: 850-2200nm↙
(Taken with inter-channel spacing=5)
EF=8;        % Elimination Factor: No. of initial spectra to omit due to↙
noise
n_pca=5;     % Number of PCs to be taken

% Define target vectors as extremes of the tansig transfer function (-1↙
and +1)
% Function mapminmax applied on Eth2, Hyd2 and Amm2 to obtain these↙
vectors (ref end of this file)

% Define target vectors as extremes of the logsig transfer function (0↙
and 1)
BGD=[1 0 0 0]';    % Target vector for background
WAT=[0 1 0 0]';    % Target vector for water
ETH=[0 0 1 0]';    % Target vector for ethanol
HDP=[0 0 0 1]';    % Target vector for hydrogen peroxide
CBD=[BGD WAT ETH HDP]'; % Combined target vectors (used in nndisp)

K=2;     % Polynomial order for Savitzky-Golay FIR smoothing filter
F=5;     % Frame size for Savitzky-Golay FIR smoothing filter

% Read training data
p1=textread('background_train_REFsourceintensity.txt');
% Truncate empty (zero) rows at the end
pInit=flipud(p1);
[C,I]=max(pInit(:,2));       % Max of YMove: All rows preceding this↙
are zero
pInit=flipud(pInit(I:end,:));% Exclude zero rows, and re-straighten the↙
matrix
p1=pInit(EF+2:end,3:NV+2);   % Exclude: Wavelengths in 1st row,
% initial EF noisy spectra, and XMove and YMove values in columns
% 1 & 2; no NaN spectral values in trailing WL channels in this
% case due ch. spacing = 5 instead of 6
p2=textread('waterOnSlide_train_REFsourceintensity.txt');
```

```matlab
% Truncate empty (zero) rows at the end
pInit=flipud(p2);
[C,I]=max(pInit(:,2));        % Max of YMove: All rows preceding this↙
are zero
pInit=flipud(pInit(I:end,:));% Exclude zero rows, and re-straighten the↙
matrix
p2=pInit(EF+2:end,3:NV+2);    % Exclude: Wavelengths in 1st row,
% initial EF noisy spectra, and XMove and YMove values in columns
% 1 & 2; no NaN spectral values in trailing WL channels in this
% case due ch. spacing = 5 instead of 6
p3=textread('ethanol_train_REFsourceintensity.txt');
% Truncate empty (zero) rows at the end
pInit=flipud(p3);
[C,I]=max(pInit(:,2));        % Max of YMove: All rows preceding this↙
are zero
pInit=flipud(pInit(I:end,:));% Exclude zero rows, and re-straighten the↙
matrix
p3=pInit(EF+2:end,3:NV+2);    % Exclude: Wavelengths in 1st row,
% initial EF noisy spectra, and XMove and YMove values in columns
% 1 & 2; no NaN spectral values in trailing WL channels in this
% case due ch. spacing = 5 instead of 6
p4=textread('hydrogenperoxide_train_REFsourceintensity.txt');
% Truncate empty (zero) rows at the end
pInit=flipud(p4);
[C,I]=max(pInit(:,2));        % Max of YMove: All rows preceding this↙
are zero
pInit=flipud(pInit(I:end,:));% Exclude zero rows, and re-straighten the↙
matrix
p4=pInit(EF+2:end,3:NV+2);    % Exclude: Wavelengths in 1st row,
% initial EF noisy spectra, and XMove and YMove values in columns
% 1 & 2; no NaN spectral values in trailing WL channels in this
% case due ch. spacing = 5 instead of 6
p=vertcat(p1,p2,p3,p4);       % Combine the training spectra

WL=pInit(1,3:NV+2);           % Wavelength scale

% Pre-processing: Filtering, followed by SNV and PCA:

% Filtering
pF = sgolayfilt(p',K,F);      % Filter data using Savitzky-Golay FIR↙
smoothing filter k=2 & f=15; filter operates on columns of objects

% Standard Normal Variate (SNV) transformation
% Map each object's mean to 0 and standard deviation to 1
pTFsnv=preprocessing(pF','snv'); % TOMCAT function preprocessing.m↙
requires and returns objects in rows and variables in columns, so↙
transpose of pF taken
pTFsnv=pTFsnv';
```

```matlab
% PCA: Take PC scores as input variables for calibration
% Use Matlab function processpca
[pTFms,ps1] = mapstd(pTFsnv);% Mean-correction and stddev-normalization↵
of x-variables (rows)
                              % Settings ps1 to be used for mapping test↵
spectra in nnop.m
[pTF,ps2] = processpca(pTFms,0.02); % Gives error if X has more rows↵
(variables) than columns (observations).
                              % Exclude PCs that account for less than↵
2% variance in the data
n_pca=size(pTF,1);            % Number of PCs taken

%result=ccpca(pTFms','k',n_pca,'plots',0); % ccpca.m is modified form↵
of LIBRA function cpca.m, to allow for X matrix that is already mean-↵
centred; n_pca PCs taken
%pTF=result.T';               % PC scores
%pldg=result.P;               % PC loadings: To be used for↵
transformation of test spectra in nnop.m

% Prepare Target matrix for logsig extremes (0 and 1)
t2(:,1:size(p1,1))=repmat(BGD,1,size(p1,1));
t2(:,end+1:end+size(p2,1))=repmat(WAT,1,size(p2,1));
t2(:,end+1:end+size(p3,1))=repmat(ETH,1,size(p3,1));
t2(:,end+1:end+size(p4,1))=repmat(HDP,1,size(p4,1));


% File: nnop.m **************************************************
% Created: 13/01/2011
% Last modified: 13/01/2011
% Created by: Aamer Saleem
% ******************************************************************
% Loads and processes NIR spectra for water and no object (zero
% absorbance) for testing a trained NN
% Spectra recorded with reference: Incident intensity
% Pre-processing: Filtering, followed by SNV and PCA
% These data were NOT used for training the NN (except no object
% spectra). The spectra were recorded with distilled water
% ******************************************************************
% To be run AFTER nnip.m
% ******************************************************************

% Read test data
pTestTotal=textread('watandeth_trv2_testing_REFincidentlight.txt');

% Truncate empty (zero) rows at the end
pTestInit=flipud(pTestTotal);
[C,I]=max(pTestInit(:,2));   % Max of YMove: All rows preceding this↵
are zero
pTestInit=flipud(pTestInit(I:end,:)); % Exclude zero rows, and re-↵
```

```matlab
straighten the matrix

pTest=pTestInit(2:end,3:NV+2); % Exclude: Wavelengths in 1st row,
% XMove and YMove values in columns 1 & 2, and NaN spectral values
% in the trailing WL channels
XMove=pTestInit(2:end,1);    % x-axis move coordinates of scan stage
YMove=pTestInit(2:end,2);    % y-axis move coordinates of scan stage

XMove=vertcat(XMove,-1);
YMove=vertcat(YMove,-1);

% Pre-processing: Filtering, followed by SNV and PCA:

% Filtering
pTestF = sgolayfilt(pTest',K,F); % Filter data using Savitzky-Golay FIR↙
smoothing filter k=2 & f=15; filter operates on columns of objects

% Standard Normal Variate (SNV) transformation
% Map each object's mean to 0 and standard deviation to 1
pTestTFsnv=preprocessing(pTestF','snv'); % TOMCAT function↙
preprocessing.m requires and returns objects in rows and variables in↙
columns, so transpose of pTestF taken
pTestTFsnv=pTestTFsnv';

% Mean-correction and stddev-normalization of x-variables (rows) using↙
calibration data settings ps1
pTestTFms = mapstd('apply',pTestTFsnv,ps1);
% PCA of x-variables (rows) using calibration data settings ps2
pTestTF = processpca('apply',pTestTFms,ps2);

% Take averages of multiple spectra recorded at single XMove and YMove↙
coordinates
pTestTF=pTestTF';
%n_pca=size(pTestTFsnv,2);   % Set n_pca equal to the number of x-↙
variables

XMS=size(pTestTF,1); % XMS: Total number of spectral objects recorded
nsim=1;
cc=0;
Xsum=zeros(1,n_pca);
pTestTFc=zeros(XMS,n_pca);
XMovec=zeros(XMS,1);
YMovec=zeros(XMS,1);
chk=zeros(1,10); chkc=0;

for j=1:XMS
    if(XMove(j)==XMove(j+1) && YMove(j)==YMove(j+1))
        nsim=nsim+1;
    else
```

```matlab
        for k=0:nsim-1
            Xsum=Xsum+pTestTF(j-k,:);
        end

        cc=cc+1;
        pTestTFc(cc,:)=Xsum/nsim; % Average spectrum at the same x and↵
y coordinates
        XMovec(cc)=XMove(j);
        YMovec(cc)=YMove(j);

        if(nsim>=3 || nsim==1) chkc=chkc+1; chk(chkc)=j; end
        Xsum=zeros(1,n_pca);
        nsim=1;
    end
end

% Compress resulting data to truncate trailing zeros
pTestTFc=pTestTFc(1:cc,:)';
XMovec=XMovec(1:cc);
YMovec=YMovec(1:cc);


% File: nnpr.m **************************************************
% Created: 13/01/2011
% Last modified: 13/01/2011
% Created by: Aamer Saleem
% ******************************************************************
% Defines and trains a new Neural Network with Bayesian
% regularization training function 'trainbr', using training dataset
% prepared in nnip.m.
% Simulates the trained network with training data and test data
% ******************************************************************
% To be run AFTER nnip.m and nnop.m
% ******************************************************************

S=3;        % Size of the hidden layer

% NN defined/ trained for targets spanning the values [0 1]
net2=newpr(pTF,t2,S); % newpr returns a network exactly as newff
% does, but with an output layer transfer function of 'tansig' and
% additional plotting functions included in the network's
% net.plotFcn property.
net2.divideFcn ='';
net2.trainFcn='trainbr';
net2.trainParam.show = 10;
net2.trainParam.epochs = 500;
net2 = init(net2);
[net2,tr2]=train(net2,pTF,t2); % Confusion matrix for this NN↵
calculated with original output matrix as output vectors span [0 1]
```

```matlab
% Simulate the net2 NN (0-1 outputs) using training data pTF and test
data pTestTFc
y2=sim(net2,pTF);
[c2,cm2,ind2,per2] = confusion(t2,y2);

yTest2=sim(net2,pTestTFc);
[cT2,cmT2,indT2,perT2] = confusion(tTest2,yTest2);

% Above-obtained simulation data plotted in nndisp.m


% File: nndisp.m *************************************************
% Created: 13/01/2011
% Last modified: 13/01/2011
% Created by: Aamer Saleem
% *****************************************************************
% Displays the confusion outputs of NN trained/ simulated in nnpr.m
% *****************************************************************
% To be run AFTER nnpr.m
% *****************************************************************

% Display the data about how test samples have been classified
% Write text file to allow plotting of results in Surfer, and plot data
in 3-D
yTest2tr=yTest2';

% Detection Thru. Max: The index of the highest output value in each
result vector is taken to signify the corresponding element
[yTestdecCm,yTestdecC]=max(yTest2); % In yTestdecC (max indices
vector), Background=1; Water=2; Ethanol=3; Hydrogen Peroxide=4
yTestdecC=yTestdecC';

ResXYSd=[XMovec YMovec yTestdecC];
dlmwrite('ResXYSd_MatPCA_op.txt',
ResXYSd,'delimiter','\t','newline','pc');

% Re-order results matrix to plot contours/ surface in matlab
[C,I]=max(XMovec);
Ystep=YMovec(I+1)-YMovec(I);
Xstep=XMovec(2)-XMovec(1);
Xscale=0:Xstep:C;
Yscale=0:Ystep:max(YMovec);

yTestRS=zeros(length(Yscale),length(Xscale)); % Reshaped results matrix
initialized

for i=1:length(yTestdecC)
    xcoord=(XMovec(i)+Xstep)/Xstep;
```

```matlab
    ycoord=(YMovec(i)+Ystep)/Ystep;

    yTestRS(ycoord,xcoord)=yTestdecC(i);
end

figure,contour(Xscale,Yscale,yTestRS)                 % Good
figure,contourf(Xscale,Yscale,yTestRS)                % Best
figure,surf(Xscale,Yscale,yTestRS)                    % Good
figure,plot3(ResXYSd(:,1),ResXYSd(:,2),ResXYSd(:,3))  % Not good
```